Project No. 11-3126

Graphite Microstructural Characterization Using Time-Domain and Correlation-Based Ultrasonics

Reactor Concepts Research Development and Demonstration (RDRD&D)

James Spicer
John Hopkins University

William Corwin, Federal POC
Mary Snead, Technical POC

NEUP Nuclear Energy University Programs
U.S. Department of Energy

GRAPHITE MICROSTRUCTURAL CHARACTERIZATION USING TIME-DOMAIN AND CORRELATION-BASED ULTRASONICS

Principal Investigator:
James B. Spicer, spicer@jhu.edu

Co-Investigator:
Dennis C. Nagle (2012-13)

Students:
Lindsey R. Lindamood (Ph.D. 2014)
Lauren R. Olasov (M.S. 2015)
Fan W. Zeng (M.S. 2015)

Organization:
Department of Materials Science and Engineering
The Johns Hopkins University
3400 North Charles Street
Baltimore, MD 21218

Collaborators:
Cristian I. Contescu (2013-2017)
Nidia C. Gallego (2013-2017)
Glenn R. Romanoski (2012-13)

Organization:
Materials Science and Technology Division
Oak Ridge National Laboratory
Oak Ridge, TN 37831

Project Duration:
October 2011-September 2017

Technical Point of Contact for Reporting:
Mary Snead, Oak Ridge National Laboratory

Workscope: NGNP-2

PICSNE Workpackage Number: 3126

This report has been submitted in partial fulfillment of the reporting requirements for the Department of Energy NEUP. The information contained in this report represents the opinions of the investigational team and has been generated using the quality assurance requirements of the NEUP.

TABLE OF CONTENTS

ABSTRACT ……. 3

INTRODUCTION ……. 4

TECHNICAL RESULTS

1. EFFECTIVE MEDIUM, MULTIMODE ULTRASONICS FOR ASSESSMENT OF MICROCRACK DENSITY AND POROSITY

Section A: Laser Ultrasonic Assessment of the Effects of Porosity and Microcracking on the Elastic Moduli of Nuclear Graphites ……..……... 6

Section B: Modeling the Effects of Oxidation-induced Porosity on the Elastic Moduli of Nuclear Graphites …… 34

2. SHEAR BIREFRINGENCE MEASUREMENTS FOR DETERMINATION OF MICROCRACK DENSITY AND ORIENTATION DISTRIBUTION

Section C: Line Source Representations for Shear Wave Birefringence Measurements in Transversely Isotropic Materials using Laser Ultrasonics …….. 55

Section D: Subsurface, Thermoelastic Line Source Excitation of a Transversely Isotropic Half-Space ……... 73

Section E: Theory and Application of Laser Ultrasonic Shear Wave Birefringence Measurements to the Determination of Microstructure Orientation in Transversely Isotropic, Polycrystalline Graphite Materials ……..... 97

3. ULTRASONIC SCATTERING CORRELATION MEASUREMENTS FOR DEFECT DISTRIBUTION DETERMINATION

Section F: Laser Ultrasonic Correlation Measurements……..……. 122

CONCLUSIONS …… 126

ACKNOWLEDGEMENTS ……. 126

ABSTRACT

Among techniques that have been used to determine elastic modulus in nuclear graphites, ultrasonic methods have enjoyed wide use and standards using contacting piezoelectric tranducers have been developed to ensure repeatability of these types of measurements. However, the use of couplants and the pressures used to effectively couple transducers to samples can bias measurements and produce results that are not wholly related to the properties of the graphite itself. In this work, we have investigated the use of laser ultrasonic methods for making elastic modulus measurements in nuclear graphites. These methods use laser-based transmitters and receivers to gather data and do not require use of ultrasonic couplants or mechanical contact with the sample. As a result, information directly related to the elastic responses of graphite can be gathered even if the graphite is porous, brittle and compliant. In particular, we have demonstrated the use of laser ultrasonics for the determination of both Young's modulus and shear modulus in a range of nuclear graphites including those that are being considered for use in future nuclear reactors. These results have been analyzed to assess the contributions of porosity and microcracking to the elastic responses of these graphites. Laser-based methods have also been used to assess the moduli of NBG-18 and IG-110 where samples of each grade were oxidized to produce specific changes in porosity. These data were used to develop new models for the elastic responses of nuclear graphites and these models have been used to infer specific changes in graphite microstructure that occur during oxidation that affect elastic modulus. Specifically, we show how ultrasonic measurements in oxidized graphites are consistent with nano/microscale oxidation processes where basal plane edges react more readily than basal plane surfaces. We have also shown the use of laser-based methods to perform shear-wave birefringence measurements and have shown how these measurements can be used to assess elastic anisotropy in nuclear graphites. Using models developed in this program, ultrasonic data were interpreted to extract orientation distribution coefficients that could be used to represent anisotropy in these materials. This demonstration showed the use of ultrasonic methods to quantify anisotropy and how these methods provide more detailed information than do measurements of thermal expansion – a technique commonly used for assessing anisotropy in nuclear graphites. Finally, we have employed laser-based, ultrasonic-correlation techniques in attempts to quantify aspects of graphite microstructure such as pore size and distribution. Results of these measurements indicate that additional work must be performed to make this ultrasonic approach viable for quantitative microstructural characterization.

INTRODUCTION

According to the *Nuclear Energy Research and Development Roadmap, Report to Congress* under the section "R&D Topics for Life Extension and Performance Improvement," data and methods are needed to assess the integrity of structures and components for safe and sustained nuclear plant operation. This report detailed how long-term materials degradation must be understood and used to predict material behavior. In particular, a milestone for materials research and development in this report was the baseline characterization of nuclear-grade graphites [1]. The ability to nondestructively assess the microstructural state of nuclear graphites is critical to qualifying these materials for current use as well as for future nuclear reactors. This type of assessment is needed:

1. to qualify graphite in its as-produced state before value-added processing occurs to make components
2. to assess graphite components before they are assembled into systems for operational use
3. to evaluate in-service components to assure reactor integrity.

Under the program covered by this report, ultrasonic nondestructive methods were used for characterization of nuclear grade graphites with the specific aim of correlating characteristic microstructural changes with ultrasonic properties. The importance of this investigation was that it would allow direct identification of different types of microstructural defects within the bulk of graphite bodies and allow for monitoring of defect density changes brought about by operations-induced damage. The ultimate aim of this investigation was to identify ultrasonic characterization methods that could be used to perform structural health monitoring of nuclear graphites in service-specific conditions.

Polycrystalline nuclear-grade graphites have complicated microstructures that relate directly to the types of precursor materials and the production methods used to form graphite. For example, in various grades of nuclear graphite (such as NBG-18 and IG-110) isotropic cokes are used as filler materials since they can be used to produce isotropic or nearly isotropic graphites [2]. These types of graphites are preferred since the behaviors can be more readily predicted. However, even if the graphite is initially isotropic, damage accumulation can cause the material to become anistropic – this damage can be sensed using ultrasonic techniques. Propagation of ultrasound in polycrystalline materials can be described using stiffness tensors along with orientation distribution functions (related to grain orientations within the graphite body). Defect structures present in as-produced materials including spherical and lenticular voids/porosity and microcracks [3]. Exposure to operational conditions can induce macroscopic creep and crack closure or crack formation/growth owing to swelling of graphite domains. This swelling, perpendicular to graphite planes in individual grains, results from neutron-induced, in-plane voids producing self-interstitials between graphite planes. This swelling can initially result in the closing of nearby, aligned microcracks and, as a result, can produce higher mechanical strengths and toughnesses.

Further irradiation can result in swelling-induced crack and void growth owing to microstructural incompatibilities with a resulting loss of material integrity. The elastic moduli of nuclear graphites are typically measured using sonic/ultrasonic/vibrational resonance techniques. While these latter techniques can be used for nondestructive evaluation purposes, ASTM standards for manufactured carbons and graphites (ASTM D02.F) are currently in development [3].

In published reports, laser ultrasonics has proven to be an effective means to characterize nuclear grade graphites and the program of research reported here builds on these previous results. In early work by O'Brien, Telschow and Knibloe, laser-ultrasonic surface acoustic waves were used to measure elastic anisotropy in samples from a GraphNOL N3M billet [4]. Additional measurements with contacting, polarized shear-wave transducers (2.25 MHz) showed birefringence effects related to the billet pressing direction. Contacting measurements by Harvel and Chang using longitudinal wave transducers showed that ultrasonic frequencies between 0.5 and 1 MHz were optimal for making measurements in arc furnace, graphite rod electrodes [5]. Unlike these earlier works, the research described here attempts to quantitatively correlate various ultrasonics characteristics with graphite microstructure.

This report follows the general structure of the overall research program – three different laser-based ultrasonics methods were developed to perform, microstructural characterization of nuclear grade graphites and these can be described as follows:

1. Effective Medium, Multimode Ultrasonics for Assessment of Microcrack Density and Porosity,
2. Shear birefringence measurements for determination of microcrack density and orientation distribution,
3. Ultrasonic scattering correlation measurements for defect distribution determination.

Both experiment and modeling in each of these areas will be detailed in the following sections of this report.

References

[1] *Nuclear Energy Research and Development Roadmap: Report to Congress*, U.S. Department of Energy – Nuclear Energy, April 2010.

[2] T. Burchell, R. Bratton and W. Windes, *NGNP Graphite Selection and Acquisition Strategy: Gen IV Nuclear Energy Systems* – ORNL/TM-2007/153, Oak Ridge National Laboratory, U.S. Department of Energy, September 2007.

[3] T. Burchell, "Nuclear Graphite," presentation to the U.S. Nuclear Regulatory Commission, January 12. 2011.

[4] M.H. O'Brien, K.L. Telschow and J.R. Knibloe, "Analysis of As-Machined Nuclear Graphite Parts Using Conventional and Laser Ultrasonic Techniques," *Journal of Nuclear Science and Technology* 29(4), 378-387 (1992).

[5] G.D. Harvel and J.S. Chang, "Nondestructive Evaluation of Multiply Connected Electrical Arc Furnace Graphite Rod Electrodes," *Research in Nondestructive Testing* 20, 215-229 (2009).

1. Effective Medium, Multimode Ultrasonics for Assessment of Microcrack Density and Porosity

Section A: Laser Ultrasonic Assessment of the Effects of Porosity and Microcracking on the Elastic Moduli of Nuclear Graphites

A.1. Introduction

Bulk nuclear graphites are multifunctional materials that play critical roles in various reactor designs. They can serve as neutron moderators, reflectors and structural components in reactor cores. As a class of materials, nuclear graphites display a range of complicated microstructures even though they have high chemical purity [A1]. These microstructures relate directly to the precursors used to synthesize graphite as well as the processing steps used to form these materials into billets for the manufacture of reactor components [A2]. While the properties of single crystal graphite are well known [A3], the properties of bulk graphites depend heavily, if not predominantly, on microstructure [A4]. Microstructural elements include crystalline graphite, amorphous carbon, porosity, microcracking as well as others and each influences various behaviors depending on its presence in the overall microstructure [A2,A5]. The extent to which these microstructural elements appear in any given type of graphite depends on the methods used for production. In the nuclear environment, these components of the microstructure affect overall performance, influence the rates at which damage accumulates and, ultimately, govern the degradation of material performance [A2,A6-8]. In particular, graphite strength and stiffness are among the properties that are important for material performance in nuclear applications.

When used in the reactor core, graphite is exposed to high temperatures and neutron irradiation as well as oxidative species with the precise conditions being dictated by the type of reactor under consideration. Operational temperatures can cause changes in stiffness and strength and creep can occur when graphite is subjected to fast neutron irradiation under mechanical loading [A9-11]. Graphite oxidation has the effect of increasing material porosity and this can impact material stiffness and strength [A6,A12,A13]. Also, neutron irradiation initially increases stiffness and strength, but beyond some dose, both decrease [A14]. All of these effects have been studied in various graphites and models have been developed to predict how these properties will vary during reactor operation with the goal of identifying service lifetimes [A15]. However, even if models are used to predict the material behavior, there is a need to perform inspection of critical components to verify material integrity and to update models with information regarding the state of the material. Since material stiffness appears to correlate with strength in these materials, some type of measurement of the elastic moduli could prove valuable in assessing the state of the material and could be used to infer changes of the microstructure.

In this work, the moduli in a selection of nuclear graphites have been measured using laser ultrasonic methods. Ultrasonic measurements of longitudinal and shear waves have been made in different propagation directions in each of these graphites and were converted to corresponding moduli

using determinations of sample density and wavespeed. With these moduli, Young's modulus could be determined as well. Trends between modulus and porosity volume fraction were identified and, in combination with models describing the stiffness of porous materials, were used to assess the influence of microcracking on the modulus in these materials. Models for the relationship between microcracking and modulus have been used to estimate the crack populations necessary to account for the behavior of the graphites in this study.

A.2. Background on Nuclear Graphite Modulus and Related Models

A.2.1. Nuclear Graphites

As a structural material, graphite exhibits interesting behaviors under conditions that exist in reactor cores. As has been noted, neutron irradiation can initially produce significant increases in graphite stiffness and strength [A14] – these can be advantageous for the structural performance. The microstructural mechanism responsible for these changes is related to primary knock-on atoms (PKAs) inserted between (0001) planes in the graphite structure. Nucleation and growth of interplanar PKA regions produces swelling or expansion along the c-axis (or [0001] direction) of graphite crystallites. This swelling interacts with other microstructural features such as adjacent pores and microcracks (including Mrozowski cracks) and can affect the bulk mechanical properties by altering these features [A16]. In particular, induced compressive stresses that close microcracks can lead to increased stiffness and strength. Continued neutron exposure ultimately reduces strength when swelling can no longer be accommodated by the graphite microstructure – induced internal stresses reach levels that facilitate material failure. Since reductions in modulus accompany this loss of strength, measurements of modulus could provide valuable insight into the structural integrity of graphite.

In this study, the moduli of 13 different nuclear graphites have been measured to provide baseline information on the as-produced state of these materials. Some of these are currently produced by graphite manufacturers for possible use in reactors while others are legacy graphites that were either used in previous reactor designs or were developed for adoption in the past. Nuclear graphites display a range of crystallinity, porosity, grain sizes, pore size distributions, grain size distributions and grain orientation distributions that relate to the precursor materials and processes used during graphite production. Details regarding production methods and microstructures for some of the graphites used in this study are provided by Burchell *et al.* [A17] and by Karthik *et al.* [A18]. Generally, graphites are synthesized from petroleum- or pitch-based cokes through a sequence of processing steps that include calcination, grinding and blending, mixing with binders, forming, baking and impregnation, and graphitization [A2]. Additional processing to purify the graphite can be performed – this is important for nuclear graphites to ensure predictable behavior in the reactor environment. Even though these processing steps are

nominally the same for most graphites, differences in the starting coke, the grinding operations, the forming processes as well as the impregnations can yield materials with widely varying microstructures that exhibit different densities, grain sizes and anisotropy. Figure A.1 shows scanning electron micrographs of three different graphites studied in this work – IG-110, NBG-18 and HLM. These images illustrate microstructural differences among these materials that might influence various properties including their elastic responses. While these micrographs primarily illustrate micrometer scale porosity, other important microstructural differences exist that could be identified by examining these graphites using higher resolution microscopy. Despite these differences, nuclear graphites are highly crystalline. This unifying characteristic not only has important implications for the overall mechanical properties of these materials but also permits a generalized investigation of structure-property relationships.

A.2.2. Models for Effects of Microstructure on Modulus

A.2.2.1. Moduli of Porous Media

Porosity plays a significant role in determining the stiffness of nuclear graphites, and its presence can be quantified using a range of techniques. For example, open porosity can be measured using mercury porosimetry while closed porosity can be inferred from measurements of open porosity and evaluation of total porosity (using X-ray or small angle neutron scattering or determinations of sample mass and volume). The elastic responses of materials, including those associated with ultrasonic measurement, are generally assumed to depend on total porosity and there are many models in the literature that have been used to interpret the variation of elastic modulus with porosity. In early work on a type of isotropic graphite (POCO graphite), Cost *et al.* measured Young's modulus and the shear modulus as a function of porosity over the approximate range 0.13 to 0.32 for the porosity volume fraction [A19]. They considered using a linear fit for their results but instead used an exponential fit to model trends. This approach was chosen owing to the experimental findings at that time, but was not justified on a theoretical basis. Later work by Shibata *et al.* examined the variation in the longitudinal wave velocity in two different isotropic graphites (IG-110 and IG-430) as a function of porosity [A13] and found that their results could be interpreted using models put forth by Takatsubo and Yamamoto [A20]. These models predict a nearly linear variation of Young's modulus with porosity volume fraction (for low porosities) and include dependence on pore shape. The work presented here will use models proposed by Hashin and Shtrikman for the bounds on the moduli of two phase materials [A21,A22]. If the primary phase is assumed to be graphite and the secondary phase is composed of porosity, then expressions for the upper bound on Young's modulus, E', and shear modulus, G', as a function of porosity, φ, can be written using their results as follows:

$$E'/E = e(\lambda,G,\varphi)\frac{1+\lambda/G}{1/3+(2/3+\lambda/G)e(\lambda,G,\varphi)/g(\lambda,G,\varphi)} \tag{A.1}$$

and

$$G'/G = g(\lambda,G,\varphi) \tag{A.2}$$

where E and G are the Young's modulus and shear modulus, respectively, for the porosity-free case,

$$e(\lambda,G,\varphi) = 1 - 3\varphi(\lambda+2G)[4G+\varphi(3\lambda+2G)]^{-1} \tag{A.3}$$

and

$$g(\lambda,G,\varphi) = 1 - 15\varphi(\lambda+2G)[9\lambda+14G+2\varphi(3\lambda+8G)]^{-1} \tag{A.4}$$

with $\lambda = G(E-2G)/(3G-E)$ being a Lamé constant related to the porosity-free moduli. The exact expression for E'/E in Eq. (A.1) can be approximated by $E'/E \approx e(\lambda,G,\varphi)$ and differs from the exact result only by a few percent for conditions to be considered in this work. Using estimates for the stiffness of porosity-free, nuclear graphites, the expressions given in Eqs. (A.1) and (A.2) can be evaluated as a function of porosity yielding the results presented in Fig. A.2. For the porosities considered, Young's modulus and the shear modulus vary in nearly the same manner (the two plots overlap over most of the range) and appear to have a dependence on porosity that is almost linear.

2.2.2. Moduli of Microcracked Media

Microcracking likely contributes, perhaps equally, to the overall moduli of graphite [A18]. In this work, microcracking refers to all crack-like structures with characteristic dimensions much smaller than the ultrasonic wavelengths being used for measurements. Bulk measurements in graphite typically employ ultrasonic frequencies below 10 MHz and these would yield ultrasonic wavelengths greater than approximately 160 μm (based on a shear modulus of 4.5 GPa and a density of 1.81 g/cm^3). Material structures, such as cracks, tend to scatter ultrasound when their dimensions exceed the ultrasonic wavelength. However, structures much smaller than the ultrasonic wavelength do not scatter strongly but their presence does affect various material properties (in an effective medium approximation). For the purposes of this work, it is assumed that all micro- and sub-micrometer cracks primarily affect ultrasonic propagation by modifying the elastic moduli being measured. Among these are Mrozowski cracks that readily form in graphites during processing as a result of differential thermal stresses and occur between parallel graphite layers in crystallites as well as along basal planes at filler/matrix interfaces. These cracks can be seen in high magnification micrographs [A23], but quantification of the characteristics of these structures is relatively difficult compared to determination of total porosity. Even though cracks could be considered to be extremely high aspect ratio pores (a limiting form), they do not contribute to determinations of total porosity using measurements of sample mass and volume, and their effect on

modulus must be taken into account separately. There are a variety of models in the literature describing the influence of microcracks (also called strong discontinuities) on modulus [A24-37]. Even though the literature describing acoustic interactions with microcracks and related discontinuities is considerable, no experimental studies have been performed to assess the validity of these models. In the absence of a preferred approach to modeling the moduli of microcracked materials, the development presented by Zheng will be used [A38].

This model can be related to the energy states of materials containing cracks – especially microcracks that have dimensions much less than the acoustic/ultrasonic wavelengths of interest since these are weak scatterers and do not re-direct the propagating elastic wave. Microcracks affect stress state energies in the material and can be described using established fracture mechanics approaches based on the *J*-integral. Since microcracks contribute to the total elastic energy state of the material, they affect the effective material stiffness. This type of effective medium approach can be used to quantify the expected variation of elastic stiffness with crack density. According to Zheng [A38], the strain energy per unit crack surface area as expressed by the *J*-integral, J, can be written as follows:

$$J = (K_I^2(1-\nu_0) + K_{II}^2(1-\nu_0) + K_{III}^2)(1+\nu_0)/E_0 \tag{A.5}$$

where E_0 is the Young's modulus and ν_0 is the Poisson ratio of the uncracked material while K_I, K_{II}, K_{III} are the stress intensity factors corresponding to crack opening under mode I, II and III loading by ultrasonic waves. For oriented, non-interacting, long-narrow-rectangular cracks, wave propagation perpendicular to the crack surfaces yields the following results for the microcrack-modified Young's modulus (E_3) and shear moduli (G_2, G_1) [A38]:

$$E_3/E_0 = (1-2\nu_0+2\nu_0^2\chi)[(1-2\nu_0+2(1-\nu_0)^2\chi)(1-2\nu_0^2\chi)]^{-1} \tag{A.6}$$

$$G_2/G_0 = [(1-\nu_0)\chi+1]^{-1} \quad \text{and} \quad G_1/G_0 = [\chi+1]^{-1} \tag{A.7}$$

where E_3 is Young's modulus for material displacement perpendicular to the crack surface, G_2 is the shear modulus for displacement perpendicular to crack length (long side), G_1 is the shear modulus for displacement along the crack length and G_0 is the modulus of the uncracked material. The critical parameter in these formulae is χ which Zheng refers to as the effective crack density (crack surface area per unit volume multiplied by the crack width). However, it is more correctly identified as the ratio of the internal energy density associated with cracks to the elastic energy density of the intact material – a crack energy density coefficient – and can be written as follows:

$$\chi = \pi n_c w^2 l \tag{A.8}$$

where n_c is the number of cracks per unit volume, w is the width (short side) of the crack face and l is its length (long side). In all of these expressions, the effective stiffness of the material decreases as crack density increases. This is shown in Fig. A.3 where the elastic moduli E_3 / E_0 and G_1 / G_0 (as expressed in Eqs. (A.6) and (A.7)) are shown as a function of the crack energy density coefficient. Since the crack geometry assumed here does not accurately reflect the microcracking that is likely present in the graphites in this work, other crack geometries should be examined and used to model more complicated crack distributions, but these types of studies are beyond the scope of this work. Even so, the model here is instructive and should provide an indication of the general influence of microcracking on stiffness in nuclear graphites.

A.2.2.3. Moduli of Porous Media Containing Microcracks

These models should provide insight into the roles that porosity and microcracks play in determining the overall stiffness of graphite. However, it should be noted that the complicated microstructural elements in graphites interact in ways that are not fully captured by these simple models. Even so, for the purposes of this work, graphite will be considered to be composed of a secondary phase (pores) imbedded in a primary phase (graphite) containing microcracks, and each of these phases will be modeled using the ideas developed in the previous sections. With this description in place, the porosity-free values for modulus from Eqs. (A.1) and (A.2) (E and G) assume the roles of the moduli for the microcracked material in Eqs. (A.6) and (A.7) (E_3 and G_2 and/or G_1). In other words, if Young's modulus is considered and Eqs. (A.1) and (A.6) are expressed as $E' = f(\varphi)E$ and $E_3 = h(\chi)E_0$, then $E' = f(\varphi)h(\chi)E_0$ – this assumes that the effects of porosity and microcracking are separable. This approach implies that the modulus of a porous material with microcracking can be estimated if porosity, effective crack density and the modulus of the intact material are known. Alternatively, this overall description can be used to estimate the effective crack density – a quantity that is difficult to measure or determine otherwise. Again, consider Young's modulus. Equation (A.6) can be re-written to show effective crack density as a function of the normalized modulus for the microcracked material – $\chi = H(E_3 / E_0)$ (where the function H is the inverse of h so that $\chi = H(h(\chi))$). Using the previous definition for $f(\varphi)$ yields $\chi = H(E' / (f(\varphi)E_0))$. This means that effective crack densities can be estimated once porosity and modulus are known and permits an interesting comparison between crack and pore number densities.

The pore number density, n_p, can be expressed as $n_p = 3\varphi / (4\pi R^3)$ where R is the radius corresponding to an average pore volume, $v_p = 4\pi R^3 / 3$. Also, the effective crack density can be used to

obtain the crack number density using previous definitions: $n_c = \chi / (\pi w^2 l)$. The number of microcracks per pore is simply the ratio of these number densities:

$$\frac{n_c}{n_p} = (\frac{\chi}{\varphi})\frac{4R^3}{3w^2 l}. \tag{A.9}$$

The ultimate value in this overall approach for the current work is that it links ultrasonic measurements of modulus to important microstructural features of graphite and shows how alterations related to porosity or microcracking brought about by the service environment of the graphite might influence modulus.

A.2.3. Experimental Determination of Graphite Moduli

A.2.3.1. Graphite Ultrasonic Samples

Ultrasonic test samples were prepared from graphite blocks (or billet sections) obtained from Oak Ridge National Laboratory as well as from various manufacturers. Sample dimensions were approximately 50 mm x 50 mm x 6 mm (length x width x thickness) with ultrasonic propagation occurring through the thickness of each sample. At least two samples of each graphite type were tested and these were taken from different locations in the graphite blocks that were received. The orientation of each sample was perpendicular to others for a particular graphite grade. Additional samples for various grades were included to gather information on the variability of properties when the graphites were from different production runs or to assess effects of anisotropy in more detail. Even so, this overall approach to sample selection (in which a single sample of a given orientation was used to represent the behavior of the overall material in that direction) likely affects the generality of the results presented in this work. In some cases, the thickness directions could be related back to important directions characteristic of forming operations that occurred during graphite manufacture (such as an extrusion direction), but in other cases the relationship between sample and billet orientation could not be determined. Similarly, the general location of some billet sections in the original billets were known, but in most cases they were not. Since graphite properties vary with position in billets, this uncertainty and restricted sampling necessarily affect the generality and interpretation of results in this work. To minimize variability related to sample surface preparation, surfaces subjected to pulsed laser irradiation were finished using silicon carbide grinding paper while those used for ultrasonic detection were polished using 1 μm diamond paste. All samples were ultrasonically cleaned in a deionized water bath and were allowed to dry before ultrasonic measurements were made.

A.2.3.2. Ultrasonic Measurements

There are a variety of ultrasonic methods that can be used to determine modulus and each has characteristics that recommend its use. Depending on the methods used as well as the conditions under which measurements are made, modulus values can vary and, consequently, comparison of results must

be made with attention to the measurement protocol. For this study, a standard transmit-and-receive, through-thickness measurement geometry was used in which an ultrasonic transmitter was located directly opposite the receiver on the graphite sample surface. In this configuration, transit times for ultrasonic waves can be measured and can be used to compute the modulus of the material using the following relationship:

$$c_k = \rho(T / \Delta t_k)^2 = \rho v_k^2 \tag{A.10}$$

where c_k is the modulus being measured ($k = L$ for longitudinal waves and $k = S$ for shear waves), ρ is the sample density, T is the sample thickness, Δt_k is the transit time for the ultrasound through the sample and v_k is the wavespeed. If the variation of modulus with porosity is needed, then measurements of density and wavespeed can be used to compute modulus while the bulk porosity can be obtained from density using values for theoretical density. The relationship between density and porosity, φ, is given by the following:

$$\varphi = (1 - \rho / \rho_0) \tag{A.11}$$

where ρ_0 is the density for material with no porosity (theoretically dense material). Using this relationship, Eq. (A.10) can be re-written as follows:

$$c_k = \rho_0 (1 - \varphi) v_k^2 . \tag{A.12}$$

This expression indicates that two factors contribute to the dependence of modulus on porosity – porosity itself as well as the measured variations of wavespeed with porosity.

A.2.3.3. Laser Ultrasonics

Conceptually, laser ultrasonic methods should provide the same information as other ultrasonic measurement techniques when modulus measurements are made. However, unlike contacting, piezoelectric-based transducers, laser ultrasonic methods do not require the use of liquid/gel couplants that can permeate the material and bias measurements. Also, since these types of couplants are not used, laser-based ultrasonic sensors can potentially be used in inspection systems to assess the state of nuclear graphites in service environments. Some preliminary understanding of the use of laser ultrasonic methods for ultrasonic assessment of graphites is needed in order to develop these types of systems – the results presented in this work demonstrate, in a broad fashion, the use of these methods.

Laser ultrasonic measurements were completed using the system shown schematically in Fig. A.4. A pulsed, Nd:YAG laser producing 8-10 ns pulses at 1064 nm with energies in excess of 300 mJ served as the source for the ultrasonic transmitter. These pulses were attenuated and focused on the sample surface so that material ablation was not observed after initial surface conditioning. The resulting ultrasonic transmitter produced ultrasound characteristic of a thermoelastic source with amplitudes that

permitted detection at various locations on a given sample. Laser ultrasonic sources of this type excite multiple ultrasonic modes (longitudinal, shear, surface and lateral waves) each having broad frequency content. Representative waveforms corresponding to the graphites highlighted in Fig. A.1 are shown in Fig. A.5 to illustrate the nature of the signals recorded using this type of instrumentation. Fourier transforms of recorded ultrasonic transients show that signals contain significant energy from quasi-static frequencies up to ten(s) of megahertz – the upper limit being related primarily to characteristics of the material under study.

All measurements were performed in an epicentral geometry – the transmitter being located directly opposite the receiver on different sides of the sample. The receiver was a Michelson-type, path stabilized interferometer (shown schematically in Fig. A.4) with a diode-pumped, frequency-doubled Nd:YAG laser (532 nm). The effective operating bandwidth of this instrument was approximately 20 kHz to 50 MHz – more than sufficient to capture the ultrasonic transients at the reception location. When used for ultrasonic measurements in graphite, this type of system might appear to have various shortcomings. First, even though graphite is black and is strongly absorptive at the wavelengths used for excitation, the ultrasonic transients launched by a thermoelastic source might not be large enough to detect owing to the low thermal expansion coefficient for graphite. Fortunately, all graphites examined in this work proved to be quite good ultrasonic transmitters owing to the interaction between the source laser beam and the graphite (specific details regarding optical absorption, photothermal energy conversion and the character of the resulting ultrasonic source will not be considered here). Next, since graphite is black and absorbs quite well in the visible portion of the spectrum, optical reception using the interferometer might appear to be a poor choice. However, when polished to an optical finish, the front surface reflection from graphite can be quite strong and provides more than enough optical return for interferometric detection of ultrasound.

The ultrasonic measurements reported in this work were used to determine the longitudinal and shear moduli of various graphite samples (with Young's modulus being derived using standard relations for isotropic materials). These moduli were computed using measured times-of-flight from laser ultrasonic waveforms along with measurements of sample thickness and density. Density measurements were performed using simple measurements of sample dimensions (to compute volume) along with sample mass determinations. It was found that this approach to density measurement yielded more consistent results than those obtained using water displacement methods. The principal uncertainty in making modulus measurements using this approach is determination of the times-of-flight for the various ultrasonic arrivals since the waveforms are complicated and must be correctly interpreted. Modeling can assist the interpretation process but cannot completely reproduce all aspects of recorded signals. Consequently, times-of-flight measurements have been made on ultrasonic arrivals that relate to single

transits through the sample. When possible, revivals (corresponding to multiple transits through the thickness) have also been used to refine measurements since these permit pulse-echo overlap estimates for times-of-flight.

A.3. Ultrasonics Results and Analysis of Modulus Variation with Porosity and Microcracking

A.3.1. Ultrasonics Results

Results of laser ultrasonic measurements are summarized in Table A.1 and in Fig. A.6 where the longitudinal and shear moduli for all samples are presented as a function of material mass density. The designations for the various graphites are commonly used in the literature and details regarding each can be found in various reports [A9,A39]. The graphical presentation in Fig. A.6 has been chosen since it illustrates a clear trend for graphite stiffness as a function of material density even though the only commonalities among the graphites are, presumably, their chemical purity and the general processes used during material synthesis. This is true except for BAN which has processing steps that differ significantly from other nuclear graphites resulting in altered properties of this graphite relative to others [A40]. Linear trend lines fit to the data (excluding values for BAN) are also shown since they approximate the overall variations of graphite stiffness with density. Scatter of the data about the trend lines has several sources that can be readily identified. Variations in density for a given graphite include actual variations that occur during production – some samples were taken from non-adjacent regions in billet sections – and also reflect measurement uncertainties. Variations in stiffness result from inhomogeneity in the graphite and also include effects related to graphite anisotropy (stiffness in different directions varies). The effects of inhomogeneity (microstructural variations) and measurement uncertainty can be estimated by comparing modulus values in graphites that are known to be relatively isotropic such as IG-110. Using values in Table A.1, the longitudinal and shear modulus measurements for the two samples included in this study differ by approximately 5%. The effects of anisotropy on reported modulus values can be estimated by examining results for an anisotropic graphite such as PCEA which is extruded and should exhibit transversely isotropic behavior. Three different samples of PCEA were used in this study with samples being fabricated with surface normals for corresponding faces that were orthogonal to one another. With these sample orientations, two of the longitudinal moduli listed in Table 1 should have the same value – two values differ by approximately 3% while the third differs from the other two by approximately 6-9%. Interpretation of the shear modulus values obtained for the three PCEA samples is more problematic since the measurement results reported were not obtained using linearly polarized shear waves – laser ultrasonic shear waves from the sources used in this work were essentially radially polarized and this necessarily results in mixed shear modes in the received waveforms for two of the PCEA measurements. Even so, owing to symmetry considerations, two of the shear modulus measurements should be equal and the third should differ just as was the case for the longitudinal wave.

For PCEA, two of the shear modulus values differ by approximately 7% while the third differs from the other two by 13-19%. These observations indicate that uncertainty related to microstructural variations (not related to anisotropy) combined with measurement uncertainty leads to several percent variation in the longitudinal modulus and approximately 7% variation in the shear modulus. Anisotropy accounts for an additional 3-6% variation for the longitudinal modulus and 6-12% for the shear modulus. For the purposes of this presentation, this anisotropy will not be considered in detail since the measurements in different directions will simply provide additional scatter to the data. Presumably, the trend lines simply provide an indication of the average modulus that might be realized for any given density (or similarly the average density for any given modulus) if an exhaustive sampling of microstructures were available for characterization. Since the sampling of microstructures is necessarily incomplete, the functional forms for trend lines must be assumed to be correct in order to analyze the data successfully.

A.3.2. Variation of Modulus with Bulk Porosity

As the graphite micrographs in Fig. A.1 illustrate, nuclear graphites are porous and it is well known that porosity plays a significant role in affecting the moduli of these materials. For purposes of comparing the current results to related work in the literature, the longitudinal and shear moduli have been used to compute Young's modulus and density has been converted to porosity volume fraction (using a theoretical density of 2.26 g/cm^3). This allows Young's modulus and the shear modulus to be shown as a function of porosity – results are presented in Fig. A.7. In Fig. A.7a, the effect of grain type (based on ASTM D7219-08) on this relationship is shown by noting which graphites are fine grain (filled symbols) and which are medium grain (open symbols). The results do not show any discernable trend that indicates grain type affects material stiffness for a given density. In Fig. A.7b, the effect of coke source (pitch – filled symbols, petroleum – open symbols) is shown. Generally, graphites processed with pitch-derived coke appear to have lower porosities (on average), but coke source does not appear to influence modulus for a given density. Finally, in Fig. A.7c the effect of the forming method is shown. For the graphites studied in this work, most were formed by one of the following processes: extrusion (filled symbols), isostatic molding (open symbols) or vibromolding (crossed symbols). While it appears that vibromolding produces materials with the lowest porosity, no clear trend between the forming method and modulus emerges for graphites of a particular density. The absence of clear and identifiable effects of grain type, coke source or forming method on modulus as a function of density (for this sample set) indicates that the primary factor affecting material stiffness is porosity. In Fig. A.8, all modulus data are presented without additional identification and will be analyzed as a single data set representing a statistical sampling of graphite modulus as a function of porosity.

Results are shown with linear and exponential trend lines that are fit to the data. The functional form for the linear fit is suggested by the model developed by Hashin and Shtrikman and is supported by

previous studies of particular graphites that have shown modulus values that vary nearly linearly with porosity [A13,A19,A41] while the exponential fit is suggested by work presented by Cost *et al.* [A19]. Again, the porosity derived here is related to measurements of sample masses and volumes and does not include contributions to porosity that might be measured using other techniques such as BET surface area measurements that would involve all accessible surfaces – including those associated with open microcracks. Given the richness of graphite microstructure, it is interesting that overall trends exist for the data gathered across the range of graphites in this study even though porosity was not intentionally varied. In contrast, the results presented by Cost *et al.* [A19] and by Shibata *et al.* [A41] were for particular graphites in which porosity was intentionally varied to assess related effects on graphite stiffness. By focusing on particular graphite types, these studies yielded stiffness values that included far less scatter than is the case for the results presented here.

It should be noted that the correlation coefficients for the various fits shown in Fig. A.8 are quite poor, but this should be expected since the approach taken here is based on a statistical interpretation of the data. The trends are based on models for the relationship between porosity and modulus and the random scatter of points about the trend line represents the variations in microstructure (for a given porosity) that can give rise to different values for modulus. The results here suggest that there exist general relationships between graphite porosity and moduli that might be used to obtain further insight into the structure-property relationships in these materials. This statement is particularly applicable for a given graphite since the underlying microstructure will not display the variability of the sample set contained in this work.

A.3.3. Modulus of "Theoretically Dense" Nuclear Graphite

Using the models for modulus variation with porosity, the results in Fig. A.8 permit estimates for the moduli of theoretically dense nuclear graphite by noting the intercepts with the modulus axis. This general procedure was used by Cost *et al.* who inferred that a fully dense version of the graphite they studied would have a Young's modulus of 25.5 GPa and a shear modulus of 9.7 GPa. Employing their use of an exponential fit with the measured results here yields values of 24.4 GPa and 10.1 GPa for the respective moduli. Using the linear fit, the moduli would be 18.8 GPa and 7.6 GPa. These experimentally-based estimates provide some indication of the expected moduli for a generalized, polycrystalline, theoretically dense graphite that contains microcracks. As was outlined previously, estimates for the effective crack density can be made by using these values along with the models for the moduli of materials containing microcracks. To complete this analysis, Eqs. (A.6) and (A.7) require values for the moduli of theoretically dense, uncracked, polycrystalline graphite, but these are unknown presumably owing to the inability to produce materials with these characteristics. Values for these moduli

will be taken from models that use well-known values for the single crystal stiffness tensor to compute the corresponding moduli of polycrystalline materials with randomly-oriented grains.

Unfortunately, theoretical estimates for the moduli of polycrystalline graphite are particularly difficult to obtain owing to the extremely high elastic anisotropy displayed by single crystal graphite. The difference between the upper bound (based on Voigt averaging) and the lower bound (based on Reuss averaging) for Young's modulus is nearly 500 GPa [A42]. The corresponding difference for the shear modulus is approximately 210 GPa [A42]. Clearly, these differences suggest some care must be taken in selecting the model that is used to estimate the theoretical stiffness of fully dense, crack-free, polycrystalline graphite. Among the models that could be used – Reuss, Hashin-Shtrikman, Kröner, Kiewel-Bunge-Frische, Voigt [A42] – the Reuss and Voigt models rarely yield accurate modulus values for materials having microstructural elements that are randomly oriented in three dimensions and this suggests that one of the other models should be used. For subsequent analysis in this work, we will use the lower bound estimate based on the generalized approach developed by Hashin and Shtrikman since it provides the lowest values that might accurately predict the moduli for materials with complicated, three-dimensional microstructures [A22]. The lower limit values for Young's modulus and the shear modulus in graphite are 39.9 GPa and 14.9 GPa respectively for this model [A42]. These values represent the moduli for uncracked material (E_0 and G_0 in Eqs. (A.6) and (A.7)) and can be used to estimate effective crack densities. Using the experimentally-based estimate for Young's modulus in a theoretically dense, microcracked material (18.8 to 24.4 GPa) along with the value from the corresponding crack-free material (39.9 GPa), Eq. (A.6) can be used to compute an effective crack density of $0.35 \le \chi_E \le 0.67$ where the subscript indicates that this estimate is based on Young's modulus. The corresponding estimate based on the shear modulus (7.6 to 10.1 GPa for microcracked versus 14.9 GPa for uncracked material) yields $0.48 \le \chi_G \le 0.95$ – the subscript indicates that this estimate relates to the shear modulus. These estimates for the effective crack density provide some indication of the degree of microcracking in the microstructure of a generalized, nuclear graphite material.

A.3.4. Estimation of Microcrack Number Density

The interpretation of the effective crack density (crack energy density coefficient) is problematic since it involves parameters related to the crack size as well as the crack population number density. However, it should be noted that the quantity associated with crack geometry ($\pi w^2 l$) can be computed using measurements of microcrack dimensions so that the corresponding population number densities can be estimated. These dimensions appear to be related to the various components of the graphite microstructure including the binder phase and filler particles and range from tens of nanometers to several micrometers [A43-46] and can be roughly equal to pore diameters in various graphites (such as IG-110).

This relationship permits an interesting comparison between pore and crack population densities. If microcrack dimensions are $l = 10w$ with $l = \pi R / 4$ then Eq. (A.9) indicates that there are roughly $275 \times (\chi / \varphi)$ cracks per pore. If the effective crack density is taken to be in the range $0.48 \le \chi \le 0.67$ (based on the overlap of the ranges obtained previously) and porosity is taken to be $\varphi \approx 0.2$ (the average for the graphites included in this study), then there should be approximately 660 to 920 microcracks per pore. This estimate for microcrack density (for the assumed crack size) represents a lower bound and would be higher if the theoretical modulus for graphite were to exceed the lower bound predicted using the Hashin-Shtrikman model. The overall conclusion from this analysis is that there are many more cracks per unit volume in graphite than there are pores. This result is partly supported by SEM micrographs presented by Wen *et al.* [A23,A45] and Zheng *et al.* [A46] as well as by TEM results given by Chi and Kim [A43,A44] that show many cracks per pore. Clearly, if the estimate for microcrack density were 10^{-2} per pore or 10^{6} per pore, then the overall analysis suggested here would be suspect – it is remarkable that a physically meaningful result is obtained with a minimum of information.

A.4. Discussion

There are various points developed in this work that deserve additional consideration. Among them is the method used to identify moduli for fully dense graphite. The choice to use linear and exponential fits to the modulus versus porosity plots was based on inspection of various models presented in the literature as well as on previous analysis by other researchers who experimentally examined the relationship in more detail. Whether the functional variation was assumed to be linear or exponential, the primary result to be extracted from the analysis was the modulus at zero porosity – no physical significance was assigned to the derivatives of the curves. However, the model developed by Hashin and Shtrikman, given in Eqs. (A.1) and (A.2), provides a more detailed description that was not used to evaluate the data, but could be used in a more robust analysis since the shape of the modulus versus porosity curve depends on the modulus at zero porosity – the derivatives of the curve are linked to the intercept – and, as a result, *two moduli can be extracted as fitting parameters from a single curve of modulus versus porosity*. As appealing as this might be, neither the least-squares fit of Eq. (A.1) to data for Young's modulus nor the least-squares fit of Eq. (A.2) to the shear modulus data was acceptable since both yielded non-physical results for the Lamé constant λ – the reason for this is a subject for additional investigation.

Moving from porosity to microcracking, a major assumption in the analysis involved choices for the moduli of nonporous and crack-free, polycrystalline graphite (E_0 and G_0). In the analysis, the lower bound moduli suggested by Hashin and Shtrikman were used. Measurements of graphite modulus as a function of neutron dosage or as a function of applied pressure can add support to these choices since both

can close microcracks (decreasing their contribution to the overall elastic energy state) and increase the measured stiffness of graphite. While these types of experiments have not been performed on the samples used in this study, related work has shown that Young's modulus increases considerably when irradiated with neutrons. Work by Bradford and Steer on neutron-irradiated Gilsocarbon graphites indicated that "structure" related changes to Young's modulus caused the stiffness of these materials to rise from 15-20 GPa to a maximum of 35-45 GPa [A.16]. Within the context of this discussion, the increase in modulus (~ 20 GPa) might be attributed to the closing of microcracks in the material. This type of closing has been observed by Wen *et al.* for Mrozowski cracks in nuclear graphites irradiated with electrons [A.23] and the increase in modulus measured by Bradford and Steer is very close to the difference between the microcrack-free modulus and the zero-porosity modulus assumed for the graphites included in the current study (roughly 15-20 GPa). Work by Ishiyama *et al.* on IG-110 showed that Young's modulus increased by a factor of approximately 2.5 as a result of neutron irradiation [A.14]. Given an initial value of 10.2 GPa, the maximum would be approximately 25 GPa yielding a 15 GPa increase that could be attributed to closing of microcracks – again, in the range of assumptions made here. In addition, the work by Bradford and Steer as well as that by Ishiyama *et al.* showed that tensile strength reached maximum values at neutron dosages that also produced maximum values for Young's modulus. This type of behavior in brittle materials is consistent with crack closing/elimination since stress intensity factors and modulus both depend directly on crack size [A.47,A.48].

In order to estimate the effective crack density for a particular graphite grade (or sample) using the procedure outlined in this work, some method for altering porosity would be needed to obtain values for the modulus at zero porosity. Porosity can be increased through oxidation processing, but this affects graphite microstructure in more ways than simply increasing pore size and/or number density since filler and binder phases oxidize at different rates [A.7]. This preferential processing of the microstructure ultimately affects the size and distribution of pores and likely affects the number density of microcracks, but this has not been verified. A more direct route to estimating microcrack populations is to assess changes in modulus brought about by crack opening or closure. This can be accomplished by imposing known stresses on the material, measuring changes in modulus and interpreting these changes with models that effectively represent microcrack characteristics in that graphite grade. The most effective stress state to accomplish this type of measurement would involve hydrostatic loading since this could be used to close all cracks regardless of crack orientation. Unfortunately, there do not appear to be studies that have measured the modulus of graphites under hydrostatic pressure, but studies have been performed that report variations in stiffness that have been brought about by uniaxial loading. Yoda *et al.* performed measurements of modulus on IG-11 using longitudinal ultrasonic waves propagating along the direction of loading [A.49]. Whether loading was tensile or compressive, modulus decreased with material strain,

but since strains were large (> 0.1% compressive strain, >0.03% tensile strain) permanent changes to the elastic modulus occurred – this is consistent with crack initiation/growth that would increase the crack volume fraction. The measurements made by Yoda *et al.* during compression are particularly interesting since they show reduction in modulus as well as some recovery of modulus (perhaps 5-10%) during sample unloading. While the absolute reductions can be related to increased crack volume fraction, recovery indicates that some type of reversible (elastic) change to the microstructure occurred during loading/unloading. Within the context of microcracking, this change can be related to crack closure processes that effectively change the crack volume fraction sensed by ultrasound. More recently, Bodel has performed measurements of modulus on nuclear graphites using longitudinal ultrasonic waves propagating along as well as transverse to the direction of loading [A.50]. All measurements were made using compressive loads (< 70 MPa). In Gilsocarbon, Bodel found that modulus decreased with increasing load and irreversible changes to modulus occurred during initial loading. Subsequent loading/unloading cycles primarily showed reversible changes to modulus with higher compressive loads yielding lower modulus values. These results as well as others presented by Bodel are consistent with the influence of microcracks on modulus in graphite materials. When taken together, the studies by Yoda *et al.* and Bodel along with the results of this work show that microcracking effects on modulus in graphite can potentially be isolated from other factors. While quantitative models have not been developed or verified to interpret these types of measurements, directions for future work are indicated by the results presented here.

A.5. Conclusions

In this work, laser ultrasonic methods have been used to measure the stiffness in a selection of nuclear graphites. Measurements were made to assess wavespeeds for longitudinal and shear waves in different propagation directions in the graphite samples and these were converted to effective longitudinal and shear moduli using determinations of sample density. Using these moduli, Young's modulus was computed. Overall trends for these moduli indicated that they increased with graphite density or, put another way, decreased with graphite porosity. These trends could be interpreted using linear and exponential fits to the data and this is consistent with various models in the literature that have been used to model variations of modulus with porosity at low porosity volume fractions. Extrapolations of these fits to zero porosity were used to infer the moduli for theoretically dense graphite. These values were far below those expected based on various models that have been developed in the literature to predict the moduli of fully dense, polycrystalline, isotropic graphite. This discrepancy could be interpreted as being related to microcracking in the graphite microstructure. Models have been used to estimate the microcrack number densities that would be necessary to account for the behavior of the graphites in this study and results indicate that hundreds of microcracks per pore would be needed to reduce graphite

stiffness from predicted values to those inferred from measurements. This is reasonable given the microstructures observed in various graphites. Furthermore, results reported in the literature are consistent with the influence of microcracking on elastic stiffness and could be interpreted using concepts developed here. Additional experiments are needed to quantify the relationship between modulus and microcrack densities and these should be developed using more accurate models that include microcrack orientation distributions. Having these types of structure-property relationships should allow for more sophisticated characterization of nuclear graphites using ultrasonics methods.

References

[A1] A.N. Jones, G.N. Hall, A. Hodgkins, K. Wen, T.J. Marrow, B.J. Marsden, J. Nucl. Mater. 381 (2008) 152-157.

[A2] "HTGR Technology Course for the Nuclear Regulatory Commission, Module 9, Graphite," Idaho National Laboratory and Oak Ridge National Laboratory, May 24-27, 2010; https://inlportal.inl.gov/portal/server.pt/directory/nrc_training_presentations/2683?DirMode=1; retrieved October 14, 2014.

[A3] A.A. Amadieh, H.A. Rafizadeh, Phys. Rev. B 7 (1973) 4527-4537.

[A4] T. Burchell, J. Strizak, M. Williams, "AGC-1 Specimen Pre-irradiation Data Report," ORNL/TM-2010/285, October 26, 2010.

[A5] J. Kane, C. Karthik, D.P. Butt, W.E. Windes, R. Ubic, J. Nucl. Mater. 415 (2011) 189-197.

[A6] C.I. Contescu, "Effect of Air Oxidation on Pore Structure Development and Mechanical Properties of Nuclear Graphite," ORNL/TM-2010/197, September 2010.

[A7] P. Wang, C.I. Contescu, S. Yu, T.D. Burchell, J. Nucl. Mater. 430 (2012) 229-238.

[A8] C.I. Contescu, R.W. Mee, P. Wang, A.V. Romanova, T.D. Burchell, J. Nucl. Mater. 453 (2014) 225-232.

[A9] T. Burchell, R. Bratton, "Graphite Irradiation Creep Capsule AGC-1 Experimental Plan," ORNL/TM-2005/505, May 27, 2005.

[A10] T.D. Burchell, J. Nucl. Mater. 381 (2008) 46-54.

[A11] J.L. McDuffee, T.D. Burchell, D.W. Heatherly, K.R. Thoms, J. Nucl. Mater. 381 (2008) 119-123.

[A12] T. Shibata, M. Ishihara, Nucl. Eng. and Design 203 (2001) 133-141.

[A13] T. Shibata, J. Sumita, T. Tada, S. Hanawa, K. Sawa, T. Iyoku, J. Nucl. Mater. 381 (2008) 165-170.

[A14] S. Ishiyama, T.D. Burchell, J.P. Strizak, M. Eto, J. Nucl. Mater. 230 (1996) 1-7.

[A15] E.D. Eason, G.N. Hall, B.J. Marsden, G.B. Heys, J. Nucl. Mater. 436 (2013) 201-207.

[A16] M.R. Bradford, A.G. Steer, J. Nucl. Mater. 381 (2008) 137-144.

[A17] T. Burchell, R. Bratton, W. Windes, "NGNP Graphite Selection and Acquisition Strategy," ORNL/TM-2007/153, September, 2007.

[A18] C. Karthik, J. Kane, D.P. Butt, W.E. Windes, R. Ubic, Microsc. Microanal. 18 (2012) 272–278.

[A19] J.R. Cost, K.R. Janowski, R.C. Rossi, Phil. Mag. 17 (1968) 851-854.

[A20] J. Takatsubo, S. Yamamoto, Trans. Jpn. Soc. Mech. Eng. A 60 (1994) 224-229 (in Japanese).

[A21] Z. Hashin, S. Shtrikman, J. Mech. Phys. Solids 10 (1962) 343-352.

[A22] Z. Hashin, S. Shtrikman, The Franklin Institute Laboratory April 1962, 336-341.

[A23] K. Wen, J. Marrow, B. Marsden, J. Nucl. Mater. 381 (2008) 199-203.

[A24] S. Crampin, Geophys. J. Int. 118 (1994) 428-438.

[A25] S. Crampin, S.V. Zatsepin, Geophys. J. Int. 129 (1997) 495-506.

[A26] S. Crampin, S. Peacock, Wave Motion 41 (2005) 59-77.

[A27] B. Budiansky, R.J. O'Connell, Int. J. Solid Structures (1976) 81-97.

[A28] J.R. Rice, J. of Applied Mechanics 35 (1968) 379-386.

[A29] C.M. Sayers, Ultrasonics 26 (1988) 73-77.

[A30] C.M. Sayers, Engineering Fracture Mechanics 35 (1990) 743-749.

[A31] C.M. Sayers, M. Kachanov, J. Geophysical Res. 100(B3) (1995) 4149-4156.

[A32] M. Kachanov, Int. J. Solids Structures 23 (1987) 23-43.

[A33] C. Mauge, M. Kachanov, J. Mech. Phys. Solids 42 (1994) 561-584.

[A34] C. Mauge, M. Kachanov, International Journal of Fracture 65 (1994) 115-139.

[A35] X. Wang, G.A. Gazonas, M.H. Santare, Int. J. Fract. 158 (2009) 27-40.

[A36] X. Wang, M.H. Santare, G.A. Gazonas, Eng. Fract. Mech. 76 (2009) 1910-1919.

[A37] D. Su, M.H. Sanatare, G.A. Gazonas, Eng. Fract. Mech. 75 (2008) 4104-4116.

[A38] Z. Zheng, Int. J. Rock Mechanics and Mining Sciences 37 (2000) 39-49.

[A39] J.P. Strizak, T.D. Burchell, W.E. Windes, "Status of Initial Assessment of Physical and Mechanical Properties of Graphite Grades for NGNP Applications," ORNL-GEN4/LTR-06-023, September 5, 2006.

[A40] D. Miller, I. Lewis, M. Santana, acs.omnibooksonline.com/data/papers/2004_K003.pdf, retrieved July 27, 2015.

[A41] T. Shibata, T. Tada, J. Sumita, K. Sawa, J. Solid Mech. and Mat. Eng. 2 (2008) 166-175.

[A42] H. Kiewel, H.J. Bunge, L. Fritsche, Textures and Microstructures 28 (1996) 17-33.

[A43] S.-H. Chi, G.-C. Kim, Transactions of the Korean Nuclear Society, Spring Meeting, May 25-26, 2006.

[A44] S.-H. Chi, G.-C. Kim, J. Nucl. Mater. 381 (2008) 98-105.

[A45] K.Y. Wen, T.J. Marrow, B.J. Marsden, Carbon 46 (2008) 62-71.

[A46] G. Zheng, P. Xu, K. Sridharan, T. Allen, J. Nucl. Mater. 446 (2014) 193-199.

[A47] G.R. Romanoski, T.D. Burchell, in *Carbon Materials for Advanced Technologies*, ed. T.D. Burchell, Pergamon, 1999, pp. 502-514.

[A48] J. Chapman, "Testing of Small Graphite Samples for Nuclear Qualification," INL/EXT-10-20275, November 2010.

[A49] S. Yoda, M. Eto, T. Oku, J. Nucl. Mater. 119 (1983) 278-283.

[A50] W. Bodel, "The Relationship between Microstructure and Young's Modulus of Nuclear Graphite," Ph.D. dissertation, The University of Manchester, Manchester, UK, 2012.

Table A.1: Grade, Density and Elastic Moduli of Nuclear Graphite Samples

Graphite	Density (g/cm^3)	Longitudinal Modulus (GPa)	Shear Modulus (GPa)	Young's Modulus (GPa)	Grain Type*	Coke Type	Forming Method	Source
HLM	1.76	10.84	3.44	8.72	medium grain	Petroleum	Extruded	SGL Carbon / USA
HLM	1.74	9.93	2.85	7.40				
H-451	1.73	11.98	3.81	9.66	medium grain	Petroleum	Extruded	SGL Carbon / USA
H-451	1.72	11.40	3.56	9.06				
H-451	1.67	11.38	4.41	10.44				
IG-110	1.71	8.81	2.71	6.94	fine grain	Petroleum	Isostatically Molded	Toyo Tanso / Japan
IG-110	1.71	9.28	2.87	7.32				
IG-430	1.83	10.86	4.23	9.99	fine grain	Pitch	Isostatically Molded	Toyo Tanso / Japan
IG-430	1.83	12.32	4.68	11.18				
NBG-10	1.79	13.53	5.93	13.16	medium grain	Pitch	Extruded	SGL Carbon / France
NBG-10	1.79	14.12	5.53	13.03				
NBG-10	1.81	15.05	5.64	13.54				
NBG-17	1.88	14.18	4.44	11.29	medium grain	Pitch	Vibromolded	SGL Carbon, Germany / France
NBG-17	1.87	15.94	4.63	12.00				
NBG-18	1.88	12.91	4.78	11.53	medium grain	Pitch	Vibromolded	SGL Carbon, Germany / France
NBG-18	1.88	13.00	4.04	10.29				
NBG-18	1.87	13.63	5.15	12.33				
NBG-18	1.84	13.41	4.56	11.34				
NBG-25	1.85	13.36	4.67	11.50	fine grain	Petroleum	Isostatically Molded	SGL Carbon, Germany / France
NBG-25	1.85	13.76	4.87	11.95				
PCEA	1.75	10.33	3.91	9.34	medium grain	Petroleum	Extruded	GrafTech Intl. / USA
PCEA	1.75	9.42	3.41	8.30				
PCEA	1.80	10.03	4.19	9.56				
PCIB	1.86	13.62	4.77	11.74	fine grain	Petroleum	Isostatically Molded	GrafTech Intl. / USA
PCIB	1.88	13.70	4.71	11.66				
PGX	1.77	9.92	3.38	8.39	medium grain	Petroleum	Molded	GrafTech Intl. / USA
PGX	1.78	10.10	4.28	9.70				
S 2020	1.77	13.20	5.06	12.03	fine grain	Petroleum	Isostatically Molded	Carbone of America / USA
S 2020	1.77	13.23	5.19	12.22				
BAN	1.96	9.40	4.24	9.23	medium grain	Petroleum Other	Extruded	GrafTech Intl. / USA
BAN	1.96	10.55	3.60	8.93				

* Grain type designation based on ASTM D7219-08, "Standard specification for isotropic and near-isotropic nuclear graphites", ASTM International, West Conshohocken, PA 19428-2959, USA.

Note: Multiple entries in the table for the various graphite grades represent measurements made in different specimens that were cut from the source sample such that ultrasonic propagation would be in orthogonal directions. In certain cases, three entries are provided and these results were used to assess whether or not the material in the source sample was transversely isotropic.

a.

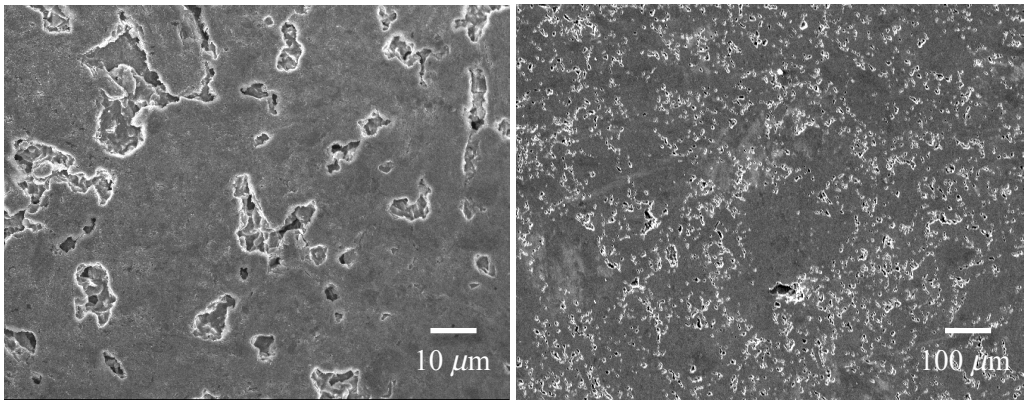

b.

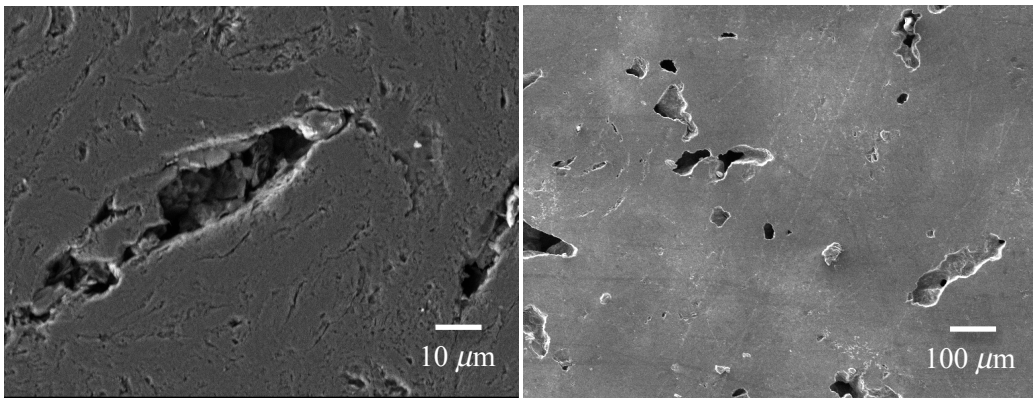

c.

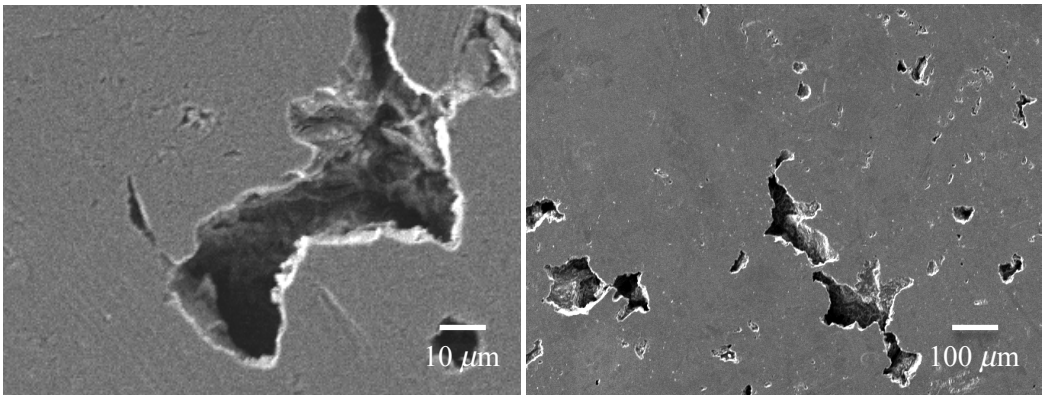

Figure A.1: Scanning electron micrographs of three different graphites used in this study: a. IG-110, b. NBG-18, c. HLM. These images highlight microstructural differences, especially porosity, among these materials.

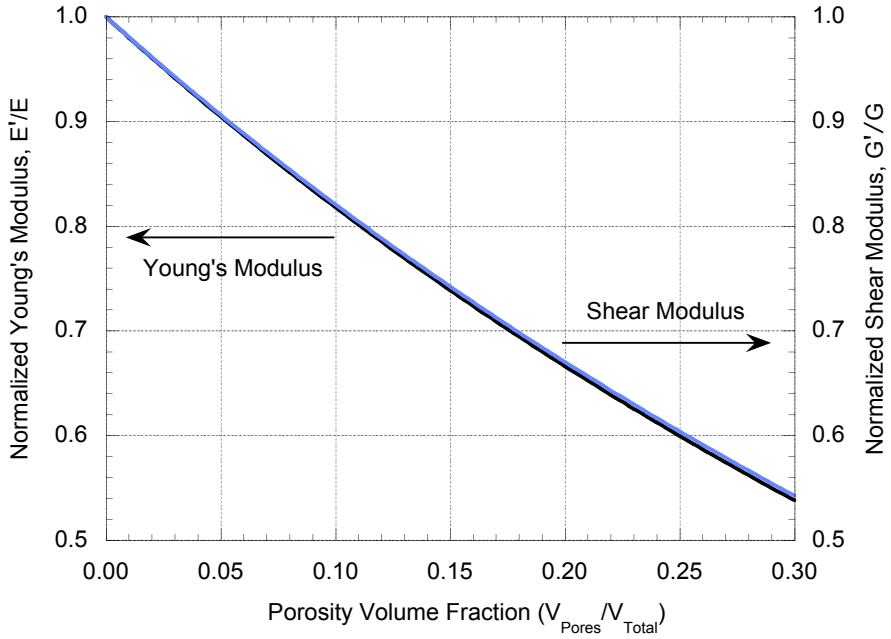

Figure A.2: Computed variation of elastic modulus with porosity volume fraction based on models developed by Hashin and Shtrikman. The moduli are normalized by values obtained at zero porosity.

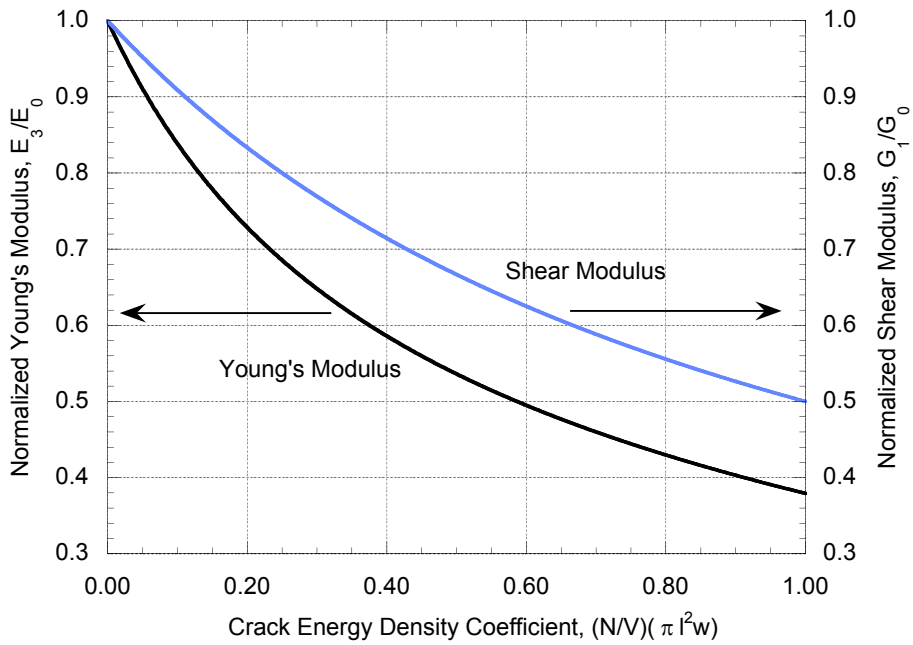

Figure A.3: Computed variation of elastic modulus with the microcrack energy density coefficient based on models presented by Zheng. This coefficient depends on crack number density, n , as well as on crack geometry.

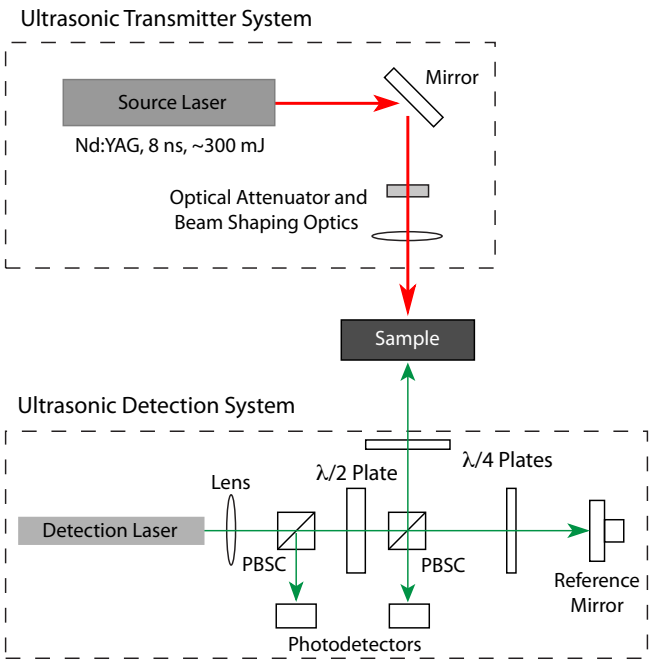

Figure A.4: Schematic illustration of the laser ultrasonic apparatus used to measure ultrasonic wave times-of-flight in nuclear graphite. The transmitter source was a pulsed Nd:YAG laser and the receiver was a path-stabilized, Michelson-type interferometer.

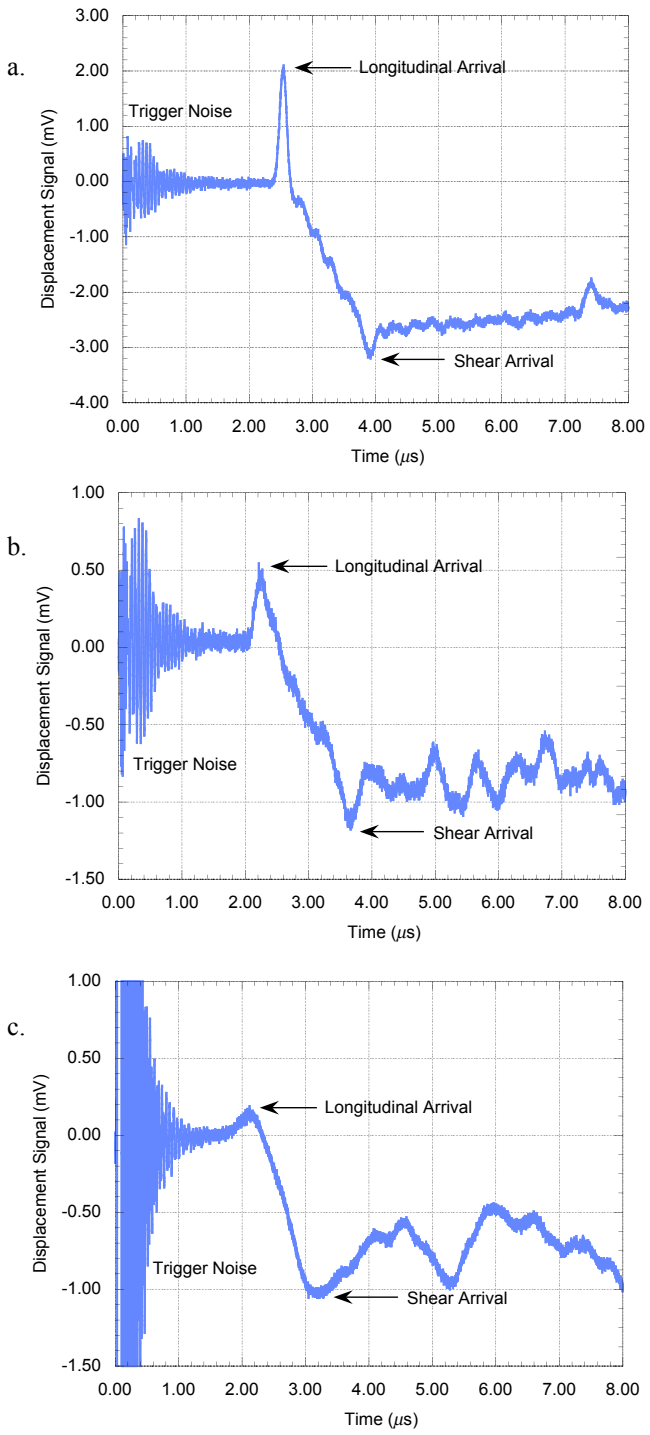

Figure A.5: Laser ultrasonic waveforms for three different graphites showing the directly transmitted longitudinal and shear wave arrivals. The trigger noise early in early in each waveform is related to the pulsing of the source laser. a. Waveform obtained for IG-110. The arrival at approximately 7.5 μs is the reflected longitudinal wave (3 transits through the sample thickness). b. Waveform for NBG-18. c. Waveform for HLM.

a.

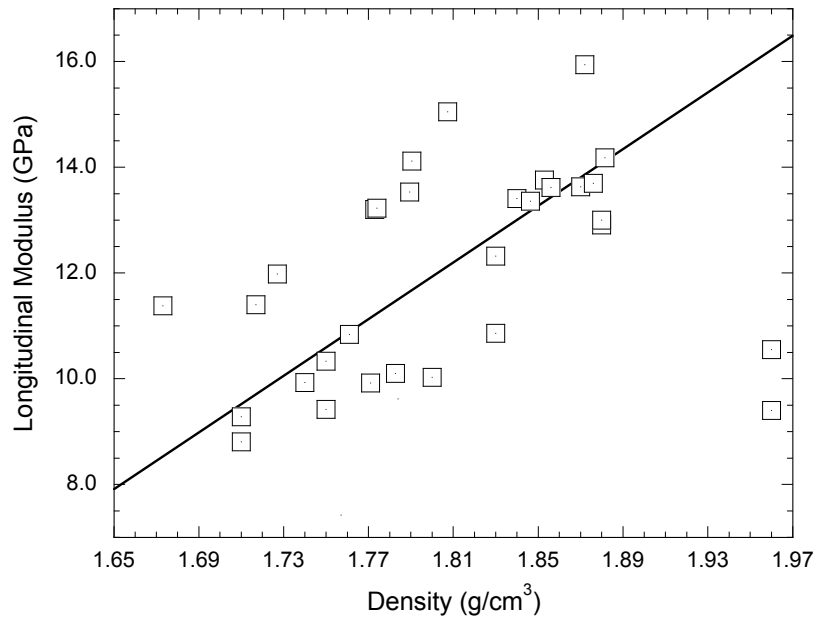

b.

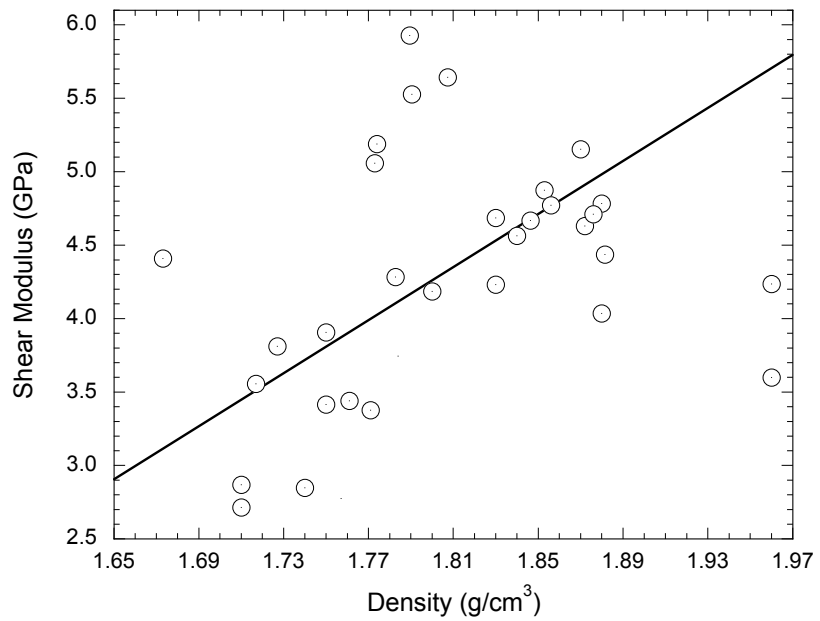

Figure A.6: a. Longitudinal stiffness of various nuclear graphites as a function of material density. b. Shear stiffness as a function of density. The solid lines in each plot represent the best fit lines to the data (omitting values measured for BAN – see text for discussion).

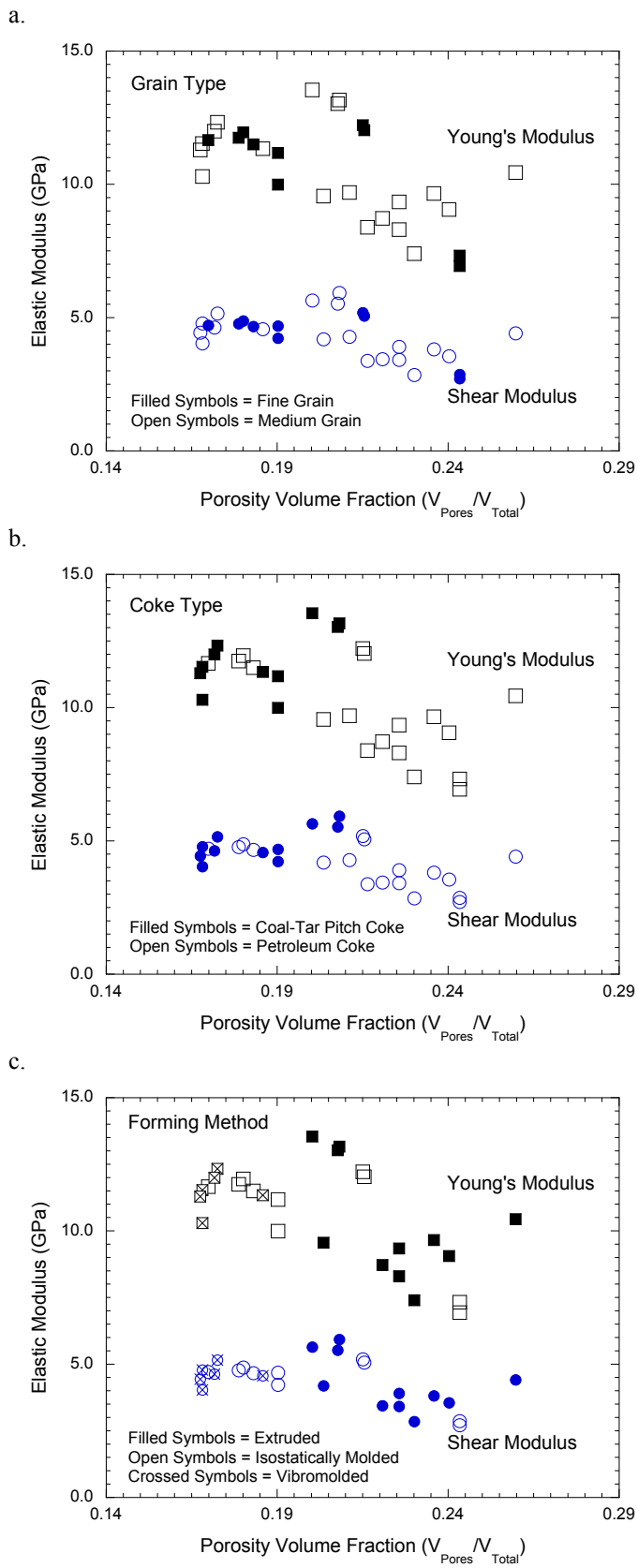

Figure A.7: Young's modulus and shear modulus (from Table 1) for nuclear graphite as a function of porosity volume fraction highlighting effects of a. grain type, b. coke source and c. forming method.

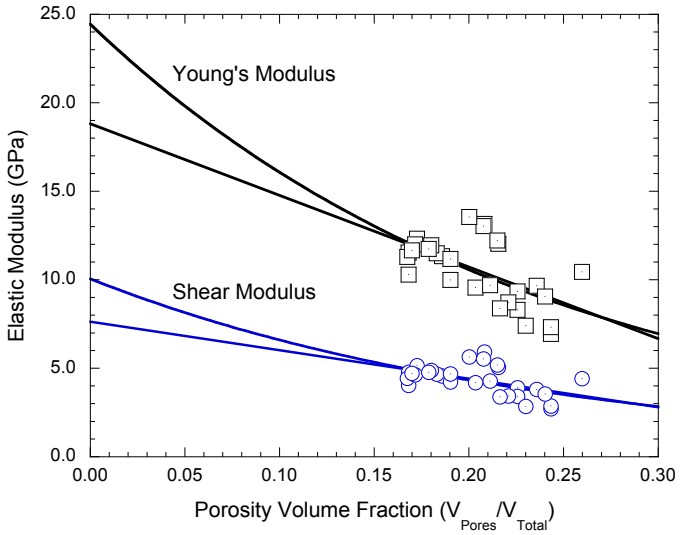

Figure A.8: Young's modulus and shear modulus for nuclear graphites as a function of porosity volume fraction. The solid lines represent linear and exponential best-fit curves to the respective data sets. The fits have been extended to zero porosity volume fraction to estimate the corresponding moduli for fully dense graphite containing microcracks.

Section B: Modeling the Effects of Oxidation-induced Porosity on the Elastic Moduli of Nuclear Graphites

B.1. Introduction

Nuclear graphite is considered to be a key material for core structures in future designs for high temperature nuclear reactors. Owing to its unique combination of material properties including high thermal conductivity, low anisotropy, high strength, and high purity, nuclear graphite can serve as an important structural element in the reactor core while at the same time acting as a neutron moderator and reflector. Even though all types of nuclear graphite are composed of the same base materials – graphite filler combined with a binder phase – the specific manufacturing processes used to produce these materials dictate the microstructural character of the final product. Operating conditions in nuclear reactors – including high temperatures, presence of oxidizing species, and high neutron flux – can also affect the material microstructure and alter the properties of graphite. In particular, the combination of high temperatures along with trace amounts of water in helium coolant for high-temperature, gas-cooled reactors can cause material oxidation. This oxidation produces material weight loss by increasing material porosity and leads to loss of graphite stiffness and strength. If oxidation leads to uniform development of porosity in the bulk of graphite components, then the effect on moduli and strength could be so high as to affect the integrity of the reactor. However, if oxidation is limited to the outside layer of graphite components, then the mechanical properties would not change deep into the core of those components. In this latter case, the reactor integrity might be ensured by suitable design of critical structural components. In any case, the health status of structural materials should be monitored using in-core structural health monitoring methods and these might include the use of remote-controlled robots equipped with ultrasonic sensors. These types of sensors would be used to determine whether or not oxidation-induced porosity reached levels that adversely affect material performance. To successfully implement this type of monitoring, it is necessary to develop structure-property relationships along with the related sensing strategies to assess the structural health of nuclear graphite and identify critical levels of damage [B1].

In particular, the relationships between elastic moduli and material density in various graphite grades have been studied by many investigators and these relationships could be used to develop sensing strategies for assessing the state of graphite components [B2-5]. Early experimental work by Cost et al. suggested that the elastic moduli had an exponential dependence on porosity. By extrapolating this experimentally-derived relationship to zero porosity, they were able to estimate the moduli of fully-dense, polycrystalline graphite [B6]. Thrower et al. also made use of an exponential dependence of Young's modulus on density to interpret results obtained on graphite oxidized in steam [B7]. An exponential function was also used by Sato et al. to fit experimental measurements of Young's modulus of graphites oxidized in air [B8]. Yoda et al. showed that a power-law could be used to describe the variation of

Young's modulus with density for graphite oxidized in air [B9] and similar power-law relationships were used by Ishiyama et al. [B10] and by Eto et al. [B11] to fit data obtained on fine-grained graphites oxidized in air. Even though these functional forms can be used to describe the relationship between modulus and porosity (or density) in nuclear graphites, the physical basis for these has not been established. Shibata et al. have developed a physical model to interpret modulus measurements in oxidized graphite to assist in the development of an ultrasonic method to nondestructively evaluate porosity levels [B12,B13]. Basing their model on interactions between pores and the ultrasonic field, they have successfully used this model to fit experimental results, but it has limits of applicability that prevent its use at low porosities. More robust models describing the relationship between modulus and porosity are needed and these should be based on the physical behaviors of polycrystalline graphite.

While computationally-based models could be developed to investigate this structure-property relationship, these models generally require a detailed, multiscale understanding of the material structure to capture information that is needed to accurately predict material behavior. Various researchers have studied the microstructures that are present in nuclear graphites [B14-16]. The results of these types of studies show that these materials contain an impressive range of microstructural features that arise from the combination of filler and binder materials. Beyond these graphite-bearing phases, the processing techniques used to produce nuclear graphites result in pores and cracks/microcracks that figure prominently in the physical behaviors of these materials. Even though much is known about the phases and defects that are present, it is not clear if the physical behaviors of these are understood sufficiently to build a multiscale, computational model that could be used to investigate the modulus-porosity relationship. Beyond understanding graphites in the as-received state, microstructural changes that accompany service-related conditions must be understood to effectively develop inspection methods that are based on structure-property relationships. Among these conditions, oxidation processes figure prominently since it is known that graphite can experience oxidation during normal reactor operation or as a result of air ingress. To study related chemo-physical processes, Contescu et al. [B17] developed standard methods for oxidizing graphites and these have been used to study microstructural changes that accompany oxidation in various graphite grades [B18,B19]. Perhaps the most noticeable change is the increase in porosity that occurs as a result of oxidation – the effect of this type of porosity on the elastic properties of nuclear graphites is the focus of the work presented here.

In this work, the relationships between the elastic moduli and porosity of oxidized, nuclear graphites are explored with particular focus on grades IG-110 and NBG-18. Samples of each grade underwent controlled oxidation to produce different sample densities and laser ultrasonic techniques were used to measure the elastic moduli. To interpret these experimental results, a relatively simple model for the

linear elastic response of a polycrystalline graphite material containing pores and microcracks is presented. The critical component of this model establishes a link between microscopic oxidation processes and specific changes to the graphite microstructure that selectively affect elastic response. The effect of this selective oxidation is to reduce modulus more rapidly with porosity than would occur if all elements of the graphite microstructure were oxidized at the same rate. The results of the measurements provided here along with the accompanying modeling approach could be useful in the development of sensing methods for structural health monitoring of graphite materials in nuclear reactors.

B.2. Graphite Materials and Methods

B.2.1. Nuclear Graphites: IG-110 and NBG-18

Two different grades of nuclear graphite, IG-110 and NBG-18, were chosen for this study because they are the leading candidates for future use in high-temperature, gas-cooled, nuclear reactors. Due to differences in manufacturing processes, NBG-18 and IG-110 exhibit very different microstructures and related details are summarized in Table B.1. Bulk mass densities were determined from manual measurements of sample dimensions and sample masses. Even though slight variations in dimensions can introduce error into calculations of density using these measured quantities, this method is generally more accurate than water-displacement measurements owing to the open porosity present in both types of graphite. Porosity was computed using measured mass densities along with the theoretical density of graphite, 2.26 g/cm^3. Other information about these graphite grades was obtained from the respective manufacturers.

Table B.1. Summary of Nuclear Graphites Characteristics

Graphite	Manufacturing Process	Grain size	Pore size	Density (g/cm^3)
NBG-18	Vibramolded	Max 1600 um	Large (5-30 um) and Small (.004-.1 um)	1.85
IG-110	Isostatically molded	Average 20 um	Small (.005-1 um)	1.77

The materials were obtained from Oak Ridge National Laboratory and were machined to produce plate-like samples with dimensions of 50 mm x 50 mm x 5 mm. Scanning electron microscopy (SEM) images of samples prepared from the two graphite grades are shown in Fig. B.1 using three different magnifications. At the lowest magnification, differences in the macropore structure are immediately seen and it is clear that the maximum pore size in NBG-18 is significantly larger than in IG-110. However, as the two graphites are examined on smaller lengthscales, differences between the grades are not as easily identified. While maximum pore size can affect the character of ultrasonic signals gathered in these two

grades, to a first approximation the pore size distribution does not affect determination of modulus as long as the measurement methods are designed appropriately.

B.2.2. Oxidation and Ultrasonic Sample Preparation

Controlled oxidation of a total of eight graphite samples was performed at Oak Ridge National Laboratory using an existing graphite oxidation test system and followed the procedure recommended by ASTM D-7542 [B19] except sample geometry and dimensions were altered to simplify ultrasonic examination of oxidized samples. The test system consisted of a 3-zone vertical tube furnace, a furnace temperature controller, a gas supply with flow rate controller, and an analytical balance (resolution: ±0.001 g) [B20]. Using this system, four samples each of IG-110 and NBG-18 were oxidized in air at a range of temperatures to produce varying degrees of weight loss. Four samples of each graphite were oxidized to approximately 5% and 10% weight loss at two different temperatures – IG-110 samples were oxidized at 525 °C and 575 °C while NBG-18 samples were oxidized at 500 °C and 575 °C. After oxidation and ultrasonic examination, samples were sectioned to assess the distribution and changes to the porosity through the thickness of the various samples.

SEM micrographs of sections from samples of the two graphite grades oxidized at the highest temperature are shown in Fig. B.2. These sections represent the interior of the sample approximately 12 mm from one of the lateral edges and 3 mm from the surface. The images show that the macropore structures in interior regions of these graphites remain relatively unchanged as a result of the oxidation process. Unfortunately, the quality of the images does not permit more detailed observations to be made. Beyond imaging, porosimetry measurements were made on different sections to assess variations in the micropore structure through the sample thickness. These measurements tended to indicate that porosity levels were uniform through the thicknesses of the samples and that higher oxidation temperatures did not produce near-surface enhancements of porosity when compared to the interior. Even though the transport of oxidative species through graphite depends strongly on the graphite grade, the conditions chosen in this work for oxidation-induced mass loss produced porosity changes that could be considered to be uniform through the sample thicknesses [B21]. Oxidation at temperatures higher than 650-700 °C could have been used and would have produced non-uniform oxidation and thinning of the samples [B21], but these conditions were not included in this study.

In preparation for ultrasonic measurements, one face of each sample was polished to a mirror-like finish using 1 um diamond paste to allow for ample optical reflection and the opposite face was ground using 400 grit silicon carbide paper to produce a macroscopically flat surface. This surface preparation was required to complete the ultrasonic measurements on these samples.

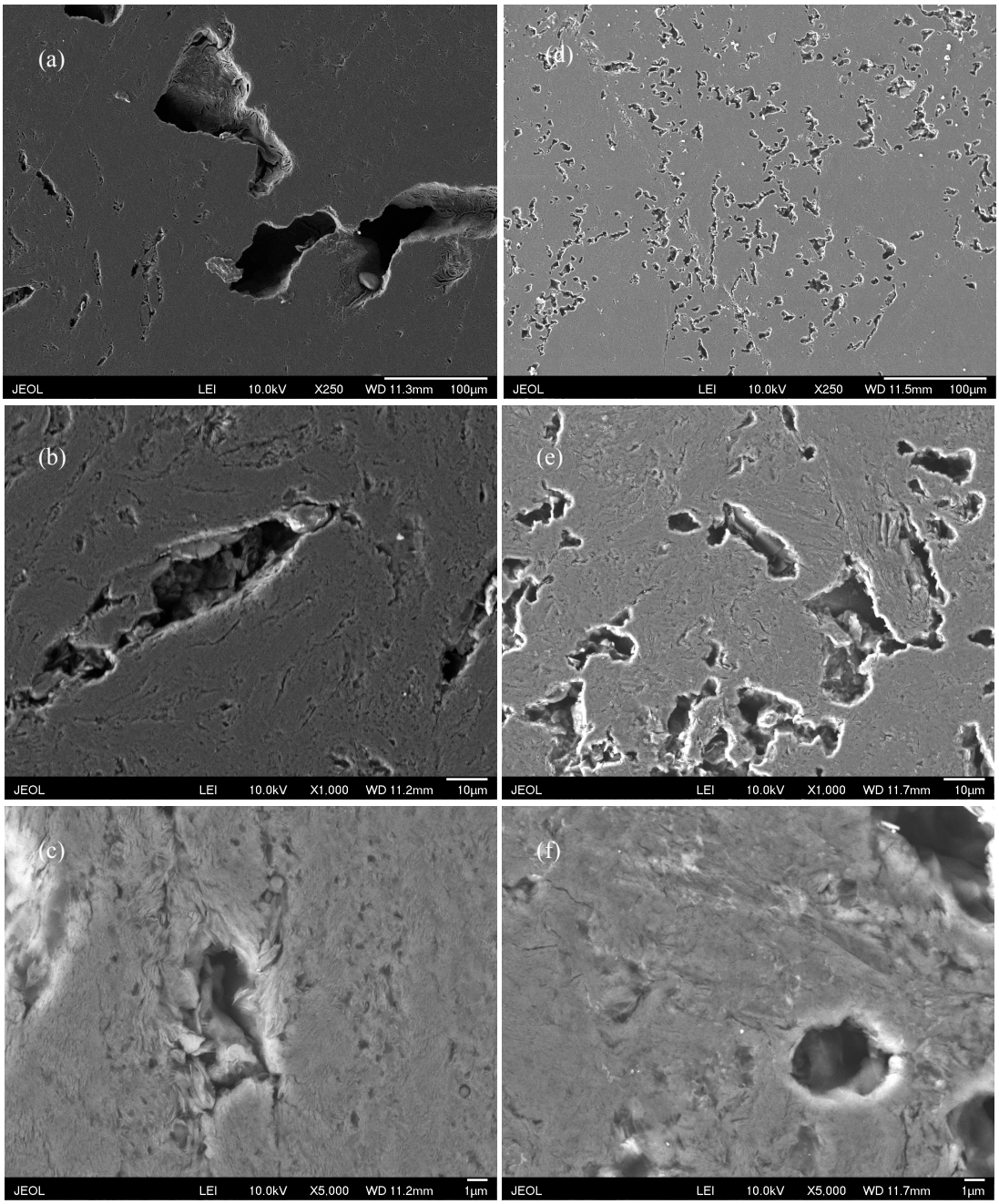

Figure B.1. Scanning electron micrographs showing microstructural features in NBG-18 (a-c) and IG-110 (d-f). At low magnifications (a and d), differences between the large scale porosity in these graphites can be seen. At higher magnifications (c and f), the microstructures of these graphites cannot be differentiated so easily using this type of imaging.

B.2.3. Ultrasonic Measurement Technique

Ultrasonic measurements were made using a non-contact, non-destructive laser ultrasonics technique [B.22]. Ultrasound was generated using a pulsed, 1064 nm Nd:YAG laser focused to a spot approximately 0.5 mm in diameter at the sample surface. The pulse from this laser (approximately 10 ns in duration) locally heated the sample surface and generated a broadbanded ultrasonic pulse that would

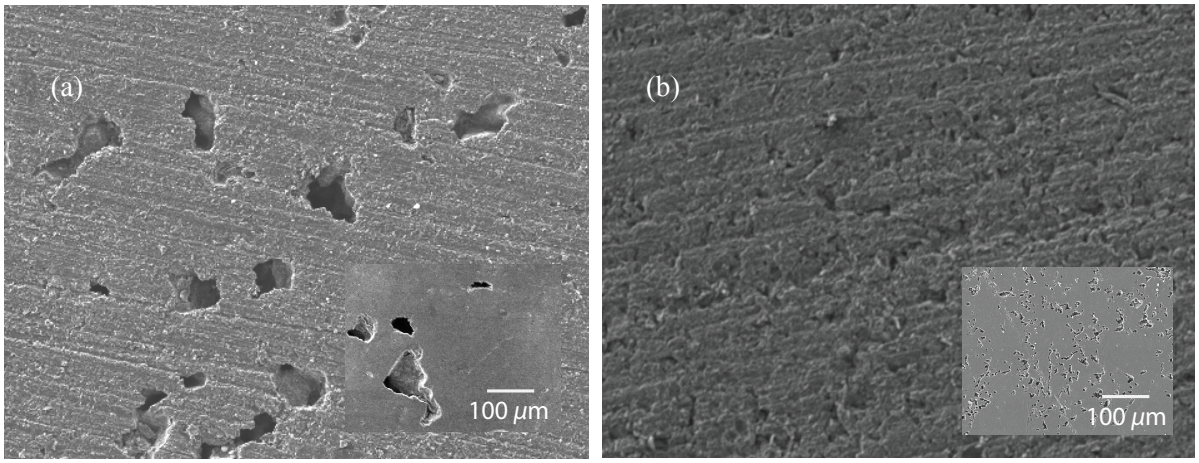

Figure B.2. Scanning electron micrographs showing large-scale porosity in (a) IG-110 and (b) NBG-18 oxidized at 575 °C. Owing to the friable nature of the material, preparation for imaging was difficult and residual polishing marks are present on the surfaces. The inset micrographs are of the unoxidized materials and are shown for comparison purposes. The scale bar shown applies to both parts of the each image.

propagate through the sample thickness. Arrival of the ultrasound on the opposing surface was detected by a path-stabilized, Michelson-type interferometer oriented directly opposite the source. Both longitudinal and shear ultrasonic waves were detected with this technique. No fewer than eight waveforms were taken for each sample from varying locations across the sample surface to account for slight variations in time-of-flight due to surface porosity.

B.3. Modeling of the Structure-Property Relationship in Graphite

There exist various approaches to modeling the variation of elastic moduli with respect to porosity in bulk graphites. The one taken here will view the graphite as a porous, polycrystalline solid composed of randomly oriented crystallites containing microcracks parallel to graphitic planes. This overall view approximates actual graphite microstructure that incorporates graphitic grains (filler) into a binder matrix. While the binder phase might not be completely graphitized, it is assumed that the primary role of residual amorphous content in the graphite is to connect adjoining crystallites and, as a result, it is elastically constrained by surrounding material. This constraint essentially reduces the influence of the amorphous carbon on the overall moduli of the graphite. To begin modeling this system, a description for the moduli of an isotropic material containing two separate phases – air and polycrystalline graphite – is needed. Next, the moduli of the polycrystalline graphite are needed and these should be based on the single crystal moduli for graphite that have been modified by the presence of microcracks. In this work, analytical models will be used to capture the essential behaviors of the graphite that are likely present with the understanding that more refined descriptions might be needed to completely and accurately capture the detailed micromechanical workings.

B.3.1. Effective Medium Theory for Two Phase Materials

Effective medium theories have been developed to describe the properties of materials with multiple, distinct phases. The central assumption underlying these theories is that the measurement processes used to characterize the material is not influenced by the scale of the phases and, as a result, the measured properties correspond to those that would be expected for a homogeneous material that effectively represents the overall behaviors of the multiphase material. The challenge for effective medium theories is to predict the properties of this homogeneous material based on the properties and volume fractions of the phases present in the actual material. Among the many theories that could be used, the one developed by Hill [B23] and by Budiansky [B24] is particularly useful since it provides closed form expressions for the moduli of a two-phase material in the effective medium approximation.

This particular theory was applied by Hsu and Wu to describe the moduli of a two-phase polymer [B25]. They showed how the measured Young's modulus as a function of volume fraction for one of the phases could be accurately represented using the theory of Hill and Budiansky. In particular, they showed how this relatively simple theory captured the essential aspects of percolation that occurred in their polymer system. The results of this theory can be described in a few equations that will be presented here and will be used to develop a description for the moduli of bulk graphite. Following the results presented by Hsu and Wu, there are two equations that relate the bulk modulus (K) and the shear modulus (G) of the effective medium to those of the constituent phases (K_1, K_2 and G_1, G_2) and their respective volume fractions (f_1, f_2). These equations are as follows:

$$f_1(1 - K_1 / K) / (3K_1 + 4G) + f_2(1 - K_2 / K) / (3K_2 + 4G) = 0 \tag{B.1}$$

$$f_1(1 - G_1 / G) / (\alpha G_1 + G) + f_2(1 - G_2 / G) / (\alpha G_2 + G) = 0 \tag{B.2}$$

with

$$\alpha = (8 - 10\nu) / (7 - 5\nu) \tag{B.3}$$

where ν is the Poisson Ratio of the effective medium so that

$$\nu = (3K - 2G) / (6K + 2G). \tag{B.4}$$

It should also be noted that $f_2 = 1 - f_1$. Eliminating the bulk modulus, K, from these equations yields the following result:

$$3f_1K_1 / (3K_1 + 4G) + 3f_2K_2 / (3K_2 + 4G) + 5f_1G_2 / (G - G_2) + 5f_2G_1 / (G - G_1) + 2 = 0. \tag{B.5}$$

As expected, this equation is unchanged if the phase designations are exchanged with one another. Inspection of the form of the equation shows that it is a quartic in G and, as a result, it can be solved

analytically to obtain the shear modulus. Even so, from a practical perspective, it is easier to simply use computational techniques to arrive at the various roots.

For the purposes of this work, we will refer to the polycrystalline graphite as being the first medium and porosity (air) as the second medium. Clearly, the shear modulus for air should be essentially zero while the bulk modulus should be extremely small compared to that of graphite. These assumptions for the behavior of air are likely true even for closed pores since the strains that occur during modulus measurement are small. Letting $G_2 = 0$ in Eq. (B.5) results in the following cubic equation for G [B26]:

$$\alpha G^3 + \beta G^2 + \gamma G + \delta = 0 \tag{B.6}$$

where $\alpha = 32$, $\beta = 24(K_1 + K_2) + 12(f_1 K_1 + f_2 K_2) + 16G_1(5f_2 - 2)$, $\gamma = 27K_1K_2 + 12G_1[(5f_2 - 2)(K_1 + K_2) - (f_1K_1 + f_2K_2)]$ and $\delta = 9K_1K_2G_1(5f_2 - 3)$. There are two volume fractions that simplify this equation further, $f_2 = 0.4$ and 0.6. If the porosity volume fraction is near 0.6 and the compressibility of air is high, then the final term in the cubic may be ignored and the equation can be approximated as a quadratic with the result that the shear modulus of the composite must be zero. Indeed this result essentially holds for porosity in excess of $f_2 \approx 0.5$. An assumption underlying this model is that the properties of the phases making up the effective medium do not change with volume fraction. While this might be true for air, the moduli of the solid phase could vary with porosity and, at this point, some sort of model for the elastic moduli of polycrystalline graphite is needed to assess whether or not this assumption holds. Even though nuclear graphites are composed of a hierarchical microstructure consisting of graphite crystallites (~10^2 nm) joined in graphite grains (20 to 800 μm) within a three-dimensional structure that includes a solid, binder-derived phase along with interspersed voids, macrocracks, etc., the effective medium approach dictates that the specific constitution of this complicated microstructure can be replaced by an equivalent that captures the essential behaviors of the original material. For the purposes of this work, the solid phase (composed of filler particles along with graphitized and amorphous binder) will be represented by an idealized polycrystalline assembly of randomly-oriented, graphite crystallites.

B.3.2. Moduli from the Theory for Polycrystalline Materials

The expected moduli for polycrystalline, fully-dense, bulk graphite should depend directly on the moduli for single crystal graphite as well as the arrangement of the crystallites in the solid. Unfortunately, the relationship between the two is not a simple one. If it is assumed that the polycrystalline aggregate behaves isotropically, then the two independent elastic moduli that describe isotropic materials must map on to the five single crystal moduli. This mapping is directly related to processes in the material that distribute stresses and strains among the crystallites. There are many schemes that have been developed

to model these processes including those by Voigt and Reuss. Under the Voigt averaging scheme, crystallites are loaded under isostrain conditions while the Reuss scheme assumes isostress loading. Neither of these loading configurations is very realistic, but the results of these methods provide upper (Voigt) and lower (Reuss) bounds for the isotropic moduli of the material. Other methods for deriving the isotropic moduli can be used (such as the one developed by Hashin and Shtrikman [B27]), but the simplicity of the Voigt and Reuss methods provides bounds that can be tied directly and easily to micromechanical processes occurring in the polycrystalline solid.

The isotropic, elastic moduli of interest for the experiments performed in this work are C_{11} and C_{44} (using two-index notation) and these are related to the single crystal elastic constants (c_{ij}) as follows for the Voigt averaging scheme:

$$C_{11}^{V} = (8c_{11} + 3c_{33} + 4c_{13} + 8c_{44})/15 \tag{B.7}$$

and

$$C_{44}^{V} = (7c_{11} - 5c_{12} + 2c_{33} - 4c_{13} + 12c_{44})/30 \tag{B.8}$$

where the superscript indicates that these represent the Voigt limit. The corresponding results obtained using the Reuss averaging process are expressed most compactly using the single crystal elastic compliances (s_{ij}). They are as follows:

$$C_{11}^{R} = (S_{11} + S_{12})/[(S_{11} - S_{12})(S_{11} + 2S_{12})] \tag{B.9}$$

and

$$C_{44}^{R} = 1/S_{44} \tag{B.10}$$

where the superscript indicates that these are the Reuss limits for the moduli and

$$S_{11} = (8s_{11} + 3s_{33} + 4s_{13} + 2s_{44})/15 \tag{B.11}$$

$$S_{12} = (s_{11} + 5s_{12} + s_{33} + 8s_{13} - s_{44})/15 \tag{B.12}$$

$$S_{44} = 2(7s_{11} - 5s_{12} + 2s_{33} - 4s_{13} + 3s_{44})/15 \tag{B.13}$$

relate the elastic compliances of the polycrystalline solid to the single crystal values when Reuss averaging is used. For many materials that have relatively low measures of anisotropy for the single crystal moduli, the Voigt and Reuss limits bracket the measured moduli closely. For graphite, the single crystal moduli show a high degree of anisotropy and the Voigt and Reuss limits differ considerably. Indeed, according to Kiewel et al., $C_{11}^{V} - C_{11}^{R} \approx 530$ GPa and $C_{44}^{V} - C_{44}^{R} \approx 200$ GPa [B28] – these differences exceed the actual measured moduli and provide little guidance regarding the expected values.

Hill suggested that a simple arithmetic average of these limits for the shear modulus generally provides values that are close to measured results for many materials systems [B23] and this approach has been extended by others [B29] to estimate other moduli of polycrystalline aggregates. While other theoretical methods have been used to estimate actual moduli from single crystal values, the Hill average provides a relatively good estimate with minimal computational effort. Unfortunately, the Hill values obtained for the moduli of polycrystalline graphite exceed the estimated values for fully dense, isotropic graphite by a considerable amount. Various researchers have attributed this discrepancy to microcracking in the graphite microstructure [B30,B31]. Different types of cracks are known to be present in graphite as a result of the extreme anisotropy of the graphite crystallite and the processing techniques used to produce polycrystalline material – differential thermal expansion/shrinkage that occur during material cooling from graphitization temperatures are accommodated by porosity and microcracking in the microstructure. In particular, Mrozowski cracks readily form between basal planes owing to the relatively weak, interplanar bonding that occurs in these directions in the crystal and these cracks have the effect of altering the single crystal moduli.

B.3.3. Crack-modified Single Crystal Elastic Moduli

The alteration of elastic moduli of solids by the presence of microcracks has been considered by many researchers, but there is no clear consensus on the best way to theoretically represent these changes. Even so, the elastic moduli of hexagonal, single crystal materials containing microcracks perpendicular to the c-axis have been modeled by Schoenberg and Douma [B32] and these can be expressed as follows using two-index notation:

$$c'_{11} = c_{11} - c_{13}^2[1-(1+E_N)^{-1}]/c_{33} \tag{B.14}$$

$$c'_{33} = c_{33}(1+E_N)^{-1} \tag{B.15}$$

$$c'_{44} = c_{44}(1+E_T)^{-1} \tag{B.16}$$

$$c'_{66} = c_{66} \tag{B.17}$$

$$c'_{13} = c_{13}(1+E_N)^{-1} \tag{B.18}$$

$$c'_{12} = c'_{11} - 2c_{66} \tag{B.19}$$

where the c'_{ij} indicate the crack-modified values for the moduli while E_N and E_T are non-dimensional parameters that relate microcrack characteristics to their effects on elastic modulus. Specifically, these parameters can be expressed as $E_N = c_{33}Z_N$ and $E_T = c_{44}Z_T$ where Z_N and Z_T represent the normal and tangential compliances of the microcrack. It should be noted that if the uncracked material is isotropic,

then these expressions generally agree with other results under appropriate conditions [B33]. In this work, it will be assumed that these compliances are approximately equal ($Z_N \approx Z_T$) since this is suggested by Schoenberg and Sayers for various types of materials [B34]. These microcrack-modified, single crystal elastic constants will be used in place of the single crystal values to model the elastic properties of polycrystalline graphite.

B.3.4. Averaging Method – Modified Hill Approach

Using the modified moduli for microcracked, graphite crystallites, Voigt and Reuss limits can be computed for the elastic moduli of polycrystalline graphite and these can be used to obtain Hill averages. Unfortunately, these averages still provide estimates for the elastic moduli that are too high if acceptable values for the microcrack compliances are assumed and this indicates that some kind of modification of the Hill averaging technique should be used for polycrystalline graphite microstructures. Instead of assuming a simple arithmetic average, a weighted averaging scheme will be used where the average, polycrystalline moduli, $\overline{C}_{ij}$, can be expressed as follows:

$$\overline{C}_{ij} = rC_{ij}^{R} + (1-r)C_{ij}^{V} \tag{B.20}$$

where $0 \le r \le 1$. The weighting parameter, r, provides some measure of the fraction of the microstructure that transfers stresses and strains according to the Reuss averaging scheme and essentially represents some type of preferred connectivity of the overall microstructure when $r \ne 0.5$. If $r < 0.5$, then the higher material stiffnesses will figure more prominently into the average while $r > 0.5$ would indicate that the higher compliances would be more important in determining the overall stiffness of the material. For single crystal graphite as well as microcracked-modified single crystals, higher stiffnesses occur in the basal plane while higher compliances occur for directions perpendicular to this plane. Consequently, adjacent crystallites that are aligned in such a way to transfer loads along the basal plane will cause the material to be relatively stiff and yield $r < 0.5$ while those that are not aligned in this way will cause the material to be more compliant yielding $r > 0.5$. In some ways, the concept behind this modeling approach is similar to the one used by Bradford and Steer to interpret changes in properties of nuclear graphites that have undergone neutron irradiation. However, unlike the development outlined here, the models they present are focused on macroscopic descriptions and are not based on micromechanical processes in graphite [B35].

B.3.5. Porosity and Selective Oxidation

Using results described in the previous sections, an overall model describing the moduli of porous, isotropic, polycrystalline graphite can be constructed and can be used to assess the variation of modulus that should occur in nuclear graphites when porosity changes. Measured porosities for contemporary

nuclear graphites as well as those for legacy materials generally fall in the range $0.16 < \varphi < 0.27$ (where in terms of previous notation $\varphi = f_2$) and the overall model developed here can be used to describe the variation of the measured moduli of these materials as function of porosity. However, when porosity in a particular graphite grade is intentionally changed by reacting graphite with oxygen at elevated temperatures, measured moduli decrease far more rapidly with porosity than would be indicated by the model. This discrepancy is likely related to selective oxidation of the graphite microstructure.

In the model describing modulus versus porosity, an implicit assumption is that the constituent phases and their properties are not affected by the volume fractions of the phases themselves. This assumption implies that the moduli of the polycrystalline graphite phase in nuclear graphites do not vary as porosity is changed. This might be true for as-manufactured graphites that are produced using similar processing techniques. However, gas phase oxidation of graphite is known to occur more readily at the edges of basal planes such that increases in porosity occur as a result of selective oxidation of crystallites along these edges [B36-38]. While oxidation does occur at the basal plane surfaces, the rate is relatively low compared to other sites on the crystallite surface. The implication is that connections between crystallites involving basal plane edges are altered more rapidly than those associated with plane surfaces with the result that the microstructure and the associated micromechanics of the polycrystalline phase vary as porosity increases.

To incorporate this effect into the model for the elastic moduli, the impact of the oxidation process on the connectivity of graphite crystallites needs to be considered. Material removal from basal plane edges essentially reduces the ability of the material to transfer loads in a manner that is assumed for the Voigt limit. To reflect this, a porosity-dependent value for the averaging parameter, r, will be used. In the absence of a formal description of this relationship, the ansatz $r = r_0 + b\varphi$ will be used to interpret experimental data where r_0 is the value of the averaging parameter for unoxidized material and b represents the sensitivity of the parameter to porosity. If the condition $r_0 + b\varphi > 1$ holds, then it will be assumed that $r = 1$ indicating that the microstructural elements contributing to the Voigt limit have been eliminated by oxidation. All the remaining microstructure behaves according to the Reuss description and any changes in porosity will simply remove material without significant changes to the microscopic elastic behavior of the graphite that remains – the elastic response of the graphite phase (as it is measured using ultrasonic methods) becomes independent of porosity.

B.4. Experimental and Modeling Results

B.4.1. Ultrasonic Measurements

Longitudinal and shear moduli can be determined from values of sample density and ultrasonic velocity

using the following relations:

$$\bar{C}_{11} = \rho v_L^2 \qquad \text{and} \qquad \bar{C}_{44} = \rho v_S^2 \tag{B.21}$$

where $\bar{C}_{11} = K + 4G/3$ is longitudinal modulus, $\bar{C}_{44} = G$ is the shear modulus, ρ is the mass density, v_L is the longitudinal wavespeed and v_S is the shear wavespeed. To compute wavespeeds, transit times for the longitudinal and shear waves are needed and these can be taken from the laser ultrasonic waveforms (an example for oxidized IG-110 is shown in Fig. B.3). Even though details regarding the

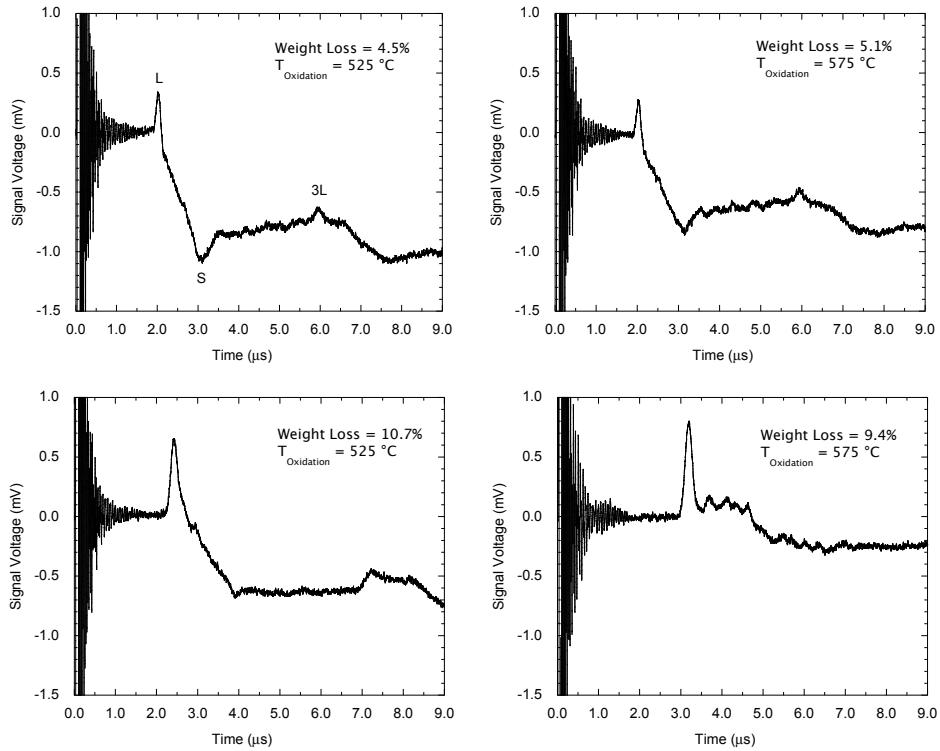

Figure B.3. Laser ultrasonic waveforms obtained in different samples of IG-110 oxidized at either 525 °C or 575 °C. The weight losses obtained for each sample are shown. In the upper left graph, the arrival of longitudinal wave (L) occurs at 2.05 us and arrival of shear wave (S) occurs at 3.1 us. The reflected longitudinal wave (3L) is also indicated. Noise from the pulsed excitation laser dominates the signal from 0.0 to 1.5 us in all waveforms.

interpretation of waveforms in graphite materials are the subject of current studies, in many cases the times associated with specific features can be taken to be the transit times for the longitudinal and shear waves respectively (see Fig. B.3). A more accurate measurement using a pulse-echo overlap method could be used, but signal-to-noise issues for waveforms taken in heavily oxidized materials prevent its use.

In Fig. B.3, representative waveforms obtained in different samples are shown for IG-110 and these generally illustrate the variations in signatures for wavefront arrivals that occur in nuclear graphites.

Owing to the complicated nature of laser ultrasonic waveforms, especially those for more highly oxidized samples, it is sometimes difficult to precisely identify wave arrivals and determine associated transit times. To reduce measurement variability associated with this uncertainty, high-order polynomial functions were fit to the data in regions associated with the wave arrivals and transit times were based on these fits. Combining these times with sample thickness measurements along with separate measurements of sample density, values for the longitudinal and shear moduli could be computed and are summarized in Table B.2.

Table B.2. Oxidized Graphite Density, Porosity and Moduli

Graphite Sample Designation	Oxidation Temperature (°C)	Oxidative Weight Loss	Sample Thickness (cm)	Mass Density (g/cm^3)	Porosity	$\overline{C}_{11}$ (GPa)	$\overline{C}_{44}$ (GPa)
IG-110							
As-received	-	0.00	0.604	1.77	0.217	10.0	4.07
HT1	575	9.41	0.556	1.653	0.269	5.12	1.95
HT2	525	10.7	0.380	1.623	0.282	3.80	1.51
HT3	525	4.51	0.425	1.726	0.236	7.43	3.17
HT4	575	5.12	0.444	1.732	0.234	8.56	3.58
NBG-18							
As-received	-	0.00	0.615	1.88	0.168	14.1	5.67
HT1	575	10.92	0.595	1.757	0.223	8.00	2.56
HT2	500	9.99	0.618	1.784	0.211	10.0	3.90
HT3	500	4.30	0.560	1.843	0.185	12.8	4.98
HT4	575	4.30	0.584	1.840	0.186	12.0	4.53

B.4.2. Modulus and Porosity

The relationship of the measured moduli to porosity can be examined by graphing the results given in Table B.2, but for purposes of comparison, the longitudinal and shear moduli will be used to derive Young's modulus, E, for all the graphite samples using the following relationship:

$$E = \overline{C}_{44}(3\overline{C}_{11} - 4\overline{C}_{44}) / (\overline{C}_{11} - \overline{C}_{44}). \tag{B.22}$$

The results are shown in Fig. B.4 where Young's modulus and the shear modulus for all samples (IG-110 and NBG-18) are shown as a function of porosity. The solid lines represent fits to the data using the microcrack-modified, single-crystal elastic moduli (all in GPa) $c'_{11} = 1053.79$, $c'_{33} = 1.07$, $c'_{44} = 0.857$, $c'_{12} = 173.79$, $c'_{13} = 0.447$ (using the single crystal elastic moduli $c_{11} = 1060$, $c_{33} = 36.5$, $c_{44} = 4.00$,

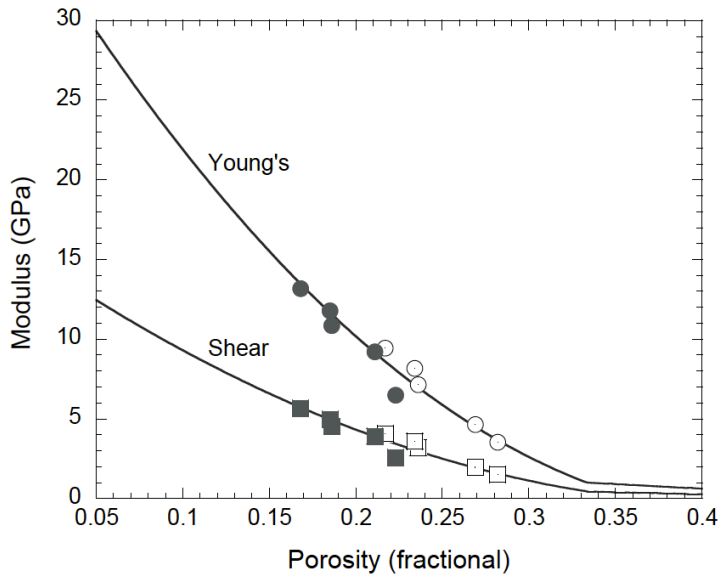

Figure B.4. Elastic moduli – Young's and shear – for nuclear graphites IG-110 (open symbols) and NBG-18 (filled symbols) as a function of porosity. Variations in porosity for a given grade were produced by oxidation. Solid curves are fits to the data based on the model outlined in this work.

$c_{12} = 180$, $c_{13} = 15.0$ with $Z_N = Z_T = 0.5$) and the averaging parameter $r = 1 - 0.068(1 - 3\varphi) = 0.932 + 0.204\varphi$. It should be noted that the computed results for both moduli depend on the same values for:

1. the microcrack-modified, single-crystal, elastic moduli,
2. the initial contribution of Reuss and Voigt limits to the polycrystalline moduli,
3. the relative contributions of these limits as a function of oxidation-induced, porosity evolution.

Essentially, the model only requires specification of three parameters once the single crystal elastic moduli are provided ($Z_N = Z_T$, r_0 and b) and with these the fits for both sets of modulus measurements are obtained. No distinction between the results for IG-110 and NBG-18 were made in establishing the modeled fits since the data appeared to follow a single trend. This approach is perhaps supported by the nature of oxidation in these materials since the majority of material loss occurs as a result of micro/nanoscale processes throughout the graphite microstructure and the two graphite grades might not differ significantly at this level. Even with this coarse approach to data interpretation, the correlation coefficient for the fit to Young's modulus data is $R = 0.9716$ and for the shear modulus it is 0.9551. The discontinuity in the first derivative of the modeled results at $\varphi = 1/3$ is related to exhaustion of Voigt-related contributions to the modulus. At higher porosities, the microstructure behaves according to the

Reuss model and the moduli have a linear variation with porosity. Both moduli essentially go to zero when $\varphi = 0.5$.

B.5. Discussion

This work raises numerous points for discussion, but only a few will be briefly mentioned here. First, the physics-based modeling outlined here provides direct connections between the established literature for the elastic properties of multiphase, polycrystalline materials and the related ultrasonic behavior of nuclear graphites. In particular, modeling has shown that the behavior of porous graphite materials depend heavily on the methods that are used to introduce porosity (or changes in porosity) into the overall microstructure. Standard models for the moduli of isotropic, two-phase materials typically assume that volume fraction does not affect phase modulus. However, this is likely not the case for oxidation-induced, porosity changes in polycrystalline graphite since preferential oxidation of specific microstructural elements primarily in the binder will result in related modulus changes. These changes will likely differ from those associated with other processes that could be used to change porosity. In this work, methods to account for the selective effects of oxidation processes on graphite modulus have been proposed and successfully used to interpret measurements.

Next, the measurements presented here were obtained using laser ultrasonic methods and it would be useful to understand how these ultrasonic results compare with those in the existing literature that were obtained using other methods [B39]. Since only optical access to the sample is required to perform laser ultrasonic measurements, materials with highly compliant microstructures can be characterized without changing the essential behavior of the material. Other ultrasonic techniques using contacting transducers can load the material and produce changes that affect the modulus. For oxidation processes in graphite, small changes in the microstructure can produce relatively large changes in modulus owing to the extreme anisotropy of graphite crystallites. For example, if two adjacent crystallites transfer stress in the basal plane, then oxidation at the boundary between the two can dramatically reduce the local modulus. However, if the material is loaded in a manner that brings the boundaries of these crystallites into contact, then the modulus will increase. Methods to measure the elastic modulus of oxidized graphites will only yield comparable results if the loading conditions used during the measurement process are the same. Unfortunately, most results in the literature have been obtained using contacting transducers or other techniques that load the sample. However, Eto et al. [B11] performed ultrasonic measurements on samples of oxidized IG-11 that were bonded to a buffer rod. Ultrasonic measurements were performed through the rod in a pulse-echo configuration in a manner that left the sample in a nearly unloaded condition. Their measurements of Young's modulus (corrected) are shown in Fig. B.5 along with the

results from Fig. B.4 (no longer differentiated by grade) – the agreement of these experimental results is quite good despite the differing graphite grades and measurement methods.

Moreover, a comparison can be made between the model used by Eto et al. to fit their data and the model developed in this work. Eto et al. used a power law function to fit their Young's modulus data and this variation can be partially justified on a theoretical basis. Researchers interested in the percolation of elastic networks have shown that the bulk and shear moduli should display power law dependence near the percolation threshold [B40,B41]. However, this dependence simply represents a functional fit to numerically-generated values for modulus derived from simulations of network solids. This means that the basis for the power law is one step removed from the assumed physical constitution of the network. Regardless, the model developed in this work can be fit to the data presented by Eto et al. and a comparison can be made to a power law fit. Figure B.6 shows the related graphs. The results show that the overall behaviors of the functional fits to the data are similar and that in the range of the data the correlation coefficients are nearly identical – 0.9978 for the power law and 0.9958 for the physical model developed in this work. Additional observations could be made regarding experimental measurements and the behaviors of the various models, but these would necessarily be limited by the quality of available results and by the current understanding of the effects of oxidation processes on nuclear graphite microstructure.

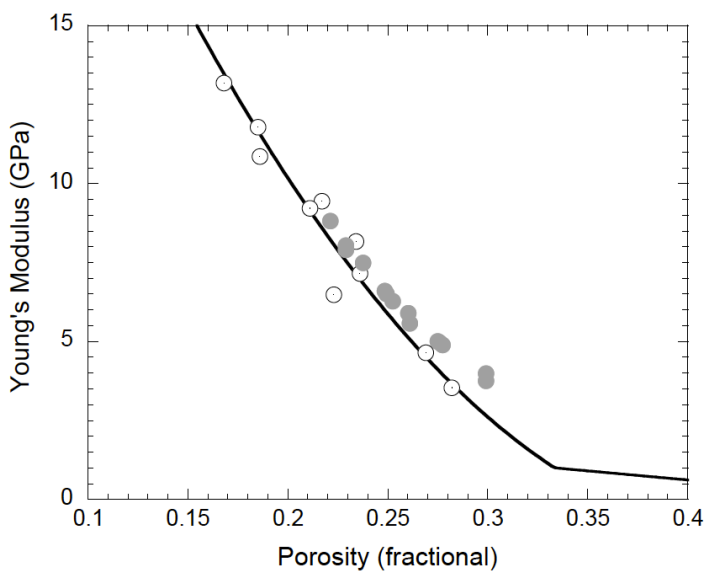

Figure B.5. Young's modulus measurements in oxidized IG-11 (from Eto et al. – filled circles), IG-110 and NBG-18 (open circles). The solid curve is the model fit from Fig. B.4.

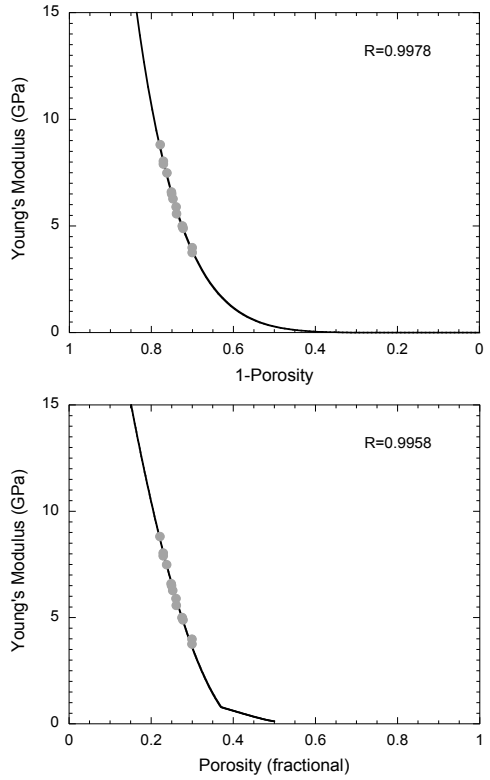

Figure B.6. Young's modulus as a function of porosity in IG-11. Data values (filled circles) represent data published by Eto et al. [B11]. Solid curves represent functional fits to the data – power law (top) and the physical model presented in this work (bottom).

B.6. Conclusion

In this work, the elastic moduli of oxidized nuclear graphites have been studied using a combination of physics-based models along with experimental measurements using ultrasonic methods. Assuming that nuclear graphites behave as porous, polycrystalline solids, an effective medium model for the elastic response of these materials was developed that included the effects of microcracks on the elastic behavior of graphite crystallites. Owing to the physical basis for this model, the effects of oxidation could be taken into account. Beyond simply increasing porosity, oxidation preferentially changes specific portions of the microstructure and these changes could be incorporated into the model to successfully interpret experimental determinations of elastic modulus. Laser ultrasonic methods were used to measure the longitudinal and shear moduli as a function of porosity. These methods only require optical access and do not impose any significant mechanical loading on the material surface so that highly compliant structures that develop as a result of oxidation are not altered during the ultrasonic measurement process. The effect of this loading can be quite important for oxidized graphite and can influence modulus measurements – especially in more porous materials. The effect of the measurement on the state of the

material has significant implications for developing sensing strategies for structural health monitoring and needs to be considered when assessing measurement results.

References

[B1] Morgan WC, Davis TJ, Thomas MT. Feasibility of monitoring the strength of HTGR core support graphite – Part III. U.S. NRC Report NUREG/CR-2929, PNL-4449, R8.

[B2] Bodel W. *The relationship between microstructure and Young's modulus of nuclear graphite*. Ph.D. dissertation, The University of Manchester, 2012.

[B3] EL GUERJOUMA R, MOUCHTACHI A, JAYET Y, BABOUX JC. Nondestructive evaluation of graphite by ultrasonic velocity-measurement using cross-correlation and Hilbert transform methods. *IEEE 1992 Ultrasonics Symposium : Proceedings, Vols 1 and 2*. 1992:829-832.

[B4] ETO M, GROWCOCK FB. Effect of oxidizing environment on the strength of H451, PGX and IG-11 graphites. *Carbon*. 1983;21(2):135-147.

[B5] Shibata T, Ishihara C. Ultrasonic signal characteristics by pulse-echo technique and mechanical strength of graphite materials with porous structure. *Nucl Eng Des*. 2001;203(2-3):133-141.

[B6] COST JR, JANOWSKI KR, ROSSI RC. Elastic properties of isotropic graphite. *Philosophical Magazine*. 1968;17(148):&.

[B7] THROWER PA, MATHEW GK, MCGINNIS NJ. The influence of oxidation on the structure and strength of graphite .2. materials of different impurity content. *Carbon*. 1982;20(6):465-471.

[B8] SATO S, HIRAKAWA K, KURUMADA A, KIMURA S, YASUDA E. Degradation of fracture-mechanics properties of reactor graphite due to burn-off. *Nucl Eng Des*. 1990;118(2):227-241.

[B9] YODA S, ETO M, TANAKA K, OKU T. Effects of oxidation on compressive deformation-behavior of nuclear-grade isotropic graphite. *Carbon*. 1985; 23(1):33-38.

[B10] ISHIYAMA S, OKU T, ETO M. Effect of oxidation on crack extension rate of fine-grained isotropic graphite. *Journal of the Atomic Energy Society of Japan*. 1986;28(10):971 ER.

[B11] ETO M, OKU T, KONISHI T. High-temperature Young modulus of a fine-grained nuclear graphite oxidized or prestressed to various levels. *Carbon*. 1991;29(1):11-21.

[B12] Shibata T, Sumita J, Tada T, Hanawa S, Sawa K, Iyoku T. Non-destructive evaluation methods for degradation of IG-110 and IG-430 graphite. *J Nucl Mater*. 2008;381(1-2):165-170.

[B13] Shibata T, Tada T, Sumita J, Sawa K. Oxidation damage evaluation by non-destructive method for graphite components in high temperature gas-cooled reactor. *J of Solid Mechanics and Materials Engineering*. 2008; 2(1): 166-175.

[B14] Wen KY, Marrow TJ, Marsden BJ. The microstructure of nuclear graphite binders. *Carbon*. 2008;46(1):62-71.

[B15] Kane J, Karthik C, Butt DP, Windes WE, Ubic R. Microstructural characterization and pore structure analysis of nuclear graphite. *J Nucl Mater*. 2011;415(2):189-197.

[B16] Karthik C, Kane J, Butt DP, Windes WE, Ubic R. Microstructural characterization of next generation nuclear graphites. *Microscopy and Microanalysis*. 2012;18(2):272-278.

[B17] Contescu CI, Azad S, Miller D, Lance MJ, Baker FS, Burchell TD. Practical aspects for characterizing air oxidation of graphite. *J Nucl Mater*. 2008;381(1-2):15-24.

[B18] Chi S, Kim G. Comparison of the oxidation rate and degree of graphitization of selected IG and NBG nuclear graphite grades. *J Nucl Mater*. 2008;381(1-2):9-14.

[B19] ASTM D7542-15 Standard Test Method for Air Oxidation of Carbon and Graphite in the Kinetic Regime, ASTM International, West Conshohocken, PA, 2015, https://doi.org/10.1520/D7542-15.

[B20] Wang P, Contescu CI, Yu S, Burchell TD. Pore structure development in oxidized IG-110 nuclear graphite. *J Nucl Mater*. 2012;430(1-3):229-238.

[B21] Kane, J. J., Contescu, C. I., Smith, R. E., Strydom, G., & Windes, W. E. Understanding the reaction of nuclear graphite with molecular oxygen: Kinetics, transport, and structural evolution. *J Nucl Mater.* 2017; *493*, 343-367. doi:10.1016/j.jnucmat.2017.06.001

[B22] Spicer, J. B., Zeng, F. W., Han, K., Olasov, L. R., Gallego, N. C., & Contescu, C. I. Effects of graphite porosity and anisotropy on measurements of elastic modulus using laser ultrasonics. *2014 IEEE International Ultrasonics Symposium (IUS)*. 2014; 232-235. doi:10.1109/ULTSYM.2014.0059

[B23] HILL R. A self-consistent mechanics of composite materials. *J Mech Phys Solids*. 1965;13(4):&.

[B24] BUDIANSKY B. On elastic moduli of some heterogeneous materials. *J Mech Phys Solids*. 1965;13(4):&.

[B25] HSU WY, WU SH. Percolation behavior in morphology and modulus of polymer blends. *Polym Eng Sci*. 1993;33(5):293-302.

[B26] HSU WY, GIRI MR, IKEDA RM. Percolation transition and elastic properties of block copolymers. *Macromolecules*. 1982;15(4):1210-1212.

[B27] HASHIN Z, SHTRIKMAN S. Note on a variational approach to the theory of composite elastic materials. *Journal of the Franklin Institute-Engineering and Applied Mathematics*. 1961;271(4):&.

[B28] Kiewel H, Bunge HJ, Fritsche L. Effect of the grain shape on the elastic constants of polycrystalline materials. *Textures and Microstructures* 1996; 28:17-33

[B29] LI Y, THOMPSON RB. Relations between elastic-constants cij and texture parameters for hexagonal materials. *J Appl Phys*. 1990;67(5):2663-2665.

[B30] Hassleman DPH. Voigt and Reuss moduli of polycrystalline solids with microcracks. *J of the American Ceramic Society*. 1970; 53(3):170.

[B31] Spicer JB, Olasov LR, Zeng FW, Han K, Gallego NC, Contescu CI. Laser ultrasonic assessment of the effects of porosity and microcracking on the elastic moduli of nuclear graphites. *J Nucl Mater*. 2016;471:80-91.

[B32] SCHOENBERG M, DOUMA J. Elastic wave-propagation in media with parallel fractures and aligned cracks. *Geophys Prospect*. 1988;36(6):571-590.

[B33] Zheng ZQ. Seismic anisotropy due to stress-induced cracks. *Int J Rock Mech Min Sci*. 2000;37(1-2):39-49.

[B34] SCHOENBERG M, SAYERS CM. Seismic anisotropy of fractured rock. *Geophysics*. 1995;60(1):204-211.

[B35] Bradford MR, Steer AG. A structurally-based model of irradiated graphite properties. *J Nucl Mater*. 2008;381(1-2):137-144.

[B36] TUINSTRA F, KOENIG JL. Characterization of graphite fiber surfaces with Raman spectroscopy. *J Composite Mater*. 1970;4:& ER.

[B37] CHU X, SCHMIDT LD. Reactions of NO, O2, H2O, and CO2 with the basal-plane of graphite. *Surf Sci*. 1992;268(1-3):325-332.

[B38] Hahn JR. Kinetic study of graphite oxidation along two lattice directions. *Carbon*. 2005;43(7):1506-1511.

[B39] Vasudevamurthy, G., Byun, T. S., Pappano, P., Snead, L. L., & Burchell, T. D. Effect of specimen size and grain orientation on the mechanical and physical properties of NBG-18 nuclear graphite. *J Nucl Mater,* 2015; *462*, 1-7. doi:10.1016/j.jnucmat.2015.02.012

[B40] FENG S, SEN PN. Percolation on elastic networks - new exponent and threshold. *Phys Rev Lett*. 1984;52(3):216-219.

[B41] Nachtrab S, Kapfer SC, Arns CH, Madadi M, Mecke K, Schroeder-Turk GE. Morphology and linear-elastic moduli of random network solids. *Adv Mater*. 2011;23(22-23):+.

2. Shear Birefringence Measurements for Determination of Microcrack Density and Orientation Distribution

Section C: Line Source Representations for Shear Wave Birefringence Measurements in Transversely Isotropic Materials using Laser Ultrasonics

C.1. Introduction

Elastic waves derived from line sources have received the attention of researchers dating back to Lamb whose classic work on step loading of an elastic half-space has inspired innumerable, succeeding investigations including the results presented here [C1-3]. In this work, we develop models for ultrasonic waves produced using laser line sources in transversely anisotropic materials with the aim of developing specific shear wave polarizations that can be used to make birefringence measurements and characterize aspects of the material anisotropy. These models will use idealized line source representations for the laser source to simplify the overall treatment and to highlight the effects of elastic anisotropy on wave propagation. Taking this approach allows for a concise presentation of analytical solutions and isolates specific characteristics of these solutions. It also captures the essential physical processes permitting easy computation for comparison to experimental measurements. These comparisons are not presented in this work, but various characteristics of wave propagation that have not been explored previously will be noted – these potentially point to new directions for materials characterization using elastic waves.

An important characteristic of materials that directly impacts elastic wave propagation is texture – the partial alignment of elastically anisotropic grains/crystallites. For a population of randomly-oriented grains that interact with ultrasound over sufficient propagation distances, materials can behave isotropically. However, if the grains do not have complete orientational randomization in the sampled volume, then the material will be elastically anisotropic and wavespeeds will vary with direction and polarization [C4-6]. Beyond grain orientation effects, partial alignment of defect structures such as microcracks can also induce elastic anisotropy [C7-10]. Ultrasound has been used to assess this anisotropy and, with appropriate models, can be used to infer some characteristics of the underlying microstructure such as the orientation distribution coefficients. In particular, shear wave birefringence measurements can be used to isolate specific aspects of the anisotropy that can be useful for process monitoring and control [C11-13] and various methods have been implemented to make these types of measurements [C14,C15], but none has taken advantage of laser line sources to produce polarized shear waves.

Laser line sources for elastic wave generation as well as the wavefields associated with these sources have been studied extensively. Early work simulated the behavior of thermoelastic sources using shear stress dipoles and focused on the directivity patterns associated with longitudinal and shear waves in isotropic materials [C16]. Subsequent reports refined this general description by including details related to the

underlying physics such as optical absorption, photothermal conversion and thermoelastic response [C17-22]. Various approaches have been used to model characteristics of the resulting elastic wavefield and these have been verified experimentally [C17]. One major finding is that the wave directivities and polarizations for these types of sources are complicated – even when the material is isotropic. Unlike other methods that have been used to perform ultrasonic shear birefringence measurements, the potential for using laser line sources for these types of measurements is largely unexplored. A good starting point for assessing this potential is to model shear wave birefringence in anisotropic materials excited using a laser source.

For isotropic materials, modeling of elastic waves generated by line sources has been the subject of many investigations. Indeed, Lamb's original problem is generally shown in textbooks on wave motion in elastic solids since it considers isotropic materials – the expressions for displacements in the wavefield are compact and readily interpreted [C1,C3,C23]. The extension to anisotropic materials and point sources requires effort but yields rich results that go well beyond those to be exploited here [C24-31]. Fortunately, line source excitation of transversely anisotropic half-spaces has also been considered in some detail and the essential mathematical techniques required to derive solutions is generally no more involved than those used for isotropic materials [C32-34]. However, compact analytical solutions exist only for specific cases, but these can be obtained using careful algebraic manipulations. While direct numerical solution of the governing equations and boundary conditions can be performed [C35,C36], simple insights into the overall behavior of the system can be lost – analytical results permit general conclusions to be made that might be difficult to identify otherwise. The subsequent sections will develop models for the epicentral displacements resulting from laser line excitation of transversely isotropic half-spaces of different orientations. The development will largely follow approaches presented previously by Payton [C37], Hurley [C38] and others [C39] with minor changes to notation to improve clarity. Three specific cases will be considered: Case I – Line source in the plane of symmetry, displacements along the symmetry axis; Case II – Line source perpendicular to the symmetry axis, displacements perpendicular to the symmetry axis; Case III – Line source parallel to the symmetry axis, displacements perpendicular to the symmetry axis. The geometry for each is shown in Fig. C.1. While only Cases II and III are needed to illustrate shear wave birefringence, Case I shows the methods used for solution and complements the other results. In all cases, final solutions for epicentral displacements will be given for materials having convex normal surfaces (Class I materials) such as occurs for various single crystals with hexagonal symmetry [C37] as well as for certain weakly-textured, polycrystalline materials displaying transverse isotropy.

C.2. Theory and Models

In the following developments, epicentral displacements from suitably-oriented, unit strength, shear stress dipoles will be derived. These stresses relate directly to the corresponding surface tractions that are appropriate for each case. The relationship of shear stress dipoles to laser line sources has been established previously and these are relatively simple for adiabatic conditions that ignore thermal diffusion [C19,C38,C39]. Under these conditions, appropriate normalization factors can be applied to the results presented here to compute displacements.

C.2.1 Epicentral Displacements Along Symmetry Axis – Case I

Suppose we have a transversely isotropic material in the form of a half-space where the surface is perpendicular to the x_3-axis. A shear stress is applied at the surface along the x_1-axis such that:

$$\sigma_{32}\big|_{x_3=0} = \delta'(x_2)H(t) \tag{C.1}$$

where σ_{ij} is the elastic stress tensor, $\delta(x_i)$ is the Dirac delta (the prime indicates differentiation with respect to x_2) and $H(t)$ is the Heaviside step function where t represents time. No normal tractions act at the boundary and this implies that the normal stress vanishes:

$$\sigma_{33}\big|_{x_3=0} = 0\ . \tag{C.2}$$

These conditions mimic those for a laser line source in the thermoelastic (non-ablative) regime. The equation of motion for the medium can be written as:

$$\sigma_{ji,j} + f_i = \rho u_{i,tt} \tag{C.3}$$

where f_i represents the component of the body force along the x_i axis, ρ is the material density and u_i is the material displacement along the x_i axis and indices after commas indicate differentiation – spatial coordinates are referenced using corresponding subscripts. The following constitutive relationship will be used:

$$\sigma_{ij} = c_{ijkl}\varepsilon_{kl} \tag{C.4}$$

where c_{ijkl} are the components of the elastic stiffness tensor and ε_{kl} is the infinitesimal strain tensor. This can be written in terms of the material displacement as follows:

$$\varepsilon_{ij} = (u_{i,j} + u_{j,i})/2\ . \tag{C.5}$$

Using these relationships along with the equation of motion yields the following wave equation describing material displacements in the medium:

$$c_{ijkl}u_{k,lj} + f_i = \rho u_{i,tt} \tag{C.6}$$

where the symmetry of the stress tensor has been utilized. For transversely isotropic materials, the stiffness tensor exhibits a number of symmetries that can be used to reduce the number of independent, non-vanishing components to the following: $c_{11} = c_{22} \neq c_{33}$, $c_{12} \neq c_{13} = c_{23}$, $c_{44} = c_{55}$ and $c_{66} = (c_{11} - c_{12})/2$ where contracted notation has been used for the subscripting ($11 \rightarrow 1$, $22 \rightarrow 2$, $33 \rightarrow 3$, $23 \rightarrow 4$, $13 \rightarrow 5$ and $12 \rightarrow 6$). Making the substitutions [C37]:

$$u_i = (\rho / c_{44})^{1/2} v_i \qquad \text{and} \qquad t = (\rho / c_{44})^{1/2} \tau \tag{C.7}$$

in Eq. (C.6) yields the following:

$$(c_{ijkl} / c_{44}) v_{k,lj} + f_i (\rho c_{44})^{-1/2} = v_{i,\tau\tau} \tag{C.8}$$

where the stiffness tensor components have been normalized by one of the shear stiffnesses and the body force is normalized by the corresponding elastic impedance. For the purposes of this presentation, it will be assumed that the laser source can be represented using boundary stresses alone and subsurface sources are negligible ($f_i = 0$). Considerations of the symmetry of the imposed boundary stresses indicate that $v_1 = 0$ and $v_{i,1} = 0$ – only displacements and derivatives associated with the x_2 and x_3 need to be considered. Using $\alpha = c_{33} / c_{44}$, $\beta = c_{11} / c_{44}$ and $\kappa = 1 + c_{23} / c_{44}$, Eq. (C.8) yields the following:

$$\beta v_{2,22} + v_{2,33} + \kappa v_{3,23} = v_{2,\tau\tau} \tag{C.9}$$

and

$$\alpha v_{3,33} + v_{3,22} + \kappa v_{2,32} = v_{3,\tau\tau} \,. \tag{C.10}$$

These equations need to be solved simultaneously and this will be accomplished using the Fourier-Laplace transform pair defined as follows:

$$\overline{v}_i = \int_0^{\infty} \int_{-\infty}^{\infty} v_i \exp(-ik_2 x_2 - s\tau) dx_2 d\tau \tag{C.11}$$

and

$$v_i = -i(2\pi)^{-2} \int_C \int_{-\infty}^{\infty} \overline{v}_i \exp(ik_2 x_2 + s\tau) dx_2 ds \,. \tag{C.12}$$

Transforming Eqs. (C.9) and (C.10) and assuming $\overline{v}_2 = A \exp(k_3 x_3)$ along with $\overline{v}_3 = B \exp(k_3 x_3)$ yields two algebraic equations that must be solved simultaneously. The following characteristic equation results:

$$\alpha k_3^{\,4} - k_3^{\,2}((1+\alpha)s^2 + \chi k_2^{\,2}) + (\beta k_2^{\,4} + (1+\beta) k_2^{\,2} s^2 + s^4) = 0 \tag{C.13}$$

where $\chi = 1 + \alpha\beta - \kappa^2$. The form for this equation suggests that we can parameterize the propagation constants as follows: $k_2 = s\gamma_2$ and $k_3 = s\gamma_3$ [C37]. The resulting equation is a quadratic for $\gamma_3{}^2$ (bi-quadratic for γ_3) and the resulting four roots are summarized as follows:

$$\gamma_{3_1} = (2\alpha)^{-1/2}\{[(1+\alpha) + \chi\gamma_2{}^2] + \varphi^{1/2}\}^{1/2} \tag{C.14a}$$

$$\gamma_{3_2} = -\gamma_{3_1} \tag{C.14b}$$

$$\gamma_{3_3} = (2\alpha)^{-1/2}\{[(1+\alpha) + \chi\gamma_2{}^2] - \varphi^{1/2}\}^{1/2} \tag{C.14c}$$

$$\gamma_{3_4} = -\gamma_{3_3} \tag{C.14d}$$

where $\varphi = [(1+\alpha) + \chi\gamma_2{}^2]^2 - 4\alpha[\beta\gamma_2{}^4 + (1+\beta)\gamma_2{}^2 + 1]$. Propagating solutions require that these roots be real and consideration of solution boundedness as $x_3 \to \infty$ requires that only explicitly negative roots be retained in the full solution. The assumed forms for $\overline{v}_2$ and $\overline{v}_3$ are as follows:

$$\overline{v}_2 = a_1 \exp(-s\gamma_{3_1} x_3) + a_2 \exp(-s\gamma_{3_3} x_3) \tag{C.15}$$

$$\overline{v}_3 = b_1 \exp(-s\gamma_{3_1} x_3) + b_2 \exp(-s\gamma_{3_3} x_3)\,. \tag{C.16}$$

The four coefficients are determined using the transformed versions of Eqs. (C.8), (C.9), (C.2) and (C.1). In this work, we are only interested in displacements along the x_3 axis (since these can be readily measured) and will only present results for the coefficients b_1 and b_2. Clearly, direct computation of displacements can be carried out at this point, but there are advantages that can be gained by additional analytical manipulations of the various equations since relatively simple expressions for the displacements can be obtained ultimately. The extensive algebra involved is unwieldy and requires keen attention to groupings of terms, but in the end the following results are obtained:

$$b_1 = (c_{44}\rho)^{-1/2}(\kappa\gamma_2{}^2 / s)[(1+\gamma_2{}^2)(1-\kappa) - \alpha\gamma_{3_3}{}^2]\gamma_{3_1} \div D \tag{C.17}$$

and

$$b_2 = -(c_{44}\rho)^{-1/2}(\kappa\gamma_2{}^2 / s)[(1+\gamma_2{}^2)(1-\kappa) - \alpha\gamma_{3_1}{}^2]\gamma_{3_3} \div D \tag{C.18}$$

where

$$D = \kappa(\gamma_{3_1} - \gamma_{3_3})\{(1+\gamma_2{}^2)[2(1-\kappa)\gamma_2{}^2 - (\chi\gamma_2{}^2 + \alpha)] - \alpha\gamma_{3_1}\gamma_{3_3}\}\,. \tag{C.19}$$

Equations (C.16)-(C.19) provide the complete solution for the desired displacements in the doubly transformed domain. Fortunately, the process for performing the required inversions is well known. Even so, the various steps will be shown here for completeness.

First, the inverse Fourier transform with respect to the variable $k_2 = s\gamma_2$ will be performed:

$$\tilde{v}_3 = (2\pi)^{-1}\int_{-\infty}^{\infty}\bar{v}_3 \exp(is\gamma_2 x_2)sd\gamma_2 = (\pi)^{-1}\,\mathrm{Re}\int_0^{\infty}\bar{v}_3 \exp(is\gamma_2 x_2)sd\gamma_2 \tag{C.20}$$

where $\tilde{v}_3$ represents the Laplace transform of v_3 and the final equality in Eq. (20) results from $\bar{v}_3$ being even in γ_2.

Since only epicentral displacements are needed, $x_2 = 0$ and the transform simplifies considerably since the integrand in Eq. (C.20) depends on ${\gamma_2}^2$ – this suggests a change in the integration variable. Letting $\Gamma_2 = {\gamma_2}^2$ yields the following:

$$\tilde{v}_3 = (2\pi)^{-1}\,\mathrm{Re}\int_0^{\infty}\bar{v}_3 s{\Gamma_2}^{-1/2}d\Gamma_2\ . \tag{C.21}$$

While this change might not appear to have achieved any significant advantage, it actually simplifies the remaining inverse transform operation – integration with respect to τ along C – allowing the ultimate solution to be obtained essentially by inspection. We will consider the terms containing b_1 and b_2 separately and begin with the b_1 term. For this term in the transform, let the variable $\tau_1 = \gamma_{3_1}x_3$ stand in for τ in the inverse Laplace transform operation in Eq. (C.12). With this parameterization, Γ_2 can be interpreted to be a function of τ_1 such that $d\Gamma_2 = \dfrac{1}{x_3}\dfrac{\partial\Gamma_2}{\partial\gamma_{3_1}}d\tau_1$. A similar parameterization for the term containing b_2 can be carried out ($\tau_3 = \gamma_{3_3}x_3$) so that combining Eq. (C.21) with (C.20) (including (C.16)-(C.19)) yields the following:

$$\begin{aligned} v_3 = -i(2\pi)^2\{&\int_C \mathrm{Re}\int_0^{\infty} H(\tau_1 - x_3)b_1 s{\Gamma_2}^{-1/2}\frac{\partial\Gamma_2}{\partial\tau_1}\exp(-s\tau_1)\exp(s\tau)d\tau_1 ds \\ &+\int_C \mathrm{Re}\int_0^{\infty} H(\tau_3 - \alpha^{-1/2}x_3)b_2 s{\Gamma_2}^{-1/2}\frac{\partial\Gamma_2}{\partial\tau_3}\exp(-s\tau_3)\exp(s\tau)d\tau_3 ds\}\ . \end{aligned} \tag{C.22}$$

Equation (C.22) appears to be a forward Laplace transform immediately followed by the inverse Laplace transform operation. The result of these operations can be written directly as follows:

$$v_3 = (2\pi)^{-1}\,\mathrm{Re}[H(\tau_1 - x_3)b_1 s{\Gamma_2}^{-1/2}\frac{\partial\Gamma_2}{\partial\tau_1} + H(\tau_3 - \alpha^{-1/2}x_3)b_2 s{\Gamma_2}^{-1/2}\frac{\partial\Gamma_2}{\partial\tau_3}]\ . \tag{C.23}$$

Next, we need to express Γ_2 in terms of γ_3 and also put the derivatives in Eq. (C.23) into recognizable forms. To achieve the first of these tasks, Eq. (C.13) can be written as a quadratic in Γ_2 and can be solved to yield the dependence of Γ_2 on γ_3 as follows:

$$\Gamma_2 = (2\beta)^{-1}\{\chi{\gamma_3}^2 - (1+\beta) \mp [(\chi{\gamma_3}^2 - (1+\beta))^2 - 4\beta(\alpha{\gamma_3}^4 - (1+\alpha){\gamma_3}^2 + 1)]^{1/2}\}\Big|_{\substack{\gamma_{3_1}\to -\\ \gamma_{3_3}\to +}}\ . \tag{C.24}$$

The derivative can be obtained most directly by differentiating the quadratric equation for Γ_2 and this yields the result:

$$\frac{\partial \Gamma_2}{\partial \gamma_3} = \frac{2\chi\gamma_3\Gamma_2 + 2(1+\alpha)\gamma_3 - 4\alpha\gamma_3^{\,3}}{2\beta\Gamma_2 + (1+\beta) - \chi\gamma_3^{\,2}} . \tag{C.25}$$

where the appropriate sign in Eq. (C.24) is chosen based on the term in Eq. (C.23) being evaluated. For completeness, this derivative is written for these terms using previous definitions as follows:

$$\frac{\partial \Gamma_2}{\partial \tau_1} = \frac{1}{x_3}\frac{\partial \Gamma_2}{\partial \gamma_{3_1}} = \frac{1}{x_3}\frac{\partial \Gamma_2}{\partial \gamma_3}\bigg|_{\gamma_3=\gamma_{3_1}} \quad \text{and} \quad \frac{\partial \Gamma_2}{\partial \tau_3} = \frac{1}{x_3}\frac{\partial \Gamma_2}{\partial \gamma_{3_3}} = \frac{1}{x_3}\frac{\partial \Gamma_2}{\partial \gamma_3}\bigg|_{\gamma_3=\gamma_{3_3}} . \tag{C.26}$$

With all terms expressed explicitly, it only remains to compute displacement values as a function of reduced time. For the first term in Eq. (C.23), we let $\tau = \tau_1 = \gamma_{3_1} x_3$ and this is used to compute γ_{3_1}. This value for γ_3 is used in Eq. (C.24) to compute Γ_2 (choosing the correct sign) as well as the derivative in Eq. (C.26). This value for Γ_2 is used in (C.14c) to compute γ_{3_3}. Finally, these values for γ_{3_1}, γ_{3_3} and Γ_2 are used with Eqs. (C.17) and (C.19) to evaluate the coefficient b_1. The second term is evaluated in a similar fashion but the parameterization begins with $\tau = \tau_3 = \gamma_{3_3} x_3$. This completes the evaluation of displacements along the x_3 axis in a half space arising from a shear dipole line source with step time dependence acting on a surface perpendicular to the axis of symmetry in a transversely isotropic material. These displacements are independent of the orientation of the line on this surface since it is a plane of isotropy. The strength of the laser line source dipole can be obtained by multiplying the unit source used here by $q_0[\beta_{22} - (c_{23}/c_{33})\beta_{33}]/C$ where q_0 is the line fluence [J/m], β_{ij} are the components of the thermal stress tensor and C is the heat capacity [$Jm^{-3}K^{-1}$] [C38,C39].

C.2.2 Epicentral Displacements Perpendicular to Symmetry Axis: Line Source Perpendicular to Symmetry Axis – Case II

For this case, the surface of the half-space is perpendicular to the x_2-axis and a shear stress is applied on the surface along the x_1-axis such that:

$$\sigma_{23}\big|_{x_2=0} = \delta'(x_3)H(t) \tag{C.27}$$

and it is assumed that there are no contributions from the normal stress to the surface tractions such that:

$$\sigma_{22}\big|_{x_2=0} = 0 . \tag{C.28}$$

Owing to the symmetries of these stresses, once again, only displacements and derivatives associated with the x_2 and x_3 directions need to be considered. The equations of motion, given in Eqs. (C.9) and (C.10),

are unchanged and the overall solution process follows the previous development. Indeed, since we are interested in epicentral displacements ($x_1 = 0$), it can be used in its entirety if the indices are exchanged ($2 \rightleftarrows 3$) and the definitions of the normalized moduli are updated ($\alpha = c_{22} / c_{44}$, $\beta = c_{33} / c_{44}$).

C.2.3 Epicentral Displacements Perpendicular to Symmetry Axis: Line Source Parallel to Symmetry Axis – Case III

For this case, the surface of the half-space is perpendicular to the x_2-axis and a shear stress is applied on the surface containing the x_3-axis such that:

$$\sigma_{21}\big|_{x_2=0} = \delta'(x_1)H(t) \tag{C.29}$$

and it is assumed that there are no contributions from the normal stress to the surface tractions such that:

$$\sigma_{22}\big|_{x_2=0} = 0\,. \tag{C.30}$$

Owing to the symmetries of these stresses, only displacements and derivatives associated with the x_1 and x_2 directions need to be considered. Since we are interested in epicentral displacements ($x_3 = 0$), it appears that the previous development can be used in its entirety with a change of indices ($3 \rightarrow 1$). However, with this change the reduced time and displacements would need to be redefined along with the normalized moduli (the shear wave travels at a different speed from the previous cases). Since the previous solutions were expressed in terms of these quantities, the treatment here will maintain the definitions for reduced time and displacement. With the following normalized modulus definitions: $\alpha = c_{11} / c_{44} = c_{22} / c_{44}$, $\eta = c_{66} / c_{44}$ and $\kappa = \eta + c_{12} / c_{44}$, the equations of motion are expressed as follows:

$$\alpha v_{1.11} + \eta v_{1,22} + \kappa v_{2,12} = v_{1,\tau\tau} \tag{C.31}$$

and

$$\alpha v_{2,22} + \eta v_{2,11} + \kappa v_{1,21} = v_{2,\tau\tau}\,. \tag{C.32}$$

Recalling that $c_{66} = (c_{11} - c_{12})/2$, the normalized moduli are related ($\kappa = \alpha - \eta$) and only two independent moduli remain. This indicates the material behaves isotropically for the conditions imposed here since the elastic response of isotropic materials can be described using two moduli. The solution to this problem is well known and can be written directly. Even so, we will choose to follow the solution process outlined previously, and compare the result to ones already known. Using notation developed previously, the following expression for the epicentral displacement is obtained:

$$v_2 = (2\pi)^{-1}\,\mathrm{Re}[H(\tau_1 - \eta^{-1/2}x_2)b_1 s\Gamma_1^{-1/2}\frac{\partial\Gamma_1}{\partial\tau_2} + H(\tau_3 - \alpha^{-1/2}x_2)b_2 s\Gamma_1^{-1/2}\frac{\partial\Gamma_1}{\partial\tau_3}] \tag{C.33}$$

where $\tau_1 = \gamma_{2_1} x_2$, $\tau_3 = \gamma_{2_3} x_2$ and

$$\gamma_{2_1} = (2\alpha\eta)^{-1/2}\{[(\alpha+\eta)+\chi\gamma_1{}^2]+\varphi^{1/2}\}^{1/2} = (\gamma_1{}^2+\eta^{-1})^{1/2} \tag{C.34a}$$

$$\gamma_{2_3} = (2\alpha\eta)^{-1/2}\{[(\alpha+\eta)+\chi\gamma_1{}^2]-\varphi^{1/2}\}^{1/2} = (\gamma_1{}^2+\alpha^{-1})^{1/2} \tag{C.34b}$$

with $\chi = \alpha^2+\eta^2-\kappa^2 = 2\alpha\eta$ and $\varphi = [(\alpha+\eta)+\chi\gamma_1{}^2]^2 - 4\alpha\eta(\alpha\gamma_1{}^2+1)(\eta\gamma_1{}^2+1) = \eta-\alpha$. The coefficients, b_1 and b_2, for this case are:

$$\begin{aligned} b_1 &= -(c_{44}\rho)^{-1/2}(\kappa\gamma_1{}^2/(\eta s))[(\eta-\kappa)(1+\eta\gamma_1{}^2)-\alpha\eta\gamma_{2_3}{}^2]\gamma_{2_1} \div D \\ &= (c_{44}\rho)^{-1/2}(\kappa^2\gamma_1{}^2\gamma_{2_1})(1+2\eta\gamma_1{}^2)/(\eta s) \div D \end{aligned} \tag{C.35}$$

and

$$\begin{aligned} b_2 &= (c_{44}\rho)^{-1/2}(\kappa\gamma_1{}^2/(\eta s))[(\eta-\kappa)(1+\eta\gamma_1{}^2)-\alpha\eta\gamma_{2_1}{}^2]\gamma_{2_3} \div D \\ &= -(c_{44}\rho)^{-1/2}(2\kappa^2\gamma_1{}^2\gamma_{2_1}{}^2\gamma_{2_3}/s) \div D \end{aligned} \tag{C.36}$$

with

$$\begin{aligned} D &= \kappa(\gamma_{2_1}-\gamma_{2_3})\{(1+\eta\gamma_1{}^2)[(2(\kappa-\eta)+\chi/\eta)\gamma_1{}^2+\alpha/\eta)]+\alpha\gamma_{2_1}\gamma_{2_3}\} \\ &= \kappa^2\eta\gamma_{2_1}[(2\gamma_1{}^2+1/\eta)^2-4\gamma_1{}^2\gamma_{2_1}\gamma_{2_3}] \end{aligned} \tag{C.37}$$

where the second expression for D is readily recognized as being related to the Rayleigh denominator [C23]. As expected, the coefficients b_1 and b_2 agree with previous developments for isotropic materials [C17,C19]. Using this form for the transformed solution, the inversions can be carried out. First, $\Gamma_1 = \gamma_1^2$ must be expressed in terms of γ_2 and the derivatives in Eq. (C.31) must be written in a recognizable form. Following the steps presented for the first case yields:

$$\Gamma_1 = (2\alpha\eta)^{-1}\{\chi\gamma_2{}^2-(\alpha+\eta)\mp[(\chi\gamma_2{}^2-(\alpha+\eta))^2-4\alpha\eta(\alpha\gamma_2{}^2-1)(\eta\gamma_2{}^2-1)]^{1/2}\}\Big|_{\substack{\gamma_{2_1}\to-\\ \gamma_{2_3}\to+}}, \tag{C.38}$$

where the appropriate sign in Eq. (C.38) is chosen based on the term in Eq. (C.33) being evaluated. For this case, the results for Γ_1 are simple – both Eq. (C.38) and (C.34) give $\Gamma_1 = \gamma_{2_1}^2 - \eta^{-1}$ or $\Gamma_1 = \gamma_{2_3}^2 - \alpha^{-1}$. The corresponding derivative

$$\frac{\partial\Gamma_1}{\partial\gamma_2} = \frac{2\chi\gamma_2\Gamma_1+2(\alpha+\eta)\gamma_2-4\alpha\eta\gamma_2{}^3}{2\alpha\eta\Gamma_1+(\alpha+\eta)-\chi\gamma_2{}^2} = 2\gamma_2 \tag{C.39}$$

simplifies considerably as well. For completeness, this derivative is written for various terms using previous definitions as follows:

$$\frac{\partial\Gamma_1}{\partial\tau_1} = \frac{1}{x_2}\frac{\partial\Gamma_1}{\partial\gamma_{2_1}} = \frac{1}{x_2}\frac{\partial\Gamma_1}{\partial\gamma_2}\bigg|_{\gamma_2=\gamma_{2_1}} = \frac{2\gamma_{2_1}}{x_2} \qquad \frac{\partial\Gamma_1}{\partial\tau_3} = \frac{1}{x_2}\frac{\partial\Gamma_1}{\partial\gamma_{2_3}} = \frac{1}{x_2}\frac{\partial\Gamma_1}{\partial\gamma_2}\bigg|_{\gamma_2=\gamma_{2_3}} = \frac{2\gamma_{2_3}}{x_2}. \tag{C.40}$$

To compute displacements, we let $\tau = \tau_1 = \gamma_{2_1} x_2$ (this defines a value for γ_{2_1}). This value is used to compute Γ_1 as well as the derivative in Eq. (C.40). The result for Γ_1 along with Eq. (C.34b) yield γ_{2_3}. Finally, these values for γ_{2_1}, γ_{2_3} and Γ_1 are used with Eqs. (C.35) and (C.37) to evaluate the coefficient b_1. The second term is evaluated in a similar fashion but the parameterization begins with $\tau = \tau_3 = \gamma_{2_3} x_2$. This completes the evaluation of displacements along the x_2 axis in a half space arising from a line source parallel to the axis of symmetry with step time dependence acting on a surface containing the axis of symmetry. The strength of the laser line source dipole for this case can be obtained by multiplying the unit source by $q_0 \alpha_L c_{11}^{-1}(c_{11} + 2c_{12})(c_{11} - c_{12}) / C$ where α_L is the linear thermal expansion coefficient – other terms were defined previously [C38,C39]. This result agrees with previous developments for laser line source excitation of isotropic half-spaces [C19].

C.3. Results – Evaluation of Displacements

The reduced displacements expressed in Eqs. (C.23) and (C.31) will be evaluated for the epicentral range $x_i = 1$ as a function of the reduced time, τ, since this simplifies interpretation of the results. Also, only anisotropy that conforms to the requirements of Class I systems will be considered [C40] – namely, those for which $\alpha > \beta$ and $\alpha + 1 < \chi < \chi_0(\alpha, \beta)$ where χ_0 is a positive root of the cubic equation:

$$0 = \chi^3 + l\chi^2 + h\chi + n \tag{C.41}$$

with

$$l = 1 + \alpha\beta + 2(1-\alpha)(1-\beta), \tag{C.42}$$

$$h = -(\alpha + \beta)[(1-\alpha) + (1-\beta) + 2\alpha\beta], \tag{C.43}$$

$$n = -[(\alpha + \beta)^2(1 + \alpha\beta) + 16\alpha\beta(1-\alpha)(1-\beta)]. \tag{C.44}$$

While other systems adhering to the requirements of Classes II-V could be considered [C37], the solution processes required for these systems demand additional attention to the computation of inverse transforms. Related details can be found in work by Payton [C37] and Hurley [C38]. In addition, the solutions generated here for transversely isotropic materials might also apply (with restrictions) to materials displaying certain tetragonal ($422, 4\text{mm}, \bar{4}2\text{m}, 4/\text{mmm}$) and cubic symmetries when appropriate definitions for directions and modulus components are made. Since the focus of the current presentation is on transversely isotropic materials, displacements will be computed for titanium which, in single crystal form, adheres to the Class I requirements and has the following normalized moduli: $\alpha = c_{33} / c_{44} = 3.88$, $\beta = c_{11} / c_{44} = 3.47$, $c_{23} / c_{44} = 1.48$ and $c_{12} / c_{44} = 1.97$ ($c_{44} = 46.7$ GPa) [C37,C40]. Using these values, epicentral displacements were computed using the previous development

for the three cases and are shown in Fig. C.2. For Case I, the orientation of the line source has no effect on the arrival times of the either the shear or longitudinal waves since the plane of isotropy is perpendicular to the propagation direction and shear waves are polarized in this plane. For Cases II and III the longitudinal waves propagate at the same speed since the direction of propagation is the same, but the respective shear waves arrive at different times – these are the cases that display shear wave birefringence. Beyond the relative wavespeeds for the different modes in Cases II and III, the general shapes of the waveforms between the wave arrivals differ significantly. These shapes are dictated by the form of the solution related to the longitudinal wave – the wavespeed depends on β while the overall shape depends on various factors that include c_{23} in Case II and c_{12} in Case III. This result is significant since it illustrates that the shape of waveforms can be used to infer principal components of the modulus tensor that do not affect wavespeed when propagation along principal directions is considered.

Even though titanium illustrates the necessary results related to shear birefringence, a second material is considered in which the anisotropy is not nearly as strong. While this material is hypothetical, it is meant to represent materials that might otherwise be isotropic (such as polycrystalline materials with random grain orientation) but have an induced anisotropy that results from some type of forming operation (such as preferred grain orientation that occurs in metallic materials during drawing/extrusion) or externally applied, uniaxial stress (that causes changes to the stiffnesses according to the third order elastic constants) [C41]. For this case, the following values for the various moduli have been assumed: $\alpha = c_{33} / c_{44} = 4.00$, $\beta = c_{11} / c_{44} = 3.60$, $c_{23} / c_{44} = 1.79$ and $c_{12} / c_{44} = 1.80$ – these values yield $c_{66} / c_{44} = 0.90$. This material is also Class I and adheres to the same restrictions on moduli as titanium. Results for the epicentral displacements are shown in Fig. C.3. The overall trends for wavespeed are the same as for titanium – differences exist between Cases I and II/III for the longitudinal wavespeeds; Cases II and III display shear birefringence. Even so, since the assumed values for c_{23} and c_{12} are much closer in this material, the waveform shapes for Cases I-III are relatively similar when compared to those obtained for titanium.

C.4. Discussion

The models developed here can be used for the interpretation of laser ultrasonic, line source measurements in transversely isotropic materials – specifically those that satisfy Class I restrictions. To facilitate these types of measurements, some knowledge of the symmetry axis direction can be used to guide choices regarding propagation direction and polarization orientation. Absent orientation information, symmetry axis direction can be determined by screening for shear wave birefringence – so long as the sample geometry allows for measurements along and perpendicular to the symmetry axis. For

propagation perpendicular to the symmetry axis, the results presented here indicate that only two measurements are required to accurately characterize birefringence. However, in practice, multiple line orientations might be necessary to accurately identify maximum and minimum shear wavespeeds especially if the direction of the symmetry axis is not clearly defined. This uncertainty in axis direction can arise in systems where applied stresses induce anisotropy in materials that might otherwise behave isotropically. For these types of measurements, the laser line source will generally launch shear waves that propagate at wavespeeds characteristic of the normal modes of the system and the quantity of energy deposited into each mode will depend on the orientation of the line relative to the symmetry axis. While the case of the arbitrarily-oriented line source has not been modeled here, it can be assumed that the measured waveforms would yield shear wavespeeds intermediate between the extrema presented by Cases II and III. These intermediate values might not accurately reflect the actual constitution of the material and could simply represent an artifact of the measurement process.

Unlike the idealized conditions represented in the models developed here, actual measurements can be complicated by factors that reflect the characteristics of the material. For example, in Cases II and III, the longitudinal wave time-of-arrival should be independent of line orientation and this is likely the case even if the laser line is not uniformly intense across the sample surface. However, if there are variations in the photothermal/thermoelastic conversion processes related to sample inhomogeneity as the line orientation is varied, then the arrival time for the longitudinal wave will change – this same inhomogeneity will affect shear wave times-of-arrival and could interfere with accurate identification of birefringence associated with elastic anisotropy. Also, microstructural variations that result in elastic inhomogeneity could produce variations in wave arrivals that might impact shear birefringence measurements. However, if the times-of-arrival for the longitudinal wave do not vary with line orientation, then this could be a good indication that any variation in shear wave arrival times is a result of anisotropy and not inhomogeneity.

For ultrasonic characterization methods, wavespeeds have been historically used to characterize elastic anisotropy since they relate directly to the stiffnesses of the material. Shear wave birefringence, as determined by wavespeed differences between orthogonally polarized modes, is one effect that can occur and this has been the focus of the presentation here. However, material anisotropy yields effects beyond those typically associated with birefringence. In particular, the character of displacements after the longitudinal arrival depends on components of the tensor that do not influence wavespeeds in bulk media for propagation along high symmetry directions. These displacements occur when finite sources act and are related to off-diagonal components of the stiffness tensor – c_{2233} and c_{1122} for the cases considered in this work. These components factor into the Poisson effect and can be measured using various techniques. For isotropic materials, they can be determined using measurements of longitudinal and shear

wavespeeds. For transversely anisotropic materials, additional measurements are required. Longitudinal wavespeed in a long, thin rod depends on the anisotropic Young's modulus – this along with bulk wavespeeds can be used to determine the values of off-diagonal tensor components. The results presented here offer the possibility of determining values for three tensor components from a single waveform obtained using a single experiment. This has not been investigated previously, but offers paths for investigation that could resolve long-standing issues related to point- and line-source Green's function interpretation of elastic wave measurements. Ultimately, simple and robust methods for determining off-diagonal components of the stiffness tensor might be used to infer characteristics of materials microstructure that are not captured when isotropic material behavior is assumed.

C.5. Conclusions

Models for ultrasonic waves produced using laser line sources in transversely anisotropic materials have been presented that show how shear wave birefringence measurements using laser sources can be used to characterize aspects of material anisotropy. By assuming adiabatic heating as well as uniform line intensity and homogeneous photothermal conversion processes, these models provide a simple description that highlights the effects of elastic anisotropy on wave propagation. The analytical solutions in this work allow for easy computation for comparison to experimental measurements and also permit specific characteristics of waveforms to be related to various stiffness components. For propagation in high symmetry directions, diagonal components of the elastic stiffness tensor dictate the wavespeeds of longitudinal and shear waves. While these arrivals are notable and are the focus of most ultrasonics measurements, the results in this study show how off-diagonal components can affect the overall shape of laser ultrasonic waveforms between wavefronts – the possibility exists to extract three stiffness tensor components from a single waveform. Since most materials with crystalline microstructural elements display some level of elastic anisotropy, laser line source measurements of the kind outlined here could provide insight into the constitution of the microstructure with a limited number of measurements.

References

[C1] H Lamb. On the propagation of tremors over the surface of an elastic solid, Philosophical Transactions of the Royal Society of London Series a-Containing Papers of a Mathematical or Physical Character. 203 (1904) 1-42.

[C2] SK Bhandari, R Chander. On the exact evaluation of displacements within a semi-infinite solid due to a buried line source, Proceedings of the Indian Academy of Sciences-Earth and Planetary Sciences. 93 (1984) 37-45.

[C3] E Kausel. Lamb's problem at its simplest, Proceedings of the Royal Society A-Mathematical Physical and Engineering Sciences. 469 (2013).

[C4] M Hirao, N Hara, H Fukuoka, K Fujisawa. Ultrasonic monitoring of texture in cold-rolled steel sheets, J.Acoust.Soc.Am. 84 (1988) 667-672.

[C5] F Reverdy, B Audoin. Elastic constants determination of anisotropic materials from phase velocities of acoustic waves generated and detected by lasers, J.Acoust.Soc.Am. 109 (2001) 1965-1972.

[C6] S Dixon, C Edwards, SB Palmer. Texture measurements of metal sheets using wideband electromagnetic acoustic transducers, Journal of Physics D-Applied Physics. 35 (2002) 816-824.

[C7] S Crampin, S Peacock. A review of shear-wave splitting in the compliant crack-critical anisotropic Earth, Wave Motion. 41 (2005) 59-77.

[C8] D Su, MH Santare, GA Gazonas. The effect of crack face contact on the anisotropic effective moduli of microcrack damaged media, Eng.Fract.Mech. 74 (2008) 1436-1455.

[C9] D Su, MH Santare, GA Gazonas. An effective medium model for elastic waves in microcrack damaged media, Eng.Fract.Mech. 75 (2008) 4104-4116.

[C10] X Wang, MH Santare, GA Gazonas. Anisotropic effective moduli of microcracked materials under antiplane loading, Eng.Fract.Mech. 76 (2009) 1910-1919.

[C11] R Mloszewski, DA Hutchins, J Francoeur. Characterization of roll-drawn polypropylene using shear-wave birefringence, J.Mater.Sci. 27 (1992) 2413-2419.

[C12] E Schneider. Ultrasonic birefringence effect - its application for materials characterizations, Optics and Lasers in Engineering. 22 (1995) 305-323.

[C13] A Moreau, D Levesque, M Lord, M Dubois, JP Monchalin, C Padioleau, et al. On-line measurement of texture, thickness and plastic strain ratio using laser-ultrasound resonance spectroscopy, Ultrasonics. 40 (2002) 1047-1056.

[C14] B Dutton, RJ Dewhurst. Anisotropy measurements in metal alloys using a laser/electromagnetic acoustic transducer array system, Appl.Phys.Lett. 89 (2006).

[C15] S Dixon, MP Fletcher, G Rowlands. The accuracy of acoustic birefringence shear wave measurements in sheet metal, J.Appl.Phys. 104 (2008).

[C16] DA Hutchins, RJ Dewhurst, SB Palmer. Directivity patterns of laser-generated ultrasound in aluminum, J.Acoust.Soc.Am. 70 (1981) 1362-1369.

[C17] JR Bernstein, JB Spicer. Line source representation for laser-generated ultrasound in aluminum, J.Acoust.Soc.Am. 107 (2000) 1352-1357.

[C18] D Royer. Mixed matrix formulation for the analysis of laser-generated acoustic waves by a thermoelastic line source, Ultrasonics. 39 (2001) 345-354.

[C19] I Arias, JD Achenbach. Thermoelastic generation of ultrasound by line-focused laser irradiation, Int.J.Solids Structures. 40 (2003) 6917-6935.

[C20] JD Achenbach. Laser excitation of surface wave motion, J.Mech.Phys.Solids. 51 (2003) 1885-1902.

[C21] I Arias, JD Achenbach. A model for the ultrasonic detection of surface-breaking cracks by the scanning laser source technique, Wave Motion. 39 (2004) 61-75.

[C22] WX Hu, ML Qian. Acoustic field excited by a pulsed laser line source in a cylinder, Ultrasonics. 44 (2006) E1187-E1190.

[C23] KF Graff. Wave Motion in Elastic Solids, Dover Publications, New York, 1991.

[C24] RG Payton. 2-dimensional pulse propagation in a 2-parameter anisotropic elastic solid, Q Appl Math. 27 (1969) 147-&.

[C25] RG Payton. 2-dimensional anisotropic elastic waves emanating from a point source, Proceedings of the Cambridge Philosophical Society-Mathematical and Physical Sciences. 70 (1971) 191-&.

[C26] RL Ryan. Pulse propagation in a transversely isotropic half-space, J.Sound Vibrat. 14 (1971) 511-&.

[C27] RG Payton. Epicenter motion of a transversely isotropic elastic half-space due to a suddenly applied buried point source, Int.J.Eng.Sci. 17 (1979) 879-887.

[C28] MJP Musgrave, RG Payton. Head wave contributions to elastic wave fields in a transversely isotropic half-space, Q J Mech Appl Math. 34 (1981) 235-250.

[C29] RG Payton. Epicenter and epicentral-axis motion of a transversely isotropic elastic half-space, SIAM J Appl Math. 40 (1981) 373-389.

[C30] RL Weaver, W Sachse, KY Kim. Transient elastic waves in a transversely isotropic plate, Journal of Applied Mechanics-Transactions of the ASME. 63 (1996) 337-346.

[C31] A Rahman, F Ahmad. Representation of the displacement in terms of scalar functions for use in transversely isotropic materials, J.Acoust.Soc.Am. 104 (1998) 3675-3676.

[C32] EA Kraut. Advances in the theory of anisotropic elastic wave propagation, Rev.Geophys. 1 (1963) 401-448.

[C33] RG Payton. Symmetry-axis elastic-waves for transversely isotropic media, Q Appl Math. 35 (1977) 63-73.

[C34] RG Payton. Plane strain displacement and stress waves induced in a transversely isotropic elastic solid by a line source, Zeitschrift Fur Angewandte Mathematik Und Physik. 29 (1978) 262-272.

[C35] JJ Wang, BQ Xu, ZH Shen, XW Ni, J Lu. Numerical simulation of thermoelastic stress field and laser ultrasound in transversely isotropic plate, Japanese Journal of Applied Physics. 47 (2008) 956-963.

[C36] Y Pan, M Perton, C Rossignol, B Audoin. The transient response of a transversely isotropic cylinder under a laser point source impact, Ultrasonics. 44 (2006) E823-E827.

[C37] RG Payton. Elastic Wave Propagation in Transversely Isotropic Media, Martinus Nijhoff, The Hague, Netherlands, 1983.

[C38] DH Hurley. An Investigation of the Anisotropic and Heterogeneous Nature of Laser Generated Ultrasound in Carbon-Fiber-Reinforced Epoxy and Single Crystal Materials, The Johns Hopkins University, Baltimore, Maryland, 1997.

[C39] DH Hurley, JB Spicer. Line source representation for laser-generated ultrasound in an elastic transversely isotropic half-space, J.Acoust.Soc.Am. 116 (2004) 2914-2922.

[C40] MJP Musgrave, RG Payton. Criteria for elastic-waves in anisotropic media - a consolidation, Journal of Elasticity. 14 (1984) 269-285.

[C41] CM Sayers, DR Allen. The influence of stress on the principal polarization directions of ultrasonic shear-waves in textured steel plates, Journal of Physics D-Applied Physics. 17 (1984) 1399-1413.

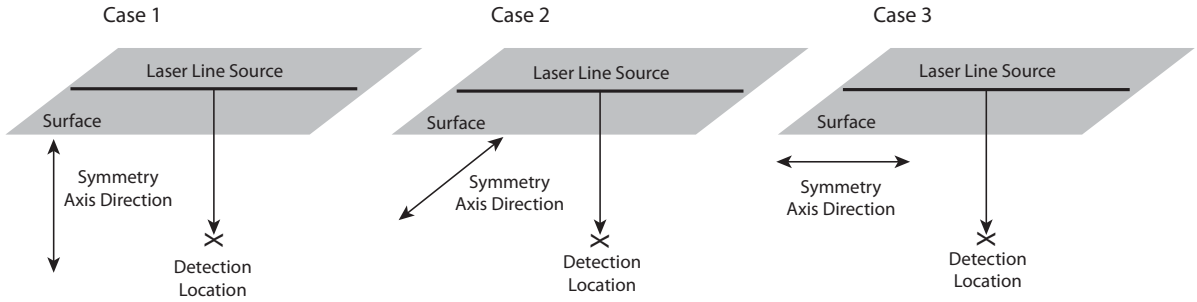

Figure C.1: Geometries for laser line source excitation of a transversely isotropic half-space. The three cases here illustrate the relationship of the surface- and source-orientation relative to the symmetry axis and also show the epicentral locations where displacements are evaluated.

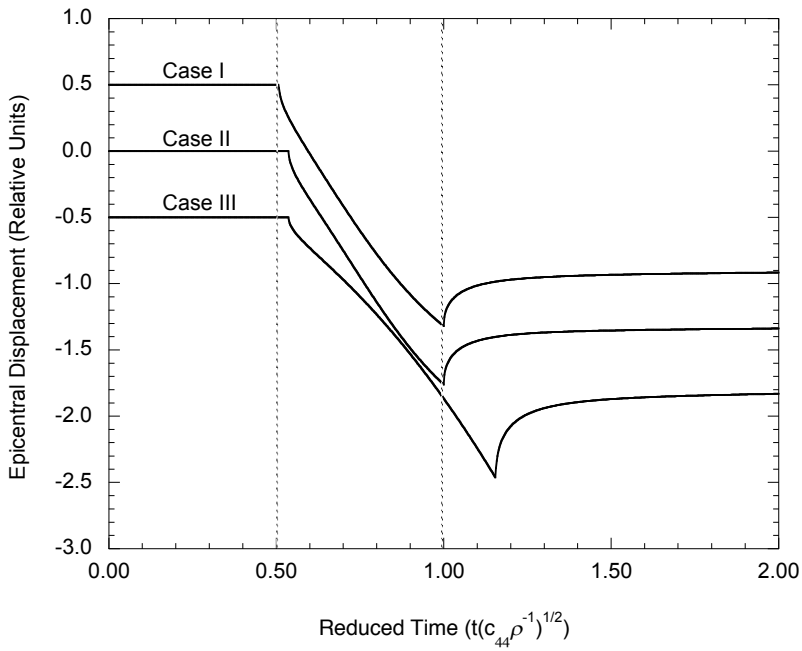

Figure C.2: Epicentral waveforms for laser-line excitation of single-crystal titanium half-spaces corresponding to the three geometries illustrated in Fig. C.1. Waveforms are shown offset for clarity.

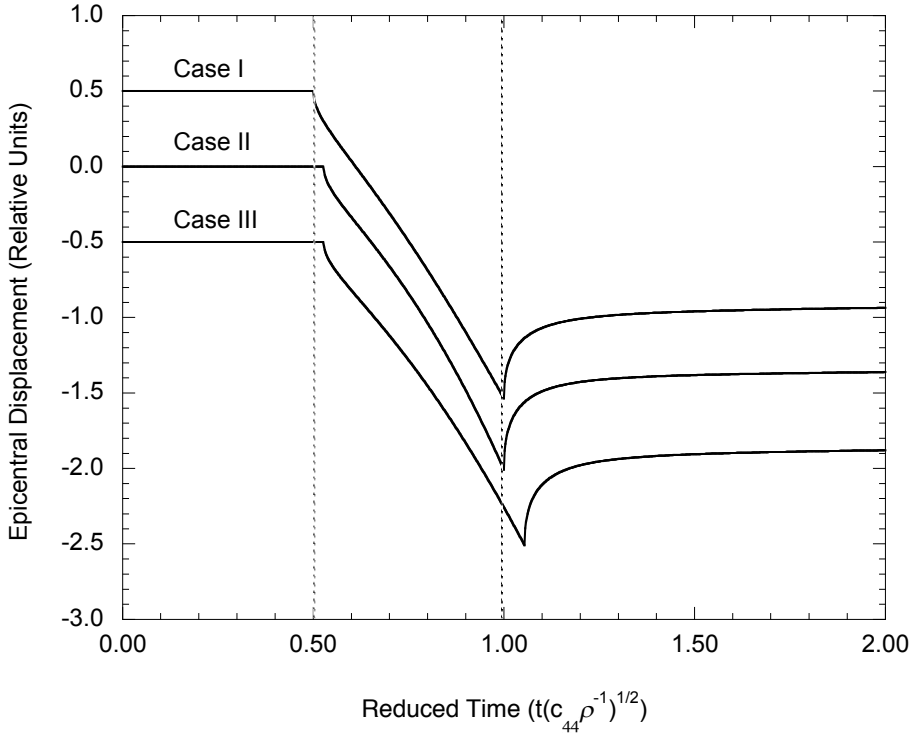

Figure C.3: Epicentral waveforms for laser-line excitation of transversely-isotropic half-spaces corresponding to the three geometries illustrated in Fig. C.1. The moduli for this material represent those that might result from preferred grain or microcrack orientations that yield transverse isotropy. Waveforms are shown offset for clarity.

Section D: Subsurface, Thermoelastic Line Source Excitation of a Transversely Isotropic Half-Space

D.1. Introduction

Subsurface line sources of elastic waves have been studied in fields from quantitative seismology [D1] to medical imaging [D2] in order to understand the character of the wavefields produced by these sources and to use the various wavefield components to characterize the nature (geometry and elastic properties) of the system being studied. In some cases, the line source of interest is primarily mechanical [D3-5] while in others it has a thermoelastic nature being derived from a source of thermal energy that couples to elastic deformations in the system. The thermoelastic line source is the focus of this work. This type of source could be derived from a range of physical and/or chemical processes (e.g. endothermic/exothermic chemical reactions, phase transformations, photothermal processes) that could take place along a line. One of the most frequently studied is the laser line source in which light is focused to a line-like geometry in/on a material and acts as a thermoelastic source in regions where optical absorption occurs [D6-12]. Under conditions that produce subsurface absorption or that transport thermal energy away from absorption sites, subsurface sources will result and the associated elastic wavefield will depend on their distribution [D13,D14]. If these sources form a linear array below the surface, then a single line source representation could be sufficient for modeling purposes. More complicated distributions can be modeled using a suitable superposition of individual line sources.

Most studies that consider subsurface line sources assume isotropic properties for the host material [D15]. This type of description can be useful for many materials, but most materials systems display some level of anisotropy owing to underlying crystallinity or as result of preferred orientational arrangement of constituent components and defects in the overall material structure. In many cases, when anisotropy is present, materials can be expected to display transverse isotropy. Materials systems that are transversely isotropic with respect to their thermal and elastic properties include those with hexagonal symmetry [D16] as well as those that undergo particular processing that results in higher transverse symmetry. This anisotropy might be small and might not be taken into account when characterization is performed, but this does not mean it should be ignored especially since it might ultimately impact materials performance. There is clearly a need to develop models for interpretation of data gathered in transversely isotropic materials systems [D17-19]. The purpose of the work presented here is to provide descriptions of material displacements in the wavefield surrounding a subsurface, thermoelastic line source in a transversely isotropic half space. These descriptions provide insight into the overall character of these sources in anisotropic materials and can also be used to model more generalized source distributions that might occur in a range of physical systems. Explicit expressions for displacements along the symmetry axis for

a receiver in an epicentral location are derived and are computed to illustrate various general aspects of the wavefield. In particular, the characteristics of wavefronts associated with various modes are considered along with the nature of direct shear wave emission by this type of source. This type of emission does not occur in isotropic systems. Finally, the relationship between solutions obtained in this work to those associated with the application of boundary tractions/stresses is derived – this shows how the surface-borne thermoelastic line source can be represented as a surface, shear stress dipole [D19,D20].

D.2. Modeling the Thermoelastic Line Source

The presentation largely follows work previously presented by Payton on line source excitation of transversely isotropic systems [D16, D21-25] but the source specification in the current work differs significantly. Also, Payton considers a range of systems in which wavefield characteristics are quite complicated, but the focus of this presentation is only on systems that satisfy the requirements for Class I materials [D16,D26,D27]. Aspects of the current work also relate closely to previous studies by Hurley [D18,D20], but this treatment focuses principally on subsurface sources and the epicentral displacements produced by these types of sources and includes explicit, closed-form expressions for these displacements that have not been shown previously.

D.2.1 Specification of the Source

We start this development with the equation of motion for a general, anisotropic, thermoelastic solid:

$$c_{ijkl}u_{l,kj} + f_i - \beta_{ij}T_{,j} = \rho u_{i,tt} \tag{D.1}$$

where c_{ijkl} is the elastic stiffness tensor, u_l is the material displacement in the l direction, f_i is the body force acting in the i direction, ρ is the material density, β_{ij} is the thermal stress coefficient tensor and T is the temperature rise above the background, ambient level. Subscripting notation has been used where the indices range from 1 to 3 and represent spatial directions/variables while the index t represents time. The summation convention has been used and subscripts after commas indicate differentiation with respect to the corresponding variable. Equation (D.1) is re-written as follows so that normalized stiffnesses can be used to describe the elastic response of the material [D16]:

$$c_{ijkl}v_{l,kj} / c_{2323} + (f_i - \beta_{ij}T_{,j}) / z_{2323} = v_{i,\tau\tau} \tag{D.2}$$

where $v_i = u_i(c_{2323}/\rho)^{1/2}$, $z_{2323} = (\rho c_{2323})^{1/2}$ and $\tau = (c_{2323}/\rho)^{1/2}t$. This normalization simplifies notation to be used in this development and introduces the reduced displacement, v_i, the reduced time, τ as well as the acoustic impedance, z_{2323}.

In the subsequent development, all body forces will be assumed to be zero, $f_i = 0$, and all solutions will assume the thermal stress approximation – namely, coupling of elastic disturbances to thermal transport will be ignored. In addition, thermal diffusion will be suppressed by assuming that the thermal conductivity in the medium is zero. Under these conditions, a subsurface, line, heating source aligned along the x_1 axis with impulse time dependence (schematically shown in Fig. D.1), can be described through the temperature field term in Eq. (D.1) as follows [D19]:

$$\beta_{ij}T_{,j} = (c_{ijkl}\alpha_{kl})(\theta\delta(x_2)\delta(x_3)H(t))_{,j} \tag{D.3}$$

where α_{kl} is the linear thermal expansion coefficient tensor ($\beta_{ij} = c_{ijkl}\alpha_{kl}$) and θ is heat source power per unit length divided by the heat capacity of the material. Evaluating the derivatives in Eq. (D.3) yields the following two "thermoelastic forces" that can be used with Eq. (D.2):

$$\varphi_2 = \beta_{22}T_{,2} = \theta(c_{2222}\alpha_{22} + c_{2233}\alpha_{33})\delta(x_2)_{,2}\delta(x_3)H(t) = \phi_2\delta(x_2)_{,2}\delta(x_3)H(t) \tag{D.4}$$

$$\varphi_3 = \beta_{33}T_{,3} = \theta(c_{3322}\alpha_{22} + c_{3333}\alpha_{33})\delta(x_2)\delta(x_3)_{,3}H(t) = \phi_3\delta(x_2)\delta(x_3)_{,3}H(t) \tag{D.5}$$

where $\phi_2 = \theta(c_{2222}\alpha_{22} + c_{2233}\alpha_{33})$ and $\phi_3 = \theta(c_{3322}\alpha_{22} + c_{3333}\alpha_{33})$.

D.2.2 Solution Method and Analytical Results

Having specified the essential content of the physical problem, we can proceed to perform the necessary mathematical manipulations to obtain the material displacements that result from this type of source. Noting symmetries associated with the source, Eq. (D.2) yields the following:

$$(\beta v_{2,22} + v_{2,33} - v_{2,\tau\tau}) + \kappa v_{3,23} = \varphi_2 / z_{2323} \tag{D.6}$$

$$\kappa v_{2,23} + (\alpha v_{3,33} + v_{3,22} - v_{3,\tau\tau}) + = \varphi_3 / z_{2323} \tag{D.7}$$

where $\alpha = c_{3333} / c_{2323}$, $\beta = c_{1111} / c_{2323}$, and $\kappa = 1 + c_{2233} / c_{2323}$. These equations need to be solved subject to the appropriate boundary conditions. In this work, we are interested in analytical, closed form solutions and the process to obtain these will employ transform techniques since these will convert differential equations to algebraic expressions that can be manipulated readily. The following definitions for the various forward transforms will be used in the subsequent development:

$$\begin{aligned}\bar{v}_i &= \int_0^\infty \int_{-\infty}^\infty \int_{-\infty}^\infty v_i \exp(-ik_2x_2 - ik_3x_3 - s\tau)\,dx_2\,dx_3\,d\tau \\ &= \int_{-\infty}^\infty \int_{-\infty}^\infty \hat{v}_i \exp(-ik_2x_2 - ik_3x_3)\,dx_2\,dx_3 = \int_{-\infty}^\infty \tilde{v}_i \exp(-ik_3x_3)\,dx_3\end{aligned} \tag{D.8}$$

which are paired with the corresponding inverse transforms:

$$v_i = -i(2\pi)^{-3}\int_C\int_{-\infty}^{\infty}\int_{-\infty}^{\infty}\bar{v}_i \exp(ik_2x_2 + ik_3x_3 + s\tau)\,dk_2\,dk_3\,ds$$
$$= -i(2\pi)^{-2}\int_C\int_{-\infty}^{\infty}\tilde{v}_i \exp(ik_2x_2 + s\tau)\,dk_2\,ds = -i(2\pi)^{-1}\int_C \hat{v}_i \exp(s\tau)\,ds \quad . \tag{D.9}$$

Applying the forward transform operations to Eqs. (D.6) and (D.7) yields the following:

$$\bar{v}_2(\beta k_2^2 + k_3^2 + s^2) + \bar{v}_3(\kappa k_2 k_3) = -(\phi_2 / z_{2323})(ik_2 / s) \tag{D.10}$$

and

$$\bar{v}_2(\kappa k_2 k_3) + \bar{v}_3(k_2^2 + \alpha k_3^2 + s^2) = -(\phi_3 / z_{2323})(ik_3 / s)\,. \tag{D.11}$$

These equations are readily solved simultaneously to yield the displacement transforms:

$$\bar{v}_2 = [(k_2^2 + \alpha k_3^2 + s^2)\Phi_2 - (\kappa k_2 k_3)\Phi_3] \div D \tag{D.12}$$

and

$$\bar{v}_3 = [(\beta k_2^2 + k_3^2 + s^2)\Phi_3 - (\kappa k_2 k_3)\Phi_2] \div D \tag{D.13}$$

where $\Phi_2 = -(\phi_2 / z_{2323})(ik_2 / s)$, $\Phi_3 = -(\phi_3 / z_{2323})(ik_3 / s)$ and

$$D = \alpha k_3^4 + k_3^2[(\alpha+1)s^2 + k_2^2(1+\alpha\beta-\kappa^2)] + (k_2^2 + s^2)(\beta k_2^2 + s^2)\,. \tag{D.15}$$

All that remains is to impose boundary conditions and complete the various inverse transform operations. To begin, we will consider inversion with respect to the transform pair (x_3, k_3) since this will allow assessment of the boundary conditions. Let k_{3n}^* be the nth of the 4 roots to the bi-quadratic equation when $D = 0$. These roots are expressed as follows:

$$k_{31}^* = -k_{32}^* = (2\alpha)^{-1/2}\{-[(\alpha+1)s^2 + \chi k_2^2] - \zeta^{1/2}\}^{1/2} \tag{D.16}$$

$$k_{33}^* = -k_{34}^* = (2\alpha)^{-1/2}\{-[(\alpha+1)s^2 + \chi k_2^2] + \zeta^{1/2}\}^{1/2} \tag{D.17}$$

where the second subscript indexes each root, $\chi = 1 + \alpha\beta - \kappa^2$ and $\zeta = [(\alpha+1)s^2 + \chi k_2^2]^2 - 4\alpha(k_2^2 + s^2)(\beta k_2^2 + s^2)$. At this point, let $k_{3n} = ik_{3n}^*$. This change essentially demands $k_{31} > 0$ and $k_{33} > 0$ for Class I materials (see Ref. [D16] pp. 133-134 for related discussion) and will prove convenient later in the development. With this definition, the denominator, D, may be re-expressed to yield the following:

$$D^{-1} = \alpha^{-1}[(k_3^2 + k_{31}^2)^{-1} - (k_3^2 + k_{33}^2)^{-1}](k_{33}^2 - k_{31}^2)^{-1}\,. \tag{D.18}$$

Since $(k_3^2 + k_{3n}^2)^{-1} = (2ik_3)^{-1}[(k_{3n} - ik_3)^{-1} - (k_{3n} + ik_3)^{-1}]$, the transforms in Eqs. (D.12) and (D.13) have simple poles at $k_3 = \pm ik_{3n}$. Inversion of $\bar{v}_3$ with respect to (x_3, k_3) can be performed to get $\tilde{v}_3 = \tilde{v}_{31} + \tilde{v}_{33}$ where $\tilde{v}_{31}$ is the portion of the doubly-transformed solution for v_3 associated with the k_{31} root and similarly for $\tilde{v}_{33}$. These parts of $\tilde{v}_3$ can be written as follows:

$$\tilde{v}_{31} = -(2\alpha)^{1/2}(k_{33}^2 - k_{31}^2)^{-1}(sz_{44})^{-1}[(\beta k_2^2 + s^2 - k_{31}^2)\Phi_3 - \kappa k_2^2 \Phi_2][e^{k_{31}x_3}H(-x_3) - e^{-k_{31}x_3}H(x_3)] \quad \text{(D.19)}$$

and

$$\tilde{v}_{33} = (2\alpha)^{1/2}(k_{33}^2 - k_{31}^2)^{-1}(sz_{44})^{-1}[(\beta k_2^2 + s^2 - k_{33}^2)\Phi_3 - \kappa k_2^2 \Phi_2][e^{k_{33}x_3}H(-x_3) - e^{-k_{33}x_3}H(x_3)] \quad \text{(D.20)}$$

where $H(x_3)$ is the Heaviside step function acting along the x_3 axis. Inverting these expressions with respect to the transform pairs (x_2, k_2) and (s, τ) yields the displacements in the x_3 direction that result from a thermoelastic line source in an infinite space. Corresponding solutions for displacements in the x_2 direction could be written as well, but since the current focus is on displacements in the x_3 direction, only the results in Eqs. (D.19) and (D.20) are needed to complete this development.

To obtain a corresponding solution for a half-space with a free surface located at $x_3 = -d$, the following boundary conditions based on the disappearance of surface tractions must be satisfied:

$$\sigma_{33}\big|_{x_3=-d} = 0 \ , \ \ \sigma_{23}\big|_{x_3=-d} = 0 \quad \text{(D.21)}$$

where

$$\sigma_{33} = c_{3333}u_{3,3}^g + c_{3322}u_{2,2}^g \ , \ \sigma_{23} = c_{2323}(u_{2,3}^g + u_{3,2}^g) \, . \quad \text{(D.22)}$$

Here, u_i^g refers to the general solution of the governing differential equation which is composed of homogeneous and inhomogeneous (or particular) solutions – $u_i^g = u_i^h + u_i$ or $\tilde{v}_3^g = (\tilde{v}_{31}^h + \tilde{v}_{33}^h) + (\tilde{v}_{31} + \tilde{v}_{33})$ for reduced displacements in the transform domain. The inhomogeneous solution corresponds to infinite space and has already been written so it can be used in the boundary conditions when they are expressed in a reduced form in the doubly transformed space:

$$0 = [\alpha \tilde{v}_{3,3}^g + ik_2(\kappa - 1)\tilde{v}_2^g]\big|_{x_3=-d} \ \text{ and } \ 0 = [\tilde{v}_{2,3}^g + ik_2\tilde{v}_3^g]\big|_{x_3=-d} \quad \text{(D.23)}$$

where $\tilde{v}_i^g = \tilde{v}_i^h + \tilde{v}_i$. Based on the form obtained for the inhomogeneous solution, the following homogeneous solutions are assumed:

$$\tilde{v}_2^h = A_1 e^{-k_{31}x_3} + A_3 e^{-k_{33}x_3} \ \text{ and } \ \tilde{v}_3^h = B_1 e^{-k_{31}x_3} + B_3 e^{-k_{33}x_3} \quad \text{(D.24)}$$

where A_n and B_n are undetermined coefficients that are needed to satisfy the given boundary conditions. The additional requirements on the undetermined coefficients come from Eq. (D.7) when the right hand side is taken to be zero (yielding the homogeneous form of the equation):

$$A_n / B_n = R_n = (\alpha k_{3n}^2 - k_2^2 - s^2)(i\kappa k_2 k_{3n})^{-1}. \tag{D.25}$$

This expression requires that solutions associated with k_{31} and k_{33} be linearly independent. It follows that if $\tilde{v}_3^h = \tilde{v}_{31}^h + \tilde{v}_{33}^h$ then $\tilde{v}_2^h = R_1\tilde{v}_{31}^h + R_3\tilde{v}_{33}^h$ – equivalent expressions hold for $\tilde{v}_3$ and $\tilde{v}_2$. Also, it should be noted that if the sign of the propagation constant, k_{3n}, changes then the sign of R_n also changes. With this additional information in place, $\tilde{v}_i^g = \tilde{v}_i^h + \tilde{v}_i$ can be used with the boundary conditions and values for B_1 and B_3 can be obtained. The algebra involved is tedious but yields the following results:

$$B_1 = [(ad+bc)\tilde{v}_{31}\big|_{x_3=0^-} + 2bd\,\tilde{v}_{33}\big|_{x_3=0^-} e^{-(k_{31}+k_{33})d}](ad-bc)^{-1} \tag{D.26}$$

$$B_3 = -[2ac\,\tilde{v}_{31}\big|_{x_3=0^-} e^{-(k_{31}+k_{33})d} + (ad+bc)\tilde{v}_{33}\big|_{x_3=0^-} e^{-2k_{33}d}](ad-bc)^{-1} \tag{D.27}$$

with $a = k_{33}[\alpha k_{31}^2 + (\kappa-1)(k_2^2+s^2)]$, $b = k_{31}[\alpha k_{33}^2 + (\kappa-1)(k_2^2+s^2)]$, $c = [\alpha k_{31}^2 + (\kappa-1)k_2^2 - s^2]$ and $d = [\alpha k_{33}^2 + (\kappa-1)k_2^2 - s^2]$.

The complete solution, $\tilde{v}_3^g$, can be written as follows for regions of the half-space where $x_3 > 0$:

$$\begin{aligned}\tilde{v}_3^g = \{&[-(ad-bc)\tilde{v}_{31}\big|_{x_3=0^-} + (ad+bc)e^{-2k_{31}d}\,\tilde{v}_{31}\big|_{x_3=0^-} + 2bde^{-(k_{31}+k_{33})d}\,\tilde{v}_{33}\big|_{x_3=0^-}]e^{-k_{31}x_3} \\ &+[-(ad-bc)\tilde{v}_{33}\big|_{x_3=0^-} - (ad+bc)e^{-2k_{33}d}\,\tilde{v}_{33}\big|_{x_3=0^-} - 2ace^{-(k_{31}+k_{33})d}\,\tilde{v}_{31}\big|_{x_3=0^-}]e^{-k_{33}x_3}\}(ad-bc)^{-1}.\end{aligned} \tag{D.29}$$

In this expression, terms of the form $\tilde{v}_{3i}\big|_{x_3=0^-}$ should be evaluated using Eqns. (D.19) and (D.20) for negative values of x_3 in the limit as $x_3 \to 0$. While various algebraic simplifications to this result can be made, this form for the solution will be used since it facilitates interpretations that will be made in subsequent sections. There are essentially six components of the solution given in Eq. (D.29) such that it can be expressed as $\tilde{v}_3^g = \tilde{v}_{3_S}^g + \tilde{v}_{3_{SS}}^g + \tilde{v}_{3_{LS}}^g + \tilde{v}_{3_L}^g + \tilde{v}_{3_{LL}}^g + \tilde{v}_{3_{SL}}^g$. These components will be considered individually in the following to highlight the physical meaning behind each. Before doing so, it will be noted that significant simplification of the solution can be achieved by considering the factors $(ad+bc)$ and $(ad-bc)$ which appear in various terms. These quantities can be written as follows:

$$ad+bc = \kappa(k_{33}+k_{31})\{(k_2^2+s^2)[(2(\kappa-1)+\chi)k_2^2 + \alpha s^2] - \alpha k_{31}k_{33}s^2\} \tag{D.30}$$

and

$$ad - bc = \kappa(k_{33} - k_{31})\{(k_2^2 + s^2)[(2(\kappa - 1) + \chi)k_2^2 + \alpha s^2] + \alpha k_{31}k_{33}s^2\}. \qquad \text{(D.31)}$$

The term $(ad - bc)$ corresponds to the usual Rayleigh denominator that appears in related treatments for isotropic materials [D15].

The overall solution consists of six arrivals at the point of observation a distance of $x_3 + d$ from the boundary – three associated with shear displacements and three associated with longitudinal displacements. If the receiver is epicentrally located at $x_2 = 0$, the six arrivals can be described as follows:

1. Direct Shear Wave. This portion of the wavefield travels a distance x_3 from the source to the receiver and is represented by $\tilde{v}_{3_S}^g = -\tilde{v}_{31}\big|_{x_3=0^-} e^{-k_{31}x_3}$.

2. Reflected Shear-to-Shear Wave. This shear wave travels a distance of $x_3 + 2d$ and includes reflection of a shear wave at the boundary. This arrival corresponds to $\tilde{v}_{3_{SS}}^g = (ad + bc)e^{-k_{31}(x_3+2d)}\,\tilde{v}_{31}\big|_{x_3=0^-}(ad - bc)^{-1}$.

3. Longitudinal-to-Shear Conversion. This arrival is a shear wave that results from longitudinal wave conversion at the boundary (travels a distance d as a longitudinal wave and a distance $x_3 + d$ as a shear wave). This arrival is represented by $\tilde{v}_{3_{LS}}^g = 2bde^{-k_{33}d - k_{31}(x_3+d)}\,\tilde{v}_{33}\big|_{x_3=0^-}(ad - bc)^{-1}$.

4. Direct Longitudinal Wave. This portion of the wavefield corresponds to the longitudinal wave that travels a distance x_3 directly between the source and the receiver and is given by $\tilde{v}_{3_L}^g = -\tilde{v}_{33}\big|_{x_3=0^-} e^{-k_{33}x_3}$.

5. Reflected Longitudinal-to-Longitudinal Wave. This is a longitudinal wave that travels a distance of $x_3 + 2d$ and results from longitudinal wave reflection at the boundary. This arrival corresponds to $\tilde{v}_{3_{LL}}^g = -(ad + bc)e^{-k_{33}(x_3+2d)}\,\tilde{v}_{33}\big|_{x_3=0^-}(ad - bc)^{-1}$.

6. Shear-to-Longitudinal Conversion. This is a longitudinal wave that results from shear wave conversion at the boundary (travels a distance d as a shear wave and a distance $x_3 + d$ as a longitudinal wave). This arrival corresponds to $\tilde{v}_{3_{SL}}^g = -2ace^{-k_{31}d - (k_{33}+d)x_3}\,\tilde{v}_{31}\big|_{x_3=0^-}(ad - bc)^{-1}$.

The solution given in Eq. (D.29) is in a doubly transformed space and inversions with respect to k_2 and s need to be completed. The inverse transform with respect to k_2 is as follows:

$$\hat{v}_3^g = (2\pi)^{-1}\int_{-\infty}^{\infty}\tilde{v}_3^g \exp(ik_2x_2)dk_2 = (\pi)^{-1}\,\mathrm{Re}\int_0^{\infty}\tilde{v}_3^g \exp(ik_2x_2)dk_2 \tag{D.32}$$

where $\hat{v}_3^g$ represents the Laplace transform of v_3^g and the final equality in Eq. (D.32) results from $\tilde{v}_3^g$ being even with respect to k_2. The remainder of this treatment will be on epicentral displacements where $x_2 = 0$ since these are measured in various experiments. Also, the transforms simplify considerably when $x_2 = 0$ and yield analytical expressions for the displacements. Since $\tilde{v}_3^g$ in Eq. (D.32) depends on ${k_2}^2$ – this suggests a change in the integration variable. Letting $\mathrm{K}_2 = {k_2}^2$ yields the following:

$$\hat{v}_3^g = (2\pi)^{-1}\,\mathrm{Re}\int_0^{\infty}\tilde{v}_3^g {\mathrm{K}_2}^{-1/2} d\mathrm{K}_2\,. \tag{D.33}$$

While this change might not appear to have achieved any significant advantage, it allows the remaining inverse Laplace transform operation to be performed essentially by inspection.

For these final steps, we will consider the terms corresponding to each of the six arrivals in Eq. (D.29) separately as follows:

1. Direct Shear Wave. This wave corresponds to the term containing the exponential $e^{-k_{31}x_3}$ and will be referred to as $v_{3_S}^g$. For this term, let the variable $\tau' = k_{31}x_3 / s$ serve as the reduced time in a forward Laplace transform operation (see Eq. (D.9)). With this parameterization, K_2 can be interpreted to be a function of τ' such that $d\mathrm{K}_2 = \dfrac{\partial \mathrm{K}_2}{\partial \tau'}d\tau' = \dfrac{s}{x_3}\dfrac{\partial \mathrm{K}_2}{\partial k_{31}}d\tau'$. Combining Eq. (D.9) with (D.33) and (D.29) yields the following:

$$v_{3_S}^g = -i(2\pi)^{-2}\int_C \mathrm{Re}\int_0^{\infty} H(\tau' - x_3)(-{\mathrm{K}_2}^{-1/2}\frac{\partial \mathrm{K}_2}{\partial \tau'}\tilde{v}_{31}\big|_{x_3=0^-})\;\big|_{k_{31}=s\tau'/x_3}\exp(-s\tau')\exp(s\tau)d\tau' ds \tag{D.34}$$

where

$$\mathrm{K}_2 = (2\beta)^{-1}\{\chi k_3^2 - (1+\beta)s^2 - [(\chi k_3^2 - (1+\beta)s^2)^2 - 4\beta(\alpha k_3^2 - s^2)(k_3^2 - s^2)]^{1/2}\}\big|_{k_3=k_{31}} \tag{D.35}$$

and

$$k_{33} = k_{31}^{-1}[(\mathrm{K}_2 + s^2)(\beta\mathrm{K}_2 + s^2)/\alpha]^{1/2}\,. \tag{D.36}$$

It should be noted that in arriving at Eq. (D.34), the change in the variable of integration from K_2 to τ' requires a change in the limits such that the lower limit $\mathrm{K}_2 = 0$ yields $\tau' = x_3$. Introducing the

Heaviside step function into the integrand allows the lower limit to be changed to zero. Also, the expression for K_2 given in Eq. (D.35) can be obtained by solving the quadratic equation provided by Eq. (D.15) when $D=0$. Even though the derivative in the integrand can be obtained by differentiating Eq. (D.35) directly, an easier approach is to differentiate the quadratric equation for K_2 (again, from Eq. (D.15) when $D=0$) and allowing the derivative to be expressed in terms of both k_3 and K_2. This yields the result:

$$\frac{\partial \mathrm{K}_2}{\partial k_3} = \frac{2\chi k_3 \mathrm{K}_2 + 2(\alpha+1)s^2 k_3 - 4\alpha k_3^3}{2\beta \mathrm{K}_2 + (\beta+1)s^2 - \chi k_3^2}. \tag{D.37}$$

Equation (D.34) appears to be a forward Laplace transform immediately followed by the inverse transform operation. The result for the displacement can be written immediately as follows:

$$v_{3_S}^g = (2\pi)^{-1} H(\tau' - x_3)\mathrm{Re}(-\mathrm{K}_2^{-1/2} \frac{\partial \mathrm{K}_2}{\partial \tau'} \tilde{v}_{31}\big|_{x_3=0^-}) \;\big|_{k_{31}=s\tau'/x_3}. \tag{D.38}$$

The displacement, $v_{3_S}^g$, can be expressed as a function of τ' by noting that $k_{31} = s\tau'/x_3$. Since $k_3 = k_{31}$ in Eqs. (D.35)-(D.37), K_2, $\frac{\partial \mathrm{K}_2}{\partial k_3}$, k_{33} as well as $\tilde{v}_{31}\big|_{x_3=0^-}$ can be written directly and substituted into Eq. (D.38) to obtain $v_{3_S}^g$. The resulting equation is quite lengthy and it is not clear that expressing it would provide additional insight into the nature of the solution. It will not be shown here.

2. Reflected Shear-to-Shear Wave. This wave corresponds to the term containing the exponential $e^{-k_{31}(x_3+2d)}$ and will be referred to as $v_{3_{SS}}^g$. For this term, let the variable $\tau' = k_{31}(x_3+2d)/s$ act as the reduced time in a forward Laplace transform operation. With this parameterization, K_2 is a function of τ' such that $d\mathrm{K}_2 = \frac{\partial \mathrm{K}_2}{\partial \tau'} d\tau' = \frac{s}{(x_3+2d)} \frac{\partial \mathrm{K}_2}{\partial k_{31}} d\tau'$. Combining Eq. (D.9) with (D.33) and (D.29) yields the following:

$$v_{3_{SS}}^g = -i(2\pi)^{-2} \int_C \mathrm{Re} \int_0^\infty H(\tau' - (x_3+2d))(\frac{ad+bc}{ad-bc} \mathrm{K}_2^{-1/2} \frac{\partial \mathrm{K}_2}{\partial \tau'} \tilde{v}_{31}\big|_{x_3=0^-}) \;\big|_{k_{31}=s\tau'/(x_3+2d)} \exp(-s\tau')\exp(s\tau) d\tau' ds \tag{D.39}$$

where K_2, $\frac{\partial \mathrm{K}_2}{\partial k_3}$ as well as k_{33} have the same form as for the direct shear wave. As before, Eq. (D.39) appears to be a forward Laplace transform immediately followed by the inverse transform operation. The result can be written directly as follows:

$$v_{3_{SS}}^{g} = (2\pi)^{-1} H(\tau' - (x_3 + 2d)) \mathrm{Re}\left(\frac{ad+bc}{ad-bc} \mathrm{K}_2^{-1/2} \frac{\partial \mathrm{K}_2}{\partial \tau'} \tilde{v}_{31}\Big|_{x_3=0^-}\right)\Bigg|_{k_{31}=s\tau'/(x_3+2d)} . \tag{D.40}$$

3. Longitudinal-to-Shear Conversion. This wave corresponds to the term containing the exponential $e^{-k_{33}d - k_{31}(x_3+d)}$ and will be referred to as $v_{3_{LS}}^{g}$. For this term, the variable $\tau' = [k_{31}(x_3+d) + k_{33}d]/s$ acts as the reduced time. With this parameterization, K_2 can once again be interpreted to be a function of τ', but the relationship is more complicated. Combining Eq. (D.9) with (D.33) and (D.29) yields the following:

$$v_{3_{LS}}^{g} = -i(2\pi)^{-2} \int_C \mathrm{Re} \int_0^\infty H(\tau' - [(x_3+d) + x_3 d/\alpha^{1/2}])(2bd\mathrm{K}_2^{-1/2} \frac{\partial \mathrm{K}_2}{\partial \tau'} \tilde{v}_{33}\Big|_{x_3=0^-}) \Big|_{\tau'=[k_{31}(x_3+d)+k_{33}d]/s} \exp(-s\tau')\exp(s\tau) d\tau' ds. \tag{D.41}$$

In this case, evaluation of the derivative $d\mathrm{K}_2 = \frac{\partial \mathrm{K}_2}{\partial \tau'} d\tau'$ cannot be accomplished in the same way as was done in the previous two cases. Here we note that τ' is a function of K_2 such that

$$\frac{\partial \mathrm{K}_2}{\partial \tau'} = \left(\frac{\partial \tau'}{\partial \mathrm{K}_2}\right)^{-1} = s\left((x_3+d)\frac{\partial k_{31}}{\partial \mathrm{K}_2} + d\frac{\partial k_{33}}{\partial \mathrm{K}_2}\right)^{-1}. \tag{D.42}$$

The process for evaluating the various terms can be carried out by assuming values for K_2, computing values for k_{31} and k_{33} with Eqs. (D.16) and (D.17) (along with subsequent definitions), and using these values to determine τ' as well as the derivative terms $\frac{\partial k_{3i}}{\partial \mathrm{K}_2} = \left(\frac{\partial \mathrm{K}_2}{\partial k_3}\right)^{-1}\Bigg|_{k_3=k_{3i}}$. Having computed the values for these terms, the displacement is given by

$$v_{3_{LS}}^{g} = (2\pi)^{-1} H(\tau' - [(x_3+d) + x_3 d/\alpha^{1/2}]) \mathrm{Re}\left(\frac{2bd}{ad-bc} \mathrm{K}_2^{-1/2} \frac{\partial \mathrm{K}_2}{\partial \tau'} \tilde{v}_{33}\Big|_{x_3=0^-}\right)\Bigg|_{\tau'=[k_{31}(x_3+d)+k_{33}d]/s} . \tag{D.43}$$

4. Direct Longitudinal Wave. This arrival corresponds to the term containing $e^{-k_{33}x_3}$ and will be referred to as $v_{3_L}^{g}$. A similar parameterization as was used for the direct shear term can be employed – the exponential suggesting the choice $\tau' = k_{33}x_3/s$ such that $d\mathrm{K}_2 = \frac{\partial \mathrm{K}_2}{\partial \tau'} d\tau' = \frac{s}{x_3}\frac{\partial \mathrm{K}_2}{\partial k_{33}} d\tau'$. Combining Eq. (D.9) with (D.33) and (D.29) yields the following:

$$v_{3_L}^{g} = -i(2\pi)^{-2} \int_C \mathrm{Re} \int_0^\infty H(\tau' - x_3)(-\mathrm{K}_2^{-1/2} \frac{\partial \mathrm{K}_2}{\partial \tau'} \tilde{v}_{33}\Big|_{x_3=0^-}) \Big|_{k_{33}=s\tau'/x_3} \exp(-s\tau')\exp(s\tau) d\tau' ds \tag{D.44}$$

where

$$\mathrm{K}_2 = (2\beta)^{-1}\{\chi k_3^2 - (1+\beta)s^2 + [(\chi k_3^2 - (1+\beta)s^2)^2 - 4\beta(\alpha k_3^2 - s^2)(k_3^2 - s^2)]^{1/2}\}\Big|_{k_3=k_{33}} . \tag{D.45}$$

The derivative $\dfrac{\partial \mathrm{K}_2}{\partial k_3}$ as well as k_{31} can be obtained using Eqs. (D.37) and (D.36) with $k_3 = k_{33}$. Again, the result for this displacement can be written directly as follows:

$$v_{3_L}^g = (2\pi)^{-1} H(\tau' - x_3/\alpha^{1/2})\mathrm{Re}(-\mathrm{K}_2^{-1/2}\frac{\partial \mathrm{K}_2}{\partial \tau'}\tilde{v}_{33}\Big|_{x_3=0^-})\ \Big|_{k_{33}=s\tau'/x_3} . \tag{D.46}$$

5. Reflected Longitudinal-to-Longitudinal Wave. This wave corresponds to the term containing the exponential $e^{-k_{33}(x_3+2d)}$ and will be referred to as $v_{3_{LL}}^g$. For this term, let the variable $\tau' = k_{33}(x_3+2d)/s$ take on the role of reduced time in the Laplace transform operation in Eq. (D.8). The solution process follows the one outlined for other waves and yields the result:

$$v_{3_{LL}}^g = (2\pi)^{-1} H(\tau' - (x_3+2d)/\alpha^{1/2})\mathrm{Re}(-\frac{ad+bc}{ad-bc}\mathrm{K}_2^{-1/2}\frac{\partial \mathrm{K}_2}{\partial \tau'}\tilde{v}_{33}\Big|_{x_3=0^-})\Big|_{k_{33}=s\tau'/(x_3+2d)} \tag{D.47}$$

where K_2 and its derivative are the same as were used for the direct longitudinal wave.

6. Shear-to-Longitudinal Conversion. This wave corresponds to the term containing the exponential $e^{-k_{31}d-k_{33}(x_3+d)}$ and will be referred to as $v_{3_{SL}}^g$. For this term, let $\tau' = [k_{31}d + k_{33}(x_3+d)]/s$. The rest of the development essentially follows that outlined for the longitudinal-to-shear conversion. Combining Eq. (D.9) with (D.33) and (D.29) yields the following:

$$v_{3_{SL}}^g = -i(2\pi)^{-2}\int_C \mathrm{Re}\int_0^\infty H(\tau' - [d + (x_3+d)/\alpha^{1/2}])(-2ac\mathrm{K}_2^{-1/2}\frac{\partial \mathrm{K}_2}{\partial \tau'}\tilde{v}_{31}\Big|_{x_3=0^-})\ \Big|_{\tau'=[k_{33}d+k_{31}(x_3+d)]/s}\exp(-s\tau')\exp(s\tau)d\tau' a$$

(D.48)

such that the displacment is given by:

$$v_{3_{SL}}^g = (2\pi)^{-1} H(\tau' - [d + (x_3+d)/\alpha^{1/2}])\mathrm{Re}(-2ac\mathrm{K}_2^{-1/2}\frac{\partial \mathrm{K}_2}{\partial \tau'}\tilde{v}_{31}\Big|_{x_3=0^-})\ \Big|_{\tau'=[k_{33}d+k_{31}(x_3+d)]/s} . \tag{D.49}$$

The overall solution is simply the sum of the individual terms: $v_3^g = v_{3_S}^g + v_{3_{SS}}^g + v_{3_{LS}}^g + v_{3_L}^g + v_{3_{LL}}^g + v_{3_{SL}}^g$. Even though this expression for the displacements is complete and only requires evaluation of closed-form terms, it is quite cumbersome and very little, if any, simplification can be accomplished unless

special circumstances prevail. While various authors have explored elements of related solutions, few (if any) have considered all the terms individually especially those related to mode conversion at the boundary [D15,D16].

D.3. Computed Results – Graphical Presentation

The overall character of the solution can be illustrated by computing displacement as a function of time for assumed conditions. Consider titanium for which $c_{1111} = 162$, $c_{2233} = 69$, $c_{3333} = 181$ and $c_{2323} = 46.7$ (all in units of GPa); $\alpha_{22} = 9.23 \times 10^{-6}$ and $\alpha_{33} = 9.57 \times 10^{-6}$ (both in units of $1/°\mathrm{C}$). Suppose the point of observation is fixed such that the direct shear wave arrives at a time equal to $t = \tau(\rho / c_{2323})^{1/2}$ with $\tau = 1$ (the prime notation has been removed). Note that the units for τ correspond to length and are determined by the choice of units for time and the wavespeed, $(c_{2323} / \rho)^{1/2}$. Under these conditions, observation occurs at the location $x_3 = \tau = 1$. In addition, it will be assumed that the source is located at a distance $d = x_3 / 20$ from the surface. For this geometry and material, the displacements at the point of observation as a function of reduced time will take the form shown in Fig. D.2a. In these results, the displacements have been divided by θ (the heat source power per unit length divided by the heat capacity) and multiplied by $(c_{2323} / \rho)^{1/2}$ (according to the original normalization carried out in Eq. (D.2)) and should be interpreted in terms of the related units. The most prominent features of the waveform are the first arrival (the direct longitudinal wave) at $\tau \approx 0.5$ and the longitudinal-to-longitudinal reflection – the negative-going peak after the first arrival. Since the waveform is composed of 6 different arrivals, it is useful to display each of these separately as is shown in Fig. D.2b. Here the first and second arrivals (L and LL respectively) are shown along with the mode-converted shear-to-longitudinal wave (SL), the direct shear wave (S) followed by the longitudinal-to-shear conversion (LS). The final arrival is the reflected shear wave (SS). Among the arrivals after the first two, the most significant is the longitudinal-to-shear conversion – all others lack distinct onsets or have low amplitudes making them difficult to identify in the total displacement waveform. It should be noted that when computing the various contributions to the total displacement, arrivals that do not undergo mode conversion can be manipulated quite easily since reduced time is a direct input parameter. However, for mode-converted arrivals, reduced time is a derived quantity and, as a result, adding these terms to the others requires some care.

Additional results are shown in Fig. D.3 where a series of displacement waveforms illustrates the effect of changing the depth of the source below the surface in titanium. For this series, the source-to-receiver distance is fixed so that the shear wave arrives at the reduced time $\tau = 1$ (corresponding to $x_3 = 1$) while the source-to-surface distance (d) takes on fractional values of x_3 – namely, 0.000, 0.005, 0.025, 0.050

and 0.075. This geometry fixes the arrival times for the direct longitudinal wave (at $\tau = \alpha^{-1/2} \approx 0.5$) and the direct shear wave ($\tau = 1.0$) – all other modes have arrival times that vary as the boundary is moved relative to the source with the most prominent being the longitudinal reflection. When the source is located far away from the surface, the reflected longitudinal wave is delayed relative to the direct wave by $\Delta\tau = 2d\alpha^{-1/2}$ and this difference decreases as the source approaches the surface. When the source is at the surface ($d = 0.000$), the wavefronts for the direct and reflected longitudinal waves cancel one another and the character of the overall waveform is changed significantly. The only distinct feature associated with shear displacements is the longitudinal-to-shear conversion. For the surface source, the arrival time for this component is $\tau = 1.0$, but as the source moves away from the boundary, the arrival is delayed by $\Delta\tau = d(\alpha^{-1/2} + 1)$ – unlike for the reflected longitudinal wave, this shift is difficult to identify in the waveform owing to the nature of the shear wavefronts.

D.4. Results for Special Conditions

D.4.1 Wavefront Arrivals

The wavefront arrivals provide insight into the overall character of the waveforms produced by this type of source. Since the directly transmitted shear and longitudinal waves factor into all components of the wavefield, attention will be focused on these. For times approaching the arrival of the direct longitudinal wave, the following result is obtained for the displacement:

$$v_{3_L}^g\Big|_{\tau\to(x_3/\alpha^{1/2})^+} = (2\pi)^{-1} H(\tau - x_3/\alpha^{1/2})[\phi_3/z_{44}][2\alpha^{3/2}(\alpha-1)/(\alpha+\kappa^2-1)]^{1/2}(\tau - x_3/\alpha^{1/2})^{-1/2} x_3^{-1/2}. \tag{D.50}$$

The temporal dependence of the wavefront is a reciprocal, square root singularity – this is typical for line sources and indicates that the computed waveforms shown in this work are approximations to the actual result. In addition, the amplitude varies as the reciprocal, square root of the distance between the source and the point of observation – again, this is the usual result for line sources and is related to conservation of energy. When the reduced time approaches the arrival time for the direct shear wave, the following result is obtained for the epicentral displacement due to the shear wave:

$$v_{3_S}^g\Big|_{\tau\to x_3^+} = (2\pi)^{-1} H(\tau - x_3)[\kappa(\phi_2 - \kappa\phi_3/(\alpha-1))/z_{44}][2\alpha/(\beta+\kappa^2-\alpha\beta)]^{3/2}[2(\alpha-1)]^{1/2}(\tau - x_3)^{1/2} x_3^{-3/2}. \tag{D.51}$$

In this case, the amplitude varies with the square root of time and does not exhibit any singularity – this prevents this portion of the wavefield from contributing significantly to the overall epicentral displacement. In addition, the wavefront displacement amplitude decreases more rapidly than $x_3^{-1/2}$ and does not contribute to overall energy transport to large distances ($x_3 >> 1$). These results indicate that

the directly transmitted longitudinal wave as well as displacements directly associated with this wave will dominate the overall character of epicentral displacements.

D.4.2 Shear Wave Emission

Direct emission of shear waves by the source is related to the material anisotropy and accounts for three of the terms in the full solution. Both elastic and thermal expansion anisotropy contribute to the existence of these portions of the wavefield for the geometry considered in this work. Shear waves are not directly generated in isotropic materials but do arise as a result of mode conversion at the boundary. This can be shown by considering the form of the source term as well as the solution for shear displacements in the unbounded medium (corresponding to v_{31} or $\tilde{v}_{31}$). The thermoelastic source has components including terms introduced after Eqs. (D.4) and (D.5):

$$\phi_2 = \theta(c_{2222}\alpha_{22} + c_{2233}\alpha_{33}) \text{ and } \phi_3 = \theta(c_{3322}\alpha_{22} + c_{3333}\alpha_{33}) . \tag{D.52}$$

For isotropic materials, all components of the thermal expansion tensor are equal ($\alpha_{22} = \alpha_{33}$) and the stiffness tensor reduces to two independent components from the five for transversely isotropic materials. First, $c_{2222} = c_{3333}$ (or $\alpha = \beta$) so that $\phi_2 = \phi_3$ – this simplifies the form of the source and the thermally-generated stresses are isotropic under these conditions. Secondly, the symmetry simplifies stiffness-related terms used to express $\tilde{v}_{31}$ including $c_{2323} = c_{1212}$ and $c_{2233} = c_{2222} - 2c_{1212}$ so that $\kappa = \alpha - 1$ and $\chi = 2\alpha$. With these equalities in place, according to Eq. (D.19), $\tilde{v}_{31} = 0$ – no transverse displacements are emitted by the source. This immediately eliminates three of the six components of the wavefield and the remaining terms are wholly related to longitudinal wave emission by the source.

D.4.3 Surface Expansion Line Source

One interesting limit is the case when $d \to 0$ which yields the displacement field for a surface source. Returning to the transform of the general solution given in Eq. (D.29) and letting $d = 0$ results in the following:

$$\tilde{v}_3^g\Big|_{d=0} = -(\alpha s z_{44})^{-1}\kappa k_2^2[\phi_3(1-\kappa)+\phi_2\alpha][be^{-k_{31}x_3} - ae^{-k_{33}x_3}](ad-bc)^{-1} . \tag{D.53}$$

Having obtained this solution for the displacements in the x_3 direction from a thermoelastic, surface line source, an alternative specification can be created by assessing the equivalent boundary stresses that give rise to these same displacements. Using Eq. (D.53) along with the associated displacements in the x_2 direction ($\tilde{v}_2^g\Big|_{d=0} = R_1\tilde{v}_{31}^g\Big|_{d=0} + R_3\tilde{v}_{33}^g\Big|_{d=0}$ – see Eq. (D.25)), the stresses can be written for the doubly transformed domain as follows:

$$\tilde{\sigma}_{33}\Big|_{d=0} = z_{44}\,[\alpha\tilde{v}_{3,3}^g + ik_2(\kappa-1)\tilde{v}_2^g]\Big|_{d=0} \tag{D.54}$$

$$\tilde{\sigma}_{23}\Big|_{d=0} = [\tilde{v}^g_{2,3} + ik_2\tilde{v}^g_3]\Big|_{d=0} \tag{D.55}$$

and evaluated at $x_3 = 0$ to yield:

$$\tilde{\sigma}_{33}\Big|_{\substack{d=0\\x_3=0}} = z_{44}(\kappa k_{31}k_{33})^{-1}[-a\tilde{v}^g_{31}\Big|_{\substack{d=0\\x_3=0}} - b\tilde{v}^g_{33}\Big|_{\substack{d=0\\x_3=0}}] = 0 \tag{D.56}$$

and

$$\tilde{\sigma}_{23}\Big|_{\substack{d=0\\x_3=0}} = z_{44}(-i\kappa k_2)^{-1}[c\tilde{v}^g_{31}\Big|_{\substack{d=0\\x_3=0}} + d\tilde{v}^g_{33}\Big|_{\substack{d=0\\x_3=0}}] = ik_2 s^{-1}[\phi_3(1-\kappa)/\alpha + \phi_2]\,. \tag{D.57}$$

These expressions can be inverted with respect to the remaining transform variables to arrive at the following equivalent boundary conditions:

$$\sigma_{33}\Big|_{\substack{d=0\\x_3=0}} = 0 \quad \text{and} \quad \sigma_{23}\Big|_{\substack{d=0\\x_3=0}} = [\phi_3(1-\kappa)/\alpha + \phi_2]\delta(x_2)_{,2}H(t)\,. \tag{D.58}$$

This result was derived previously by Hurley using the method of images [D.20]. By explicitly deriving solutions for the buried thermoelastic source using a general approach, the surface source is simply a special case that can be modeled more directly using equivalent boundary conditions.

D.4.4 Distribution of Subsurface Sources

Another interesting source specification that contrasts to the single source on the half-space surface is a distribution of subsurface sources that are all contained in the plane defined by the line direction and the surface normal – see Fig. D.4 for a schematic of the source configuration. This type of distributed source might occur in a variety of physical situations including those produced by subsurface photothermal conversion. If a total of N discrete sources are arrayed according to a distribution where the source amplitude as a function of the depth below the surface for the kth source is $f(d_k)$, then the total displacement, $v^g_{3_{Total}}(x_3)$, resulting from the superposition of these can be expressed as follows:

$$v^g_{3_{Total}}(x_3) = \sum_{k=0}^{N} f(d_k)v^g_3(x_3 - d_k)\,. \tag{D.59}$$

If these sources are arrayed in a regular fashion such that they are spaced at equal intervals below the surface (beginning at the surface), then $d_k = k\Delta d = k(d_{k+1} - d_k)$ and the total displacement can be computed according to Eq. (D.59). However, if $f(d_k)$ represents a continuous distribution function that is sampled at various locations, then the total displacement might be represented as follows:

$$v^g_{3_{Total}}(x_3) = [\sum_{k=0}^{N} f(d_k)v^g_3(x_3 - d_k)\Delta d][\sum_{k=0}^{N} f(d_k)\Delta d]^{-1} \tag{D.60}$$

where the denominator simply normalizes the computed displacement. The other factors do not change the result but are important if the distribution is exhaustively sampled – namely, as $\Delta d \to 0$ the following result emerges:

$$v^g_{3_{Total}}(x_3) = [\int_0^\infty f(y) v^g_3(x_3 - y) dy][\int_0^\infty f(y) dy]^{-1} \tag{D.61}$$

where the dummy variable, y, has been used to represent the source depth, d. Equation (D.61) is simply a convolution of the source distribution function with the displacement for the single line source normalized by the integrated source strength. Note that the original solution for the single line source located a distance d from the surface is recovered from Eq. (D.61) if the distribution is a Dirac delta function where $f(y) = \delta(y - d)$.

D.5. Discussion

The intent of this work has been to derive the elastic displacements that occur in a transversely isotropic half-space resulting from the action of a subsurface, thermoelastic line source perpendicular to the symmetry axis and parallel to the surface. Analytical, closed form solutions for these displacements have been derived for receiver locations directly below the line source – namely, those that are epicentrally located – and computed waveforms have been shown for titanium. While the various results presented in this work are instructive, their value is primarily in the application to specific problems that might arise in physical systems that display transverse isotropy but do not directly adhere to restrictions that have been placed on the results shown in this work. Some additional comments regarding the application of results in this work are required. First, the assumption that the receiver is buried in a half-space below the source is not typically encountered. Receivers are generally located on surfaces. To generate a source-receiver geometry similar to the one assumed in this work, the receiver would likely reside on the back surface of a plate structure and boundary conditions on this second surface would need to be included in the development [D28-30]. The displacements under these conditions can be developed from the results presented here by simply multiplying the various arrivals by the appropriate reflection coefficients – these are directly related to those already presented for reflection of the directly-emitted waves at the free surface. This treatment is consistent with ray descriptions of propagation in plates. Based on related treatments in isotropic materials, minor changes to the overall waveform shape are expected for reception on the back surface of a plate when compared to the buried receiver [D18].

The next issue relates to the computation of wavefields associated with distributed sources. While the line source permits the development of simple solutions, many physical circumstances give rise to distributed sources and methods for computation of the resulting displacements should be considered. The convolution integral given in Eq. (D.61) provides a formal solution for one type of distributed source, but it is unknown whether or not there exist continuous source distributions giving rise to simple solutions that do not require numerical evaluation. Numerical integration is likely required to obtain the displacements from most sources, and the question naturally arises regarding the best computational

approach to use. The convolution in Eq. (D.61) is one – this requires numerical evaluation of a single integral. However, the convolution could be carried out in the transform domain (before inversions were completed) and this could result in numerical evaluation of two, nested integrals. Indeed, under these conditions, a wider range of circumstances could be modeled since the temporal as well as the lateral spatial characteristics of the source might be incorporated into these integrals [D9]. However, care must be taken during the associated numerical integrations – it might be more computationally efficient to simply solve the governing differential equations numerically as has been done by others previously [D29]. While this approach does not take advantage of some elegant mathematics [D31], it does utilize the capabilities of contemporary computational techniques and could reveal behaviors that are not readily identified when analytical techniques are employed. Essentially, a wide range of circumstances involving changes to the source geometry and temporal profile might be modeled quite rapidly once solution algorithms are in place.

Finally, restrictions regarding the overall solution as it relates to the essential system geometry should be considered. The case developed in this work has the free surface as well as the source perpendicular to the symmetry axis. However, since the source is linear, dependence of displacements on one of the three spatial coordinates is suppressed – x_1 for the case here. The source geometry renders the overall problem one of two spatial dimensions and this also occurs when the line is oriented along principal axes in other directions. Solutions for these other source orientations can be derived directly from the results developed in this work. If the surface as well as the source are parallel to the symmetry axis, then the overall system behaves isotropically – appropriate changes to subscripts as well as substitutions for the various moduli can be made to generate the corresponding solution. The final expression for epicentral displacements is more compact than the one presented here since three terms directly associated with shear wave emission disappear and remaining terms simplify considerably. The final source geometry of interest occurs when the surface is parallel to the symmetry axis and the source is perpendicular to it. Under these conditions, the solution procedure shown here can be used in its entirety with a simple exchange of subscripts ($2 \rightleftarrows 3$) along with a re-definition of the normalized moduli. Under these conditions, the longitudinal wavespeed changes while the shear wave travels at the same speed as for the case considered in the original development.

D.6. Conclusions

Mathematical expressions for the material displacements resulting from a subsurface, thermoelastic line source in a transversely isotropic half space have been presented. These expressions showed that six discrete wave arrivals can be expected in the wavefield. In particular, closed-form, analytical solutions for displacements associated with the six arrivals were derived for a receiver located directly below the

source (in an epicentral location). Computed displacements in titanium showed large amplitude arrivals corresponding to longitudinal waves (directly transmitted and reflected from the surface) along with a smaller amplitude arrival associated with a shear wave produced by longitudinal wave conversion at the boundary. The directly transmitted longitudinal wavefront has a reciprocal, square root dependence on time as well as a reciprocal, square root dependence on the source-to-receiver distance – the temporal singularity at the longitudinal wavefront accounts for the large amplitudes in computed results. Shear waves have relatively small amplitudes for epicentral reception. In particular, the directly transmitted shear wave was shown to have a square root dependence on time yielding no singularity at the wavefront. The origin of this shear wave is directly related to the anisotropy of the system – it does not exist in isotropic systems. Computed results for titanium tend to indicate that the epicentral wavefront singularities for the direct and reflected longitudinal waves cancel one another in the limit as the source approaches the boundary leaving only higher order terms. This conclusion is supported by results for surface stresses that occur in the limit as the line moves to the boundary. In this limit, the source assumes the form of a surface, shear stress dipole with no contributions from the normal stress. Expressions have been developed for distributed sources that can be composed using superposition of subsurface line sources and it has also been shown that under appropriate conditions these expressions take on the form of a convolution between the source distribution function and the single line source solution developed in this work.

References

[D1] K Aki, PG Richards, Quantitative Seismology : Theory and Methods, W. H. Freeman, San Francisco, 1980.

[D2] T Royston, Y Yazicioglu, F Loth. Surface response of a viscoelastic medium to subsurface acoustic sources with application to medical diagnosis, J.Acoust.Soc.Am. 113 (2003) 1109-1121.

[D3] H Lamb. On the propagation of tremors over the surface of an elastic solid, Philosophical Transactions of the Royal Society of London Series a-Containing Papers of a Mathematical or Physical Character. 203 (1904) 1-42.

[D4] SK Bhandari, R Chander. On the exact evaluation of displacements within a semi-infinite solid due to a buried line source, Proceedings of the Indian Academy of Sciences-Earth and Planetary Sciences. 93 (1984) 37-45.

[D5] E Kausel. Lamb's problem at its simplest, Proceedings of the Royal Society A-Mathematical Physical and Engineering Sciences. 469 (2013).

[D6] DA Hutchins, RJ Dewhurst, SB Palmer. Directivity patterns of laser-generated ultrasound in aluminum, J.Acoust.Soc.Am. 70 (1981) 1362-1369.

[D7] JR Bernstein, JB Spicer. Line source representation for laser-generated ultrasound in aluminum, J.Acoust.Soc.Am. 107 (2000) 1352-1357.

[D8] D Royer. Mixed matrix formulation for the analysis of laser-generated acoustic waves by a thermoelastic line source, Ultrasonics. 39 (2001) 345-354.

[D9] I Arias, JD Achenbach. Thermoelastic generation of ultrasound by line-focused laser irradiation, Int.J.Solids Structures. 40 (2003) 6917-6935.

[D10] JD Achenbach. Laser excitation of surface wave motion, J.Mech.Phys.Solids. 51 (2003) 1885-1902.

[D11] WX Hu, ML Qian. Acoustic field excited by a pulsed laser line source in a cylinder, Ultrasonics. 44 (2006) E1187-E1190.

[D12] A Aharoni, K Jassby, M Tur. The Thermoelastic Surface Strip Source for Laser-Generated Ultrasound, J.Acoust.Soc.Am. 92 (1992) 3249-3258.

[D13] K Telschow, R Conant. Optical and Thermal Parameter Effects on Laser-Generated Ultrasound, J.Acoust.Soc.Am. 88 (1990) 1494-1502.

[D14] Y Guo, D Yang, Y Chang, W Gao. Effect of oblique force source induced by laser ablation on ultrasonic generation, Optics Express. 22 (2014) 166-176.

[D15] KF Graff. Wave Motion in Elastic Solids, Dover Publications, New York, 1991.

[D16] RG Payton. Elastic Wave Propagation in Transversely Isotropic Media, Martinus Nijhoff, The Hague, Netherlands, 1983.

[D17] RL Ryan. Pulse propagation in a transversely isotropic half-space, J.Sound Vibrat. 14 (1971) 511-&.

[D18] DH Hurley. An Investigation of the Anisotropic and Heterogeneous Nature of Laser Generated Ultrasound in Carbon-Fiber-Reinforced Epoxy and Single Crystal Materials, The Johns Hopkins University, Baltimore, Maryland, 1997.

[D19] DH Hurley, JB Spicer. Line source representation for laser-generated ultrasound in an elastic transversely isotropic half-space, J.Acoust.Soc.Am. 116 (2004) 2914-2922.

[D20] DH Hurley. Laser-generated thermoelastic acoustic: sources in anisotropic materials, J.Acoust.Soc.Am. 115 (2004) 2054-2058.

[D21] RG Payton. 2-dimensional anisotropic elastic waves emanating from a point source, Proceedings of the Cambridge Philosophical Society-Mathematical and Physical Sciences. 70 (1971) 191-&.

[D22] RG Payton. Epicenter and epicentral-axis motion of a transversely isotropic elastic half-space, SIAM J Appl Math. 40 (1981) 373-389.

[D23] RG Payton. Symmetry-axis elastic-waves for transversely isotropic media, Q Appl Math. 35 (1977) 63-73.

[D24] RG Payton. Plane strain displacement and stress waves induced in a transversely isotropic elastic solid by a line source, Zeitschrift Fur Angewandte Mathematik Und Physik. 29 (1978) 262-272.

[D25] EA Kraut. Advances in the theory of anisotropic elastic wave propagation, Rev.Geophys. 1 (1963) 401-448.

[D26] MJP Musgrave, RG Payton. Criteria for elastic-waves in anisotropic media - a consolidation, Journal of Elasticity. 14 (1984) 269-285.

[D27] RG Payton. Epicenter motion of a transversely isotropic elastic half-space due to a suddenly applied buried point source, Int.J.Eng.Sci. 17 (1979) 879-887.

[D28] B Xu, J Feng, G Xu, J Wang, H Sun, G Cao. Laser-generated thermoelastic acoustic sources and Lamb waves in anisotropic plates, Applied Physics A-Materials Science & Processing. 91 (2008) 173-179.

[D29] JJ Wang, BQ Xu, ZH Shen, XW Ni, J Lu. Numerical simulation of thermoelastic stress field and laser ultrasound in transversely isotropic plate, Japanese Journal of Applied Physics. 47 (2008) 956-963.

[D30] RL Weaver, W Sachse, KY Kim. Transient elastic waves in a transversely isotropic plate, Journal of Applied Mechanics-Transactions of the ASME. 63 (1996) 337-346.

[D31] A Rahman, F Ahmad. Representation of the displacement in terms of scalar functions for use in transversely isotropic materials, J.Acoust.Soc.Am. 104 (1998) 3675-3676.

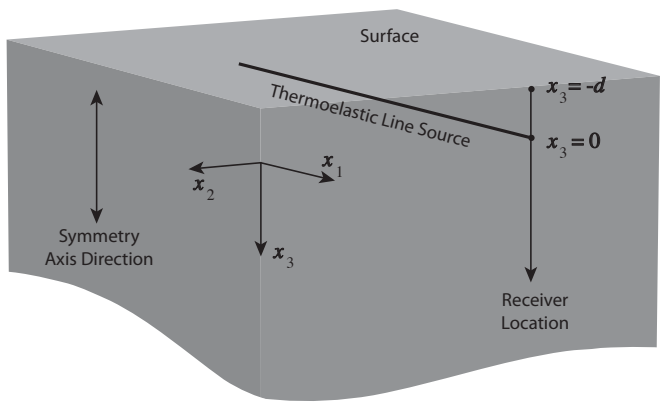

Figure D.1: Schematic illustration of the line source configuration modeled in this work. The source is perpendicular to the symmetry axis and parallel to the surface in a transversely isotropic material.

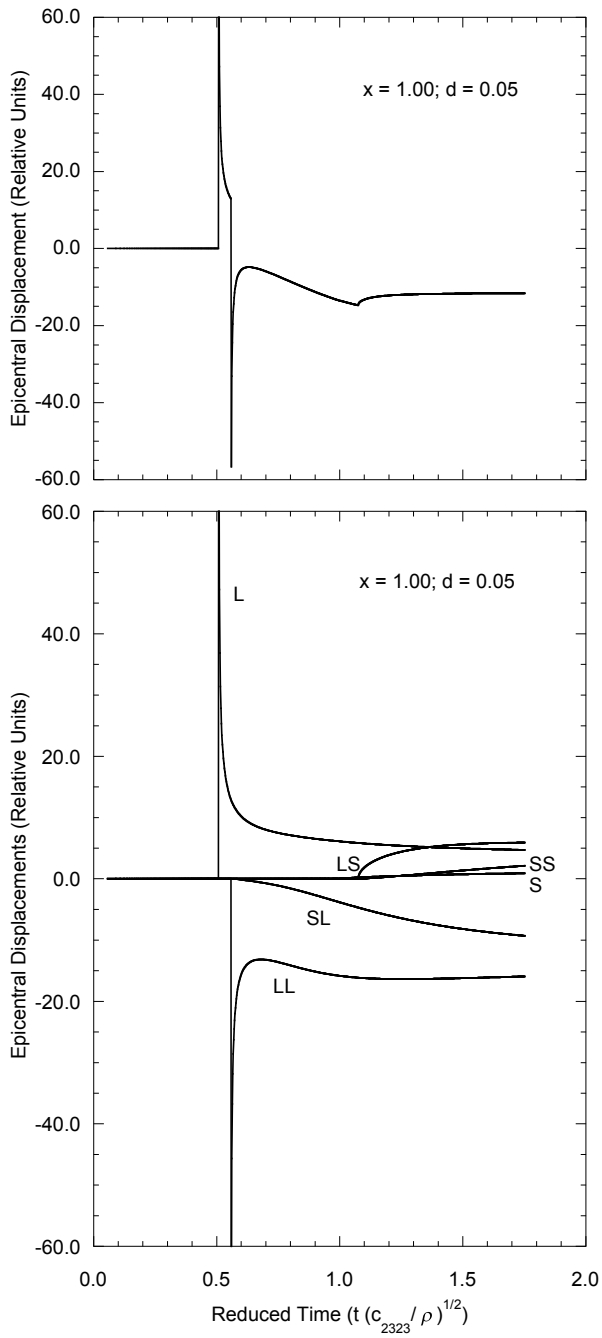

Figure D.2: (a) Epicentral displacements for a source located a distance $d = 0.05$ below the surface and a receiver located at $x_3 = 1$. The elastic constants and thermal expansion coefficient for titanium have been used. (b) The six components of the waveform shown in (a) where L is the direct longitudinal wave, LL is the reflected longitudinal wave, SL is the mode-converted shear-to-longitudinal wave, S is the direct shear wave, LS is the mode-converted longitudinal-to-shear wave and SS is the reflected shear wave.

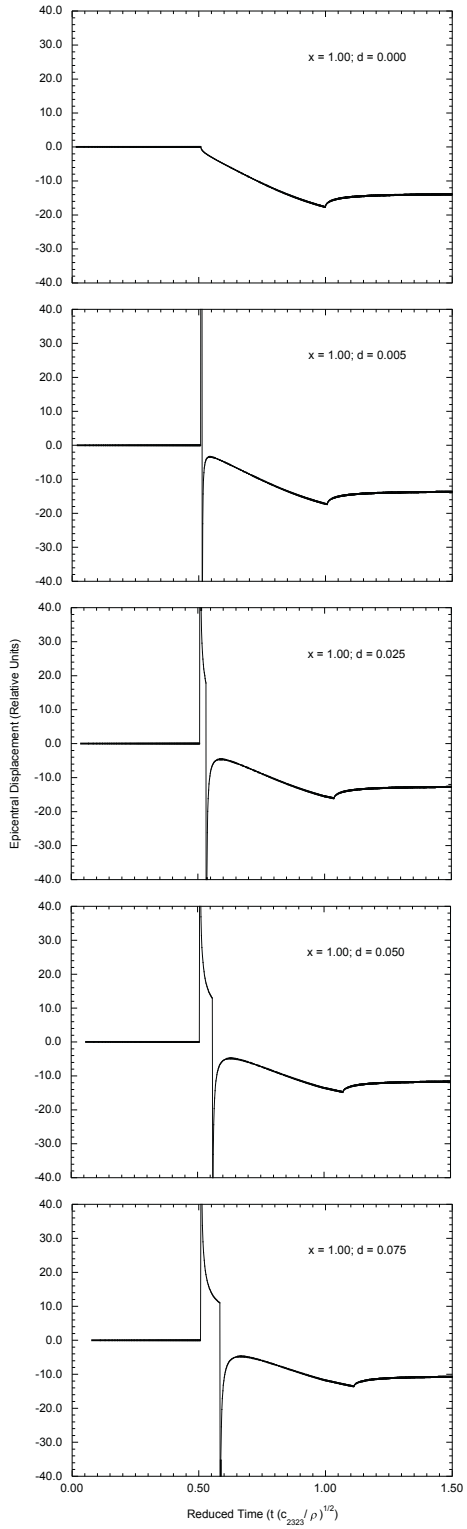

Figure D.3: Epicentral displacements in titanium for a receiver located at $x_3 = 1$ and a source located at the subsurface locations indicated next to each waveform. The direct and reflected longitudinal waves dominate the character of these waveforms when the source is subsurface ($d \neq 0$).

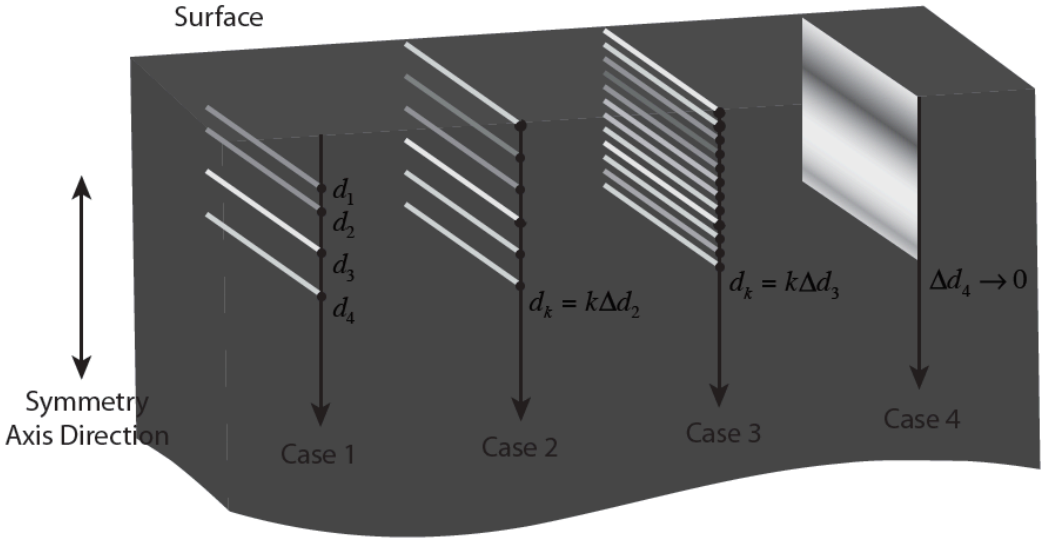

Figure D.4: Schematic illustration of source distributions that can be modeled using results presented in this work. Shading of sources indicates relative strengths. For collections of individual line sources as is shown for Cases 1-3, simple addition of waveforms can be used. In the limit of a continuous distribution as is shown in Case 4, convolution is required.

Section E: Theory and application of laser ultrasonic shear wave birefringence measurements to the determination of microstructure orientation in transversely isotropic, polycrystalline graphite materials

E.1. Introduction

Common materials used in a variety of engineering applications can be described as being polycrystalline. Namely, the material is composed of connected regions that share a common crystal structure and composition but differ in the crystallographic orientation relative to one another. Each of these regions can be referred to as a grain or crystallite. In many polycrystalline materials, crystallite orientations are nearly random and the material can behave isotropically if a statistically significant number of grains are involved in the physical process being investigated. Descriptions of materials behavior that include basic physical properties can be quite simple for isotropic materials and, for a large number of engineering materials, these types of descriptions are sufficient for most purposes. However, if the orientations of crystalline regions in the material are not random and there is some type of preferred orientation for the overall population then the material is said to have texture and will behave anisotropically. This is the case for various nuclear grade graphites produced using processing methods that result in preferred crystallite orientation. The anisotropy in these materials can have profound effects on their performance in nuclear reactors where they can serve as critical structural components [E1]. Consequently, significant effort has been invested in the measurement of anisotropy in nuclear graphites, but the results of these measurements have generally not been related quantitatively to the underlying texture of the material even though methods for doing so have been demonstrated previously [E2]. By contrast, the relationships between texture and material anisotropy in geological materials and metal alloys have been studied extensively [E3-7] since the trajectory of seismic waves as well as the behavior of rolled sheet during plastic forming both depend heavily on this anisotropy [E8,E9]. The most widely used methods for determination of texture in polycrystalline materials involve the use of x-ray diffraction (XRD). These methods generally provide information about the overall crystallographic orientation of material near the surface by interrogating many crystallites in this region and providing some average response related to the overall population [E10,E11]. Electron, backscatter diffraction (EBSD) is another method that has been used [E12]. Owing to the high spatial resolutions that can be achieved using electron microscopy techniques, orientation maps for individual crystallites at the material surface can be created using EBSD. Statistical analysis of these maps can be performed and results related to those obtained using XRD methods. Neutron diffraction has also been used and can provide information not available using either XRD or EBSD techniques since neutrons penetrate through the bulk of a sample and can provide volumetric texture information [E3,E5].

The material that is the focus of the work presented here is nuclear graphite – a chemically pure form of polycrystalline graphite that has properties favorable for use in nuclear reactors. In polycrystalline graphite, anisotropy can arise not only from the texture – as occurs in other polycrystalline materials such as ceramics and metals – but also from the preferred orientation of microstructural defects. Alignment of non-spherical pores as well as microcracks can influence properties that depend directly on the geometries and population densities for these defects. While the measurement of crystallite orientation can be accomplished using diffraction-based techniques, the orientation of defect structures can be more difficult to determine directly especially if whole populations must be characterized. Since these structures can strongly influence the physical properties of the overall material [E13], measurement of the anisotropy of bulk properties can provide insight into the preferred orientation of defect structures in the material.

The use of physical properties measurements to characterize anisotropy and infer texture has been used extensively. In particular, the elastic moduli of polycrystalline materials can be readily assessed using ultrasonic methods and these can be directly related to the underlying materials microstructure [E4,E6,E7,E12,E14-17]. If the material anisotropy is dominated by orientation of crystalline regions, then some useful comparisons can be made between diffraction-based measurements and those obtained using ultrasonic techniques [E5,E12]. In some sense, these comparisons are tests of structure-property relationships since diffraction techniques provide information directly related to preferred orientation while ultrasonics essentially provides modulus-related information. Results of studies that have considered both generally indicate that there is agreement between diffraction and properties results so long as the differences between the measurement techniques are taken into account [E18].

For the work reported here, ultrasonic methods have been used to characterize a transversely-isotropic, polycrystalline graphite and measurements have been interpreted within an overall framework that allows for comparison to other physical property measurements. Ultrasound is sensitive to both texture as well as to the presence and orientation of defect structures and, as a result, ultrasonic measurements indicate the combined effects of these on the material moduli. In particular, the technique of shear wave birefringence using laser ultrasonic methods has been used since it minimizes the effects of material inhomogeneity on measured results while effectively capturing and isolating material anisotropy. These ultrasonic measurements provide information that can be interpreted using simple models describing the elastic moduli of polycrystalline materials. In this work, we show how standard physical property descriptions representing the behaviors of single crystal materials (with and without defects) can be combined with a representation of texture (based on the orientation distribution function) to permit development of simple descriptions for the average properties associated with textured, polycrystalline graphite.

E.2. Physical Properties of Textured Polycrystalline Materials

E.2.1 General Background

Texture in polycrystalline materials generally arises from the techniques that are used during material processing. Rolling, extrusion as well as molding operations can cause slight re-orientation and increased alignment of crystalline regions driven by stresses experienced by the material during the forming process [E10]. Since single crystal materials are anisotropic, any texture associated with polycrystalline materials will have physical properties that reflect not only the texture but depend directly on the properties of underlying crystal structure of the constituent crystallites. This implies that polycrystalline materials displaying texture do not behave isotropically and, as a result, more involved descriptions than are used for isotropic materials are required to adequately characterize their behaviors. These descriptions must involve the physical properties of the single crystal material and must also include methods for accounting for the overall behavior of the polycrystalline ensemble. In this work, we will focus on the elastic responses and the thermal expansion characteristics, but the overall method used here has been generalized to other material behaviors that can be described using physical property methods. In the following sections, notation conventions vary and have been chosen to effectively convey the major ideas being described. In some cases, notation directly reflects the underlying computation being performed while at other times the notation represents the essential ideas being developed. A uniform notation could have been used for all sections, but would be at the expense of overall clarity. The compromise used here facilitates the presentation while providing essential details that support the overall results of the work.

E.2.2. Physical Properties of Single Crystals and Polycrystalline Materials

The elastic and thermal expansion behaviors of single crystal materials are well-defined using physical property descriptions. Generally, these behaviors are coupled (differences between the isothermal and adiabatic elastic moduli depend on the thermal expansion) and can also occur simultaneously (stress-induced deformations can combine with those produced by changes in temperature). It will be assumed that all behaviors are linear with respect to field variables – stress varies linearly with strain for elastic behavior and strain varies linearly with temperature changes for thermal expansion. This assumption greatly simplifies descriptions of the corresponding physical properties and these can be found in various reference texts [E19,E20].

Unlike single crystal materials, the bulk material properties of a polycrystalline material depend not only on the single crystal properties but also on the relative orientations of individual crystallites that compose the material. Stated differently, the properties of the polycrystalline must somehow reflect the crystalline properties of the constituent material as well as the symmetries of the polycrystalline ensemble. The simplest approach to deriving properties of the aggregate is to compute a directionally-weighted average

that incorporates the fractional volume occupied by crystallites of a given orientation along with the value of the property in a particular direction referred to a coordinate system [E10]. While this description is conceptually straightforward, another equivalent method for deriving the properties of the polycrystalline material is to employ the orientation distribution function, $f(\boldsymbol{g})$. This scalar function describes the fraction of material in the representative volume of a given orientation, $\boldsymbol{g}$. The orientation can be provided by an ordered set, (ψ,θ,ϕ), corresponding to the symmetric Euler angles. Using $\boldsymbol{g}=(\psi,\theta,\phi)$, the orientation distribution function can be expressed as a series expansion using the generalized spherical harmonic functions as follows:

$$f(\psi,\theta,\phi)=\sum_{l=0}^{L_0'}\sum_{m=-l}^{l}\sum_{n=-l}^{l}W_{lmn}Z_{lmn}(\cos\theta)e^{im\psi}e^{in\phi} \tag{E.1}$$

where W_{lmn} are the orientation distribution coefficients and Z_{lmn} are the Jacobi Polynomials. Similarly, the components of the tensor, $\boldsymbol{t}$,can be expressed in the sample frame of reference such that

$$\boldsymbol{t}(\psi,\theta,\phi)=\sum_{l=0}^{L_0''}\sum_{m=-l}^{l}\sum_{n=-l}^{l}\boldsymbol{t}_{lmn}Z_{lmn}(\cos\theta)e^{im\psi}e^{in\phi} \tag{E.2}$$

where $\boldsymbol{t}_{lmn}$ represent the tensor coefficients for the various components in the sample frame of reference. Using the expressions given in Eqs. (E.1) and (E.2) along with the following representation for the average value for of the tensor property, $\overline{\boldsymbol{t}}$:

$$\overline{\boldsymbol{t}}=\int \boldsymbol{t}(\boldsymbol{g})f(\boldsymbol{g})d\boldsymbol{g}\,. \tag{E.3}$$

and noting the orthonormal properties of the generalized spherical harmonics yields the following:

$$\overline{\boldsymbol{t}}=4\pi^2\sum_{l=0}^{L_0}\sum_{m=-l}^{l}\sum_{n=-l}^{l}\boldsymbol{t}_{lmn}W_{lmn} \tag{E.4}$$

where L_0 takes on the lower value of either L_0' or L_0'' [E10]. This result indicates that the property in the sample frame of reference depends only on the orientation distribution coefficients and the coefficients for the tensor corresponding to the single crystal property. Generally, the higher the point group symmetry of the crystal system for the constituent crystallites or the higher the symmetry of the distribution function or the lower the rank of the tensor property, the lower the number of orientation distribution coefficients that are needed to describe the average property in the polycrystalline material. For the purposes of this work in which we will consider transversely isotropic materials composed of graphite crystallites having hexagonal point group symmetry, only two orientation distribution

coefficients are required to describe the average elastic modulus tensor while thermal expansion can be described using a single orientation distribution coefficient.

E.2.3. Models for Elastic Response and Thermal Expansion in Polycrystalline Systems

E.2.3.1. Elastic Response

For textured polycrystalline materials, the constitutive relation for linear elastic response can be expressed as follows:

$$\sigma_{ij} = \overline{c}_{ijkl}\varepsilon_{kl} \tag{E.5}$$

where σ_{ij} is the elastic stress tensor, ε_{kl} is the infinitessimal strain tensor and $\overline{c}_{ijkl}$ is the effective, linear elastic, stiffness tensor. Self-consistent methods are needed to accurately estimate the effective moduli [E8], but these methods will not be pursued here. Upper and lower bounds can be obtained by assuming uniform stress or strain conditions which yield the Reuss and Voigt limits for the polycrystalline moduli, respectively. These limits can be computed readily and yield compact forms that can be written directly. Early publications by Morris [E22,E23] as well as by Sayers [E24,E25] are useful in constructing these expressions. Following work by Li and Thompson [E26], the components of the elastic modulus tensor that relate to the shear birefringence measurements in this work can be expressed as follows:

$$\overline{c}_{11}^{I} = c_{11}^{I^0} + 4\pi^2[4(10^{1/2}/210)A_1^I W_{200} + 3(2^{1/2}/105)B^I W_{400}] \tag{E.6}$$

$$\overline{c}_{44}^{I} = c_{44}^{I^0} + 4\pi^2[(10^{1/2}/210)A_3^I W_{200} - 4(2^{1/2}/105)B^I W_{400}] \tag{E.7}$$

$$\overline{c}_{66}^{I} = c_{44}^{I^0} + 4\pi^2[-(10^{1/2}/105)A_3^I W_{200} + (2^{1/2}/105)B^I W_{400}] \tag{E.8}$$

where $I = R$ or V depending on whether the Reuss or Voigt values are needed. In these expressions, Voigt two-index notation has been used instead of tensor notation since this decreases the length of various expressions. Also, expressions for A_1^I, A_3^I and B^I are provided in Appendix A. According to Eqs. (E.6)-(E.8), the polycrystalline moduli depend only on the single crystal elastic constants and the orientation distribution coefficients W_{200} and W_{400}.

E.2.3.2. Thermal Expansion

Strains, ε_{ij}, associated with a temperature rise, θ, in a textured, polycrystalline material can be expressed as follows:

$$\varepsilon_{ij} = \overline{\alpha}_{ij}^{I}\theta \tag{E.9}$$

where $\bar{\alpha}_{ij}^{I}$ represents the thermal expansion coefficient tensor for the material and $I = R$ or V depending on whether Reuss or Voigt averaging methods are used. Again, estimates for components of the effective thermal expansion tensor should be obtained using methods that have been described elsewhere, but the upper and lower bounds based on the Reuss and Voigt averaging schemes can be expressed quite simply using algebraic expressions.

Following work by Dunn and Ledbetter [E27], the thermal expansion coefficients for a transversely isotropic, polycrystalline material using the Reuss averaging process yields:

$$\bar{\alpha}_1^R = (2\alpha_1 + \alpha_3)/3 - [4(2/5)^{1/2}\pi^2(\alpha_3 - \alpha_1)/3]W_{200} \tag{E.10}$$

and

$$\bar{\alpha}_3^R = (2\alpha_1 + \alpha_3)/3 + [8(2/5)^{1/2}\pi^2(\alpha_3 - \alpha_1)/3]W_{200} \tag{E.11}$$

which are the principal components of the thermal expansion tensor. Note that these expressions are fairly simple and indicate that thermal expansion in the polycrystalline system depends solely on the single crystal thermal expansion coefficients and the orientation distribution coefficient W_{200}.

Once again, following work by Dunn and Ledbetter [E27], the corresponding results for the thermal expansion coefficients using the Voigt averaging method yields:

$$\bar{\alpha}_1^V = (2\alpha_1 + \alpha_3)/3 + 2(\alpha_1 - \alpha_3)\gamma/3 - \eta W_{200} \tag{E.12}$$

and

$$\bar{\alpha}_3^V = (2\alpha_1 + \alpha_3)/3 + 2(\alpha_1 - \alpha_3)\gamma/3 - \kappa W_{200} \tag{E.13}$$

where expressions for γ, η and κ are provided in Appendix B. Even though these results for the thermal expansion coefficients contain many more terms than those obtained for Reuss averaging, the polycrystalline thermal expansion coefficients still depend solely on the orientation distribution coefficient W_{200} and on the single crystal values for the thermal expansion coefficient and, in this case, the elastic moduli.

E.2.3.3. Modified Hill Approximation

As has been mentioned, the Voigt and Reuss averages for both the elastic moduli and the thermal expansion coefficients represent bounds that might or might not accurately reflect the actual values obtained in polycrystalline materials. For many materials systems, a first estimate beyond these bounds that might be considered is the Hill approximation – the simple average of the Voigt and Reuss values. While the Hill approximation might reasonably hold under many circumstances, it is not clear why this estimate should be preferred to others especially in polycrystalline graphites since the Voigt and Reuss

limits differ significantly from one another. For the purposes of this work, a modified Hill approximation will be used where a weighted average of the Voigt and Reuss limits will be used instead of a simple average. For the elastic moduli we will use

$$\overline{c}_{ij} = r\overline{c}_{ij}^{R} + (1-r)\overline{c}_{ij}^{V} \tag{E.14}$$

and for the thermal expansion coefficients

$$\overline{\alpha}_{i} = r\overline{\alpha}_{i}^{R} + (1-r)\overline{\alpha}_{i}^{V} \tag{E.15}$$

where, in both of these expressions, r is the fractional contribution of the Reuss estimate to the overall property and $0 \le r \le 1$.

E.2.3.4. Determination of Orientation Distribution Coefficients

First, consider the elastic properties of the material. In this work, we will present shear birefringence measurements that provide values for $\overline{c}_{11}$, $\overline{c}_{44}$ and $\overline{c}_{66}$. The essential unknowns in the corresponding models for these moduli are r and the orientation distribution coefficients W_{200} and W_{400}. Equations (E.6)-(E.8) and (E.14) can be solved for either W_{200} or W_{400} – related quadratic equations and the solution process used in this work are given in Appendix C. Even though the solution for either orientation distribution coefficient can be expressed in a finite, closed form, it is lengthy and will not be given here. The important result is that our measurements provide sufficient information to uniquely solve for the underlying descriptors of the system. Similarly, when thermal expansion is considered, if values for the two components of the corresponding tensor are measured, then r and W_{200} can be determined using the models presented here. A quadratic equation for W_{200} results (also given in Appendix C), but its solution is too lengthy to be shown here.

E.3. Elastic and Thermal Expansion Properties of Single Crystal Graphite Containing Microcracks

During processing of bulk, nuclear graphite materials, microcracks and oriented pores are introduced into the microstructure of the material. These defects are known to affect various behaviors in graphite including the elastic response of the material [E28,E29], and related effects need to be considered for interpretation of experimental results obtained in this work. There are various approaches to modeling the effects of microcracks on the elastic properties of polycrystalline materials [E30-33] especially those containing high crack densities [E34] that could account for the effects of microcracks on the elastic moduli of polycrystalline graphite. However, we will choose to modify the single crystal elastic constants to incorporate the effects of microcracks since it is known that these types of defects readily form along planes perpendicular to the axis of symmetry (c-axis) in graphite. This particular approach approximates conditions that hold in nuclear graphite.

E.3.1. Single Crystal Elastic Constants – Effect of Oriented Microcracks

Fortunately, the elastic moduli for hexagonal, single crystal materials containing microcracks perpendicular to the c-axis have been modeled by Schoenberg and Douma [E35]. The results they obtained are presented here as follows:

$$c'_{33} = c_{33}(1+E_N)^{-1},\ c'_{11} = c_{11} - c_{13}^2[1-(1+E_N)^{-1}]/c_{33},\ c'_{44} = c_{44}(1+E_T)^{-1},$$

$$c'_{66} = c_{66},\ c'_{13} = c_{13}(1+E_N)^{-1},\ c'_{12} = c'_{11} - 2c_{66} \tag{E.16}$$

where the prime indicates the stiffness tensor component has been modified by the presence of microcracks, $E_N = c_{33}Z_N$ and $E_T = c_{44}Z_T$. Here Z_N and Z_T represent the normal and tangential compliances of an average crack. If the uncracked material is isotropic, these expressions are in general agreement with Zheng under certain conditions [E36]. For the purposes of this work, it will be assumed that $Z_N \approx Z_T$ since Schoenberg and Sayers indicate that this is true for various types of materials [E37]. For analysis of experimental results, these microcrack-modified, single crystal elastic constants will be used with all previous models for the elastic properties of textured, polycrystalline materials.

3.2. Thermal Expansion – Effect of Oriented Microcracks

Owing to differences between Voigt and Reuss averaging, the effect of microcracks on thermal expansion in polycrystalline materials can manifest itself directly through the thermal expansion coefficients or indirectly through the elastic moduli. According to Eqs. (E.12) and (E.13), the Voigt values for components of the thermal expansion tensor depend directly on the single crystal values for elastic moduli owing to elastic constraint effects. Since these are modified by microcracks, it is clear that the thermal expansion of the polycrystalline material will be affected by microcracking even if the single crystal thermal expansion coefficients are not. For the purposes of this work, it will be assumed that the single crystal values for components of the thermal expansion are not directly affected by pores or microcracks since the influence of these microstructural elements on thermal expansion occurs primarily when elastic constraint occurs in polycrystalline systems. This overall approach to interpreting the influence of microstructure on thermal expansion is consistent with work on thermal expansion in a range of materials systems [E38-42] and agrees with early work on nuclear graphites by Sutton and Howard [E43] and by Jenkins [E44].

E.4. Experimental: Materials and Methods

Using laser ultrasonic line source techniques, shear birefringence measurements were made on NBG-25 – a leading candidate as a structural material produced by SGL Carbon for core support in the next generation nuclear reactors [E45]. Reports indicate that NBG-25 is an isostatically-molded, superfine-

grained (<50 μm) graphite produced using petroleum-derived coke [E45,E46]. Preliminary ultrasonic evaluation of this material indicated that it was transversely isotropic. Two ultrasonic samples of NBG-25 having dimensions approximately 50 mm by 50 mm by 6 mm were cut from a larger sample block. These two samples will be referred to as NBG-25-1 and NBG-25-2. The orientations of these samples were chosen so that the directions of ultrasound propagation (along the 6 mm thickness direction) would be perpendicular to one another in the frame of reference of the original block. One square surface of each sample was prepared using silicon carbide grinding paper; the other square surface was polished to a mirror-like finish using 1 μm diamond paste so that the optical reflectivity was sufficient for ultrasound detection using optical interferometry. Using simple measurements of sample dimensions and mass, the bulk density of the NBG-25 was measured to be 1.85 g/cm^3. It should be noted that the measured volume includes both open and closed pores and this is appropriate for determination of modulus since ultrasound does not distinguish between the two.

Aspects of the graphite microstructure are shown in Fig. E.1 where micrographs of the polished sample surface are shown. The image in Fig. E.1a was acquired using polarized light microscopy and highlights polarization rotation that occurs as a result of light reflection from the sample surface. Crystalline regions of the microstructure that are not aligned with the surface normal will rotate the polarization and produce intensity variations in the acquired image. This type of imaging can quickly provide a qualitative sense of the orientation of crystalline regions in the graphite. A scanning electron microscope (SEM) micrograph of NBG-25 is shown in Fig. E.1b. Image analysis of the polished graphite surface can reveal detail about graphite structure including size, shape, and distribution of pores. Unlike pores, cracks and microcracks are difficult to identify in the SEM images. However, Mrozowski microcracks and other microstructural crack-like features have been observed in nuclear graphites previously using TEM methods [E47-50] and these studies have shown that microcracks generally occur between graphitic planes along the crystal c-

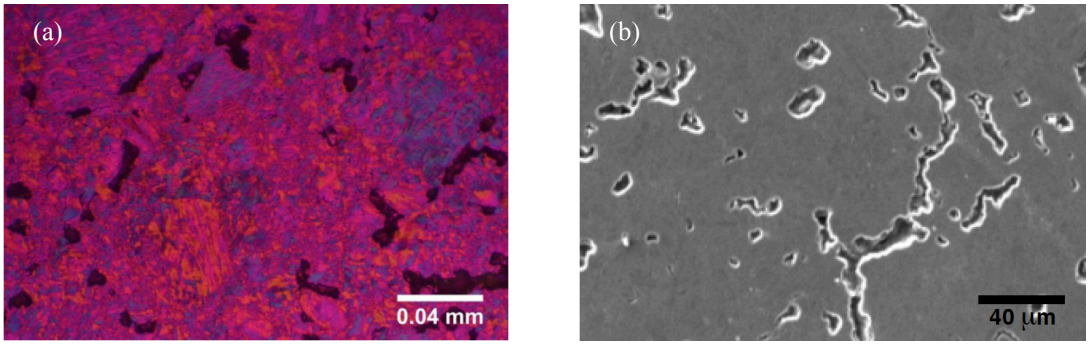

Figure E.1. Micrographs of NBG-25 used in this study. (a) Photomicrograph obtained using polarized light microscopy highlighting regions of varying crystallographic orientation. Black regions are pores. (b) SEM micrograph highlighting pore structure in the graphite.

axis.

A schematic of the laser ultrasonic system used to measure shear wave birefringence in these samples is shown in Fig. E.2. The output of a Q-switched Nd:YAG laser (pulse duration approximately 10 ns) was formed into a line using beam-shaping optics and the pulse energy was adjusted to minimize material removal by ablation. Under these conditions, the laser line source served as a thermoelastic, ultrasonic transmitter that emitted both shear waves as well as longitudinal waves. A Michelson-type, path-stabilized interferometer, located directly opposite the line source in the epicentral position, was used as a receiver. Its effective operating bandwidth was approximately 20 kHz to 50 MHz. Owing to the line-like character of the source, it produced shear waves with specific polarization perpendicular to the line direction for components of the displacement field transmitted through the sample thickness. Only shear modes with displacement perpendicular to the laser line are produced since displacements along the line direction are suppressed owing to the symmetry of the source [E51]. Figure E.3 shows a schematic drawing of the measurement configuration where the shear wave propagation direction was fixed while the shear polarization was varied by rotating the orientation of the line source. Time-of-flight measurements were made as a function of the line orientation to assess wavespeed variations as a function of wave polarization. Any wavespeed variations related to polarization direction can be linked primarily to material anisotropy since shear waves propagate through a fixed volume of material between the source and the receiver. This volume is essentially defined by the receiver spot size on the sample surface (less than 100 μm for the work here) as well as the width of the line source (approximately 100 μm). Even though ultrasound arrives at the receiver location from all positions along the line (and encompasses a relatively large volume of material), only wavefront arrivals at the receiver are recorded and these correspond to portions of the ultrasonic field that travel the shortest distances between the line source and the receiver. The lateral resolution provided by the dimensions of the receiver and source permit

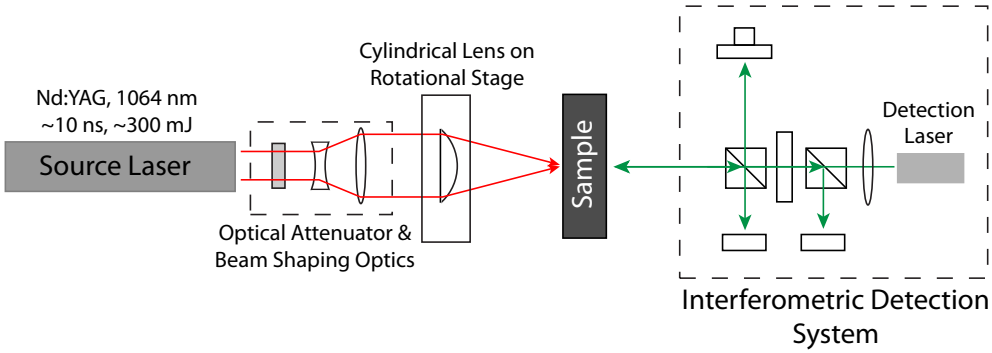

Figure E.2. Schematic of the laser ultrasonic system used to measure shear wave birefringence in graphite. The orientation of the laser line source was changed by mounting the cylindrical lens in a rotational stage.

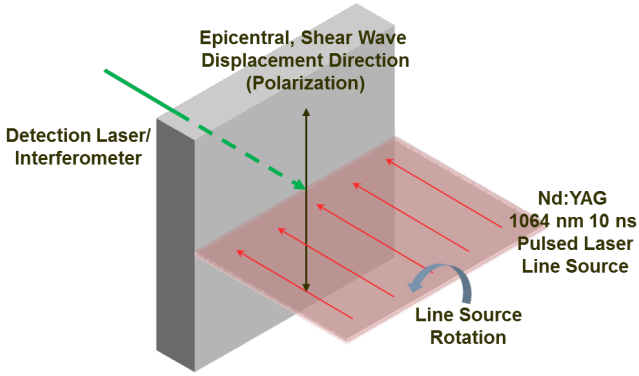

Figure E.3. Schematic of the measurement geometry used to gather ultrasonic waveforms highlighting the shear wave polarization relative to the line source direction.

interrogation of the material on length scales below those typically obtained using traditional ultrasonic techniques. By scanning the source and receiver relative to the sample, variations related to inhomogeneity can be mapped. However, the influence of inhomogeneity on shear wave birefringence measurements is considerably lower than effects attributable to elastic anisotropy since the volume of material interrogated during the ultrasonic measurements is, for the most part, unchanged when signals are recorded for various line orientations. In this work, measurements were made with line orientations of 0° and 90° relative to one sample edge. The different line source and sample orientations for the two samples are shown in Fig. E.4.

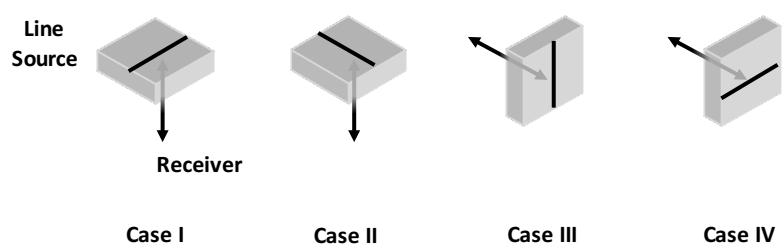

Figure E.4. Illustrations showing relative orientations of the laser line source and the ultrasonic receiver used for assessment of shear birefringence.

E.5. Results and Discussion

Representative laser ultrasonic waveforms are shown in Fig. E.5. In general, the ultrasonic signals from NBG-25-1 have better signal-to-noise characteristics than those from NBG-25-2. Nonetheless, the ultrasonic arrivals for the directly transmitted longitudinal and shear waves are easily identified, and the four different waveforms clearly show the effects of polarization and propagation direction on ultrasonic wavespeeds. These waveforms can be compared to results of modeling studies focused on laser line sources in transversely isotropic systems to assist in the interpretation of arrival times as a function of propagation direction and polarization [E52].

In order to assign the recorded waveforms in Fig. E.5 to the corresponding measurement geometries depicted in Fig. E.4, a few observations regarding expected behaviors in relation to measured results are needed. First, for a transversely isotropic material in which the axis of symmetry is parallel to the direction of ultrasonic propagation, the line source orientation and the corresponding wave polarizations

do not affect the ultrasonic wavespeeds. If Cases I and II correspond to this condition, then the orientation of the line source will not affect the measurement. Results obtained in sample NBG-25-1 appear to approximate this condition. In contrast, if Cases III and IV correspond to propagation perpendicular to the axis of symmetry then the line source orientation will affect the shear wavespeeds leading to shear wave birefringence [E52]. This condition appears to be true for the sample NBG-25-2 since the times-of-flight for the shear wave arrivals in this sample differ (indicated by Δt_{Shear} in Fig. E.5).

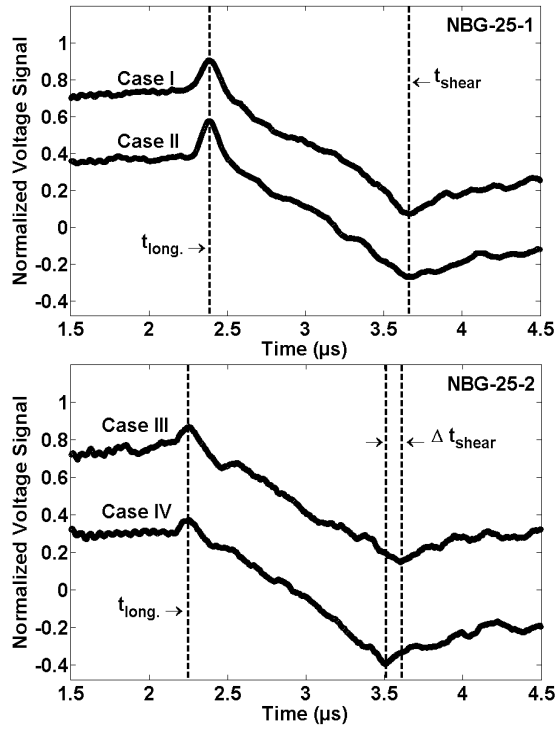

Figure E.5. Laser ultrasonic results obtained on two samples of NBG-25 corresponding to the Cases shown in Fig. 4. The sample designated as NBG-25-2 displays shear wave birefringence which is indicated by the difference in shear wave arrival times. Waveforms are shown offset for clarity.

These results indicate that NBG-25 could possess symmetries characteristic of a transversely isotropic material. Even so, the limited measurements provided here do not necessarily capture the overall extremes of the elastic anisotropy in this material, and this raises the possibility that the sample reference frames are not necessarily aligned with the material frame of reference. This could be important in a complete assessment of material anisotropy in this system. For the purposes of this work, it will be assumed that results on NBG-25-2 correspond to propagation perpendicular to an axis of symmetry. This is important for analysis of ultrasonic signals and also permits comparison to thermal expansion results presented in the literature for NBG-25.

The models presented for the elastic moduli of transversely isotropic, polycrystalline materials with preferred grain orientation indicate that the components of the elastic stiffness tensor for the bulk material can be expressed using effective isotropic moduli along with perturbations that include the orientation distribution coefficients, W_{200} and W_{400} [E26]. These effective isotropic moduli consist of suitable averages of the single crystal modulus values from the stiffness tensor. Based on these models, the ultrasonic waveforms gathered in the orientations represented by Cases III and IV can be used to compute

moduli (following procedures outlined in Appendix D) that relate to W_{200} and W_{400}. Similarly, it was shown that the thermal expansion coefficients for polycrystalline materials with preferred grain orientation displaying transverse isotropy can be described using effective isotropic coefficients that are suitably modified by terms that depend on the orientation distribution coefficient W_{200} [E27]. Measurements of thermal expansion along and perpendicular to the axis of symmetry are sufficient to infer W_{200} given that the components of the single crystal thermal expansion coefficient tensor as well as the elastic compliances are known. Even though thermal expansion measurements were not performed on the samples used in this study, results from the literature for NBG-25 can be used.

For a transversely isotropic material, the elastic moduli that can be extracted from the laser ultrasonic measurements indicated for Cases III and IV correspond to $\bar{c}_{11}$, $\bar{c}_{44}$ and $\bar{c}_{66}$ [E52] which were 12.5, 4.84 and 5.13 GPa respectively for the NBG-25 used in this work. Interpreting these results within the framework of a textured, polycrystalline material using microcrack-modified values for the components of the single crystal stiffness tensor along with a modified Hill averaging approach yields values of $W_{200} = 0.00196$ and $W_{400} = -0.000757$ for the orientation distribution coefficients. These results were obtained using the following microcrack-modified stiffnesses (all in GPa): $c'_{11} = 1053.79$, $c'_{33} = 1.07$, $c'_{44} = 0.857$, $c'_{12} = 173.79$ and $c'_{13} = 0.447$ (corresponding to a microcrack compliance of $Z_N \approx Z_T = Z = 0.5$). These should be compared to the following accepted values for microcrack-free, single crystal graphite (again in GPa) $c_{11} = 1060$, $c_{33} = 36.5$, $c_{44} = 4$, $c_{12} = 180$ and $c_{13} = 15$. Essentially, elastic constants that depend heavily on microcracks oriented along graphitic planes are significantly modified while others are not altered to any great degree. In addition, a value of $r = 0.984$ was produced for the modified Hill averaging scheme indicating that the measured modulus values were close to those associated with the Reuss bound – the lower limit – and this quantitative result is consistent with observations made previously in various graphites [E53,E54].

Published measurements of the thermal expansion in NBG-25 provide the following values for the components of the thermal expansion coefficient tensor: $\bar{\alpha}_1 = 3.5 \times 10^{-6}\ {}^{\circ}\mathrm{C}^{-1}$ and $\bar{\alpha}_3 = 4.2 \times 10^{-6}\ {}^{\circ}\mathrm{C}^{-1}$ [E55-57]. To interpret these values with the framework for a textured, polycrystalline material, the same microcrack-modified values for the single crystal elastic constants (and the corresponding compliances) were used along with the thermal expansion coefficients for single crystal graphite ($\alpha_1 = -1.2 \times 10^{-6}\ {}^{\circ}\mathrm{C}^{-1}$ and $\alpha_3 = 14 \times 10^{-6}\ {}^{\circ}\mathrm{C}^{-1}$) [E58-63]. Again, the modified Hill averaging approach was used to model the polycrystalline material yielding the orientation distribution coefficient $W_{200} = 0.0019$ along with $r = 0.973$. Since the orientation distribution coefficients are purely

geometrical descriptors of polycrystalline materials, they are independent of the measurement process used to infer them and it should be expected that a value for W_{200} based on measurements of elastic anisotropy should agree with one derived from thermal expansion measurements. Similarly, since the distribution of stresses and strains that occurs among adjoining grains in a material should depend primarily on the relative orientations and stiffnesses of the grains and should not differentiate between mechanically-induced or thermally-induced deformations, it should be expected that the fractional contribution of the Reuss and Voigt values to the modified Hill average for the two properties should be the same.

Even so, the agreement of the results for W_{200} and r obtained using ultrasound measurements with those determined using thermal expansion results is remarkable and might appear to be fortuitous. However, the ~ 3% difference between the values for W_{200} and the ~ 1% difference for the values for r are tied to direct connections between the elastic moduli and thermal expansion that occur in polycrystalline, anisotropic materials since both depend on the single crystal stiffness components [E27,E63] – the microcrack-modified values in this case. Examination of the expression for these given in Eq. (E.16) shows that the moduli depend on the normal and tangential compliances of an average microcrack (Z_N and Z_T respectively) where, in this work, these compliances have been assumed to be equal. Essentially, the microcrack compliance becomes an additional parameter that can be varied. While Shoenberg and Douma [E35] refer to Z_N and Z_T as being microcrack compliances, both can be directly related to microcrack densities [E36], and, as a result, the role of this additional parameter becomes clear – it reflects the defect content of the graphite. This suggests that changes to $Z_N \approx Z_T = Z$ could directly relate to changes in the defect content (microcrack density) in the material.

It is possible to use diffraction-based measurements to directly measure orientation distribution coefficients [E10,E43]. Based on the models developed here, these measurements could be combined with either the elastic or the thermal expansion measurements to derive values for the remaining parameters – including the microcrack density. Doing so presents interesting opportunities for in-service monitoring of graphite integrity. Initial evaluation of the orientation distribution coefficients combined with physical property measurements could be used to establish a baseline for defect content. Changes to the properties would accompany subsequent service-induced changes to defect content and these might be interpreted, within the framework developed in this work, as changes to the microcrack density. Even though any physical property that depends on the presence of microcracks could be used for this type of monitoring, there are advantages to using those that relate more completely to the overall structure of the material. In this work, the focus has been on elastic responses and thermal expansion. Since the elastic

behavior depends on two orientation distribution coefficients (W_{200} and W_{400}) instead of only one (W_{200} as is the case for thermal expansion), measurements of the elastic properties more completely capture the structure-related symmetries of the material than does thermal expansion. Indeed, the general development for the properties of textured materials considered in this work (transversely isotropic, polycrystalline materials composed of grains from the hexagonal crystal system) indicates that any property represented by a second rank tensor (such as thermal expansion) depends only on one orientation distribution coefficient. Other properties such as electrical conductivity, thermal conductivity and dielectric permittivity might be used for characterization or monitoring purposes, but they only partially reflect the underlying structure because they are represented by second rank tensors (for linear systems). While most property measurements incompletely reflect the totality of material structure, those that are represented by higher rank tensors have the potential to capture more structure-related information and this could be important for characterization purposes.

E.6. Conclusions

In this work, an ultrasonic technique for characterization of anisotropy in polycrystalline graphites was demonstrated.

- Laser-based ultrasonics techniques were used to perform shear wave birefringence measurements. These measurements can be used to ultrasonically characterize polycrystalline materials displaying texture and can provide information about the related symmetries of these materials through the elastic moduli.
- Elastic moduli measured using laser ultrasonic methods were interpreted within a framework describing the behaviors of textured anisotropic materials to describe the overall symmetry of a polycrystalline graphite – NBG-25.
- The framework developed to interpret property measurements in polycrystalline ensembles was based on a modified Hill averaging scheme in which both the Reuss and Voigt limits contribute to the overall property average. To successfully apply this averaging scheme to polycrystalline graphite, the effect of microcracking on the elastic response needed to be considered and this was taken into account using microcrack-modified values for the single crystal elastic constants. By incorporating the microcrack-modified values for the single crystal elastic constants into the modified Hill average, laser ultrasonic shear wave birefringence measurements could be used to derive values for the orientation distribution coefficients W_{200} and W_{400}.
- Thermal expansion measurements on NBG-25 reported in the literature were interpreted using the approach outlined in this work to arrive at a value for W_{200} that agreed well with the corresponding value obtained using ultrasonics measurements.

- Anisotropy in nuclear graphites can be quantified using elasticity and/or thermal expansion measurements, but the elastic response can provide more information about the anisotropy material since it can provide additional texture information through the orientation distribution coefficient W_{400} which cannot be measured using thermal expansion measurements. This additional information about the preferred orientation of graphite microstructure could be useful in forming a more complete understanding of graphite behavior in service environments.

Future work will focus on applying the approach described in this proposal to other polycrystalline graphites to establish quantitative relationships between processing conditions and anisotropy in as-received materials and to investigate variations in anisotropy produced by service-related conditions.

References

[E1] BJ Marsden, M Haverty, W Bodel, GN Hall, AN Jones, PM Mummery, M Treifi. Dimensional change, irradiation creep and thermal/mechanical property changes in nuclear graphite, International Materials Reviews, 61 (2016) 155-182. DOI:10.1080/09506608.2015.1136460

[E2] T Lokajicek, P Lukas, AN Nikitin, IV Papushkin, VV Sumin, RN Vasin. The determination of the elastic properties of an anisotropic polycrystalline graphite using neutron diffraction and ultrasonic measurements, Carbon. 49 (2011) 1374-1384.

[E3] A Allen, M Hutchings, C Sayers, D Allen, R Smith. Use of Neutron-Diffraction Texture Measurements to Establish a Model for Calculation of Ultrasonic Velocities in Highly Oriented Austenitic Weld Material, J.Appl.Phys. 54 (1983) 555-560.

[E4] M Hirao, N Hara, H Fukuoka, K Fujisawa. Ultrasonic Monitoring of Texture in Cold-Rolled Steel Sheets, J.Acoust.Soc.Am. 84 (1988) 667-672.

[E5] A Clark, R Reno, R Thompson, J Smith, G Blessing, R Fields, P Delsanto, R Mignogna. Texture Monitoring in Aluminum-Alloys - a Comparison of Ultrasonic and Neutron-Diffraction Measurement, Ultrasonics. 26 (1988) 189-197.

[E6] A Moreau, D Levesque, M Lord, M Dubois, J Monchalin, C Padioleau, J Bussiere. On-line measurement of texture, thickness and plastic strain ratio using laser-ultrasound resonance spectroscopy, Ultrasonics. 40 (2002) 1047-1056.

[E7] S Dixon, MP Fletcher, G Rowlands. The accuracy of acoustic birefringence shear wave measurements in sheet metal, J.Appl.Phys. 104 (2008) 114901.

[E8] V Vavrycuk. Real ray tracing in anisotropic viscoelastic media, Geophys.J.Int. 175 (2008) 617-626.

[E9] RB Thompson. Ultrasonic Characterization of Texture and Formability of Rolled Metal Sheets, Mater.Eval. 51 (1993) 1162-1165.

[E10] UF Kocks, CN Tomé, H Wenk, Texture and anisotropy : preferred orientations in polycrystals and their effect on materials properties, Cambridge University Press, Cambridge, U.K. ;New York, 1998.

[E11] H-J Bunge, Texture analysis in materials science : mathematical methods, English ed., Butterworths, London ;Boston, 1982.

[E12] CL Davis, M Strangwood, M Potter, S Dixon, PF Morris. Prediction of elastic modulus plus anisotropy using X-ray and electron backscattered diffraction texture quantification and ultrasonic (Electromagnetic acoustic transducer) measurements in aluminum sheets, Metallurgical and Materials Transactions A-Physical Metallurgy and Materials Science. 39A (2008) 679-687.

[E13] B Kelly. Graphite - the most Fascinating Nuclear Material, Carbon. 20 (1982) 2-11.

[E14] S Sato, S Miyazono. Studies of Elastic Modulus of Irradiated Graphite by an Ultrasonic Pulse Method, Carbon. 2 (1964) 103-114.

[E15] T Oku, T Usui, M Eto, Y Fukuda. Effect of Compressive Stress on Youngs Modulus of Unirradiated and Irradiated Nuclear Graphites, Carbon. 15 (1977) 3-8.

[E16] T Maruyama, M Eto, T Oku. Elastic-Modulus and Bend Strength of a Nuclear Graphite at High-Temperature, Carbon. 25 (1987) 723-726.

[E17] Y Li, R Thompson. Effects of Dispersion on the Inference of Metal Texture from S0 Plate Mode Measurements .1. Evaluation of Dispersion Correction Methods, J.Acoust.Soc.Am. 91 (1992) 1298-1309.

[E18] PJ Kielczynski, A Moreau, JF Bussiere. Determination of Texture Coefficients in Hexagonal Polycrystalline Aggregates with Orthorhombic Symmetry using Ultrasounds, J.Acoust.Soc.Am. 95 (1994) 813-827.

[E19] JF Nye, Physical properties of crystals: their representation by tensors and matrices, 1984 ed., Clarendon Press ;New York, Oxford Oxfordshire, 1984.

[E20] S Haussühl, Physical properties of crystals: an introduction, Wiley-VCH, Weinheim, 2007.

[E21] CN Tomé, see Chapter 7 “Tensor Properties of Textured Polycrystals” in Texture and anisotropy : preferred orientations in polycrystals and their effect on materials properties by UF Kocks, CN Tomé, H Wenk, Cambridge University Press, Cambridge, U.K. ;New York, 1998.

[E22] PR Morris. Averaging Fourth-Rank Tensors with Weight Functions, J.Appl.Phys. 40 (1969) 447-&.

[E23] PR Morris. Relation of Polycrystalline Elastic Properties to Texture, J.Met. 31 (1979) 89-89.

[E24] CM Sayers. Angular Dependent Ultrasonic Wave Velocities in Aggregates of Hexagonal Crystals, Ultrasonics. 24 (1986) 289-291.

[E25] CM Sayers. The Elastic-Anisotropy of Polycrystalline Aggregates of Zirconium and its Alloys, J.Nucl.Mater. 144 (1987) 211-213.

[E26] Y Li, R Thompson. Relations between Elastic-Constants Cij and Texture Parameters for Hexagonal Materials, J.Appl.Phys. 67 (1990) 2663-2665.

[E27] M Dunn, H Ledbetter. Thermal-Expansion of Textured Polycrystalline Aggregates, J.Appl.Phys. 78 (1995) 1583-1588.

[E28] DPH Hasselman, Voigt and Reuss Moduli of Polycrystalline Solids with Microcracks, J Am Ceram Soc. 53 (1970) 170.

[E29] P Wagner, JA O'Rourke, PE Armstrong. Porosity Effects in Polycrystalline Graphite, J Am Ceram Soc. 55 (1972) 214-219.

[E30] JA Hudson. Wave Speeds and Attenuation of Elastic-Waves in Material Containing Cracks, Geophysical Journal of the Royal Astronomical Society. 64 (1981) 133-150.

[E31] O Nishizawa. Seismic Velocity Anisotropy in a Medium Containing Oriented Cracks - Transversely Isotropic Case, Journal of Physics of the Earth. 30 (1982) 331-347.

[E32] JM Assad, RH Tatham, JA McDonald. A Physical Model Study of Microcrack-Induced Anisotropy, Geophysics. 57 (1992) 1562-1570.

[E33] F Guerrero, I Sevostianov, A Giraud. On a Possible Approximation of Changes in Elastic Properties of a Transversely Isotropic Material due to an Arbitrarily Oriented Crack, Int.J.Fract. 153 (2008) 169-176.

[E34] Y Hu, GA McMechan. Theoretical Elastic Stiffness Tensor at High Crack Density, Journal of Seismic Exploration. 19 (2010) 43-68.

[E35] M Schoenberg, J Douma. Elastic Wave-Propagation in Media with Parallel Fractures and Aligned Cracks, Geophys.Prospect. 36 (1988) 571-590.

[E36] Z Zheng. Seismic anisotropy due to stress-induced cracks, Int.J.Rock Mech.Min.Sci. 37 (2000) 39-49.

[E37] M Schoenberg, CM Sayers. Seismic Anisotropy of Fractured Rock, Geophysics. 60 (1995) 204-211.

[E38] DE Bowles. Effect of Microcracks on the Thermal-Expansion of Composite Laminates, J.Composite Mater. 18 (1984) 173-187.

[E39] S Ghabezloo. Micromechanical analysis of the effect of porosity on the thermal expansion coefficient of heterogeneous porous materials, Int.J.Rock Mech.Min.Sci. 55 (2012) 97-101.

[E40] S Ghabezloo. Effect of porosity on the thermal expansion coefficient: A discussion of the paper 'Effects of mineral admixtures on the thermal expansion properties of hardened cement paste' by ZH Shui, R. Zhang, W. Chen, D. Xuan, Constr. Build. Mater. 24 (9) (2010) 1761-1767, Constr.Build.Mater. 24 (2010) 1796-1798.

[E41] Y Kobayashi, M Katayama, M Kato, S Kuramochi. Effect of Microstructure on the Thermal Expansion Coefficient of Sintered Cordierite Prepared from Sol Mixtures, J Am Ceram Soc. 96 (2013) 1863-1868.

[E42] E Sicat, F Gong, D Zhang, T Ueda. Change of the Coefficient of Thermal Expansion of Mortar Due to Damage by Freeze Thaw Cycles, Journal of Advanced Concrete Technology. 11 (2013) 333-346.

[E43] AL Sutton, VC Howard. The Role of Porosity in the Accommodation of Thermal Expansion in Graphite, J.Nucl.Mater. 7 (1962) 58-71.

[E44] GM Jenkins. The Thermal Expansion of Polycrystalline Graphite, J.Nucl.Mater. 13 (1964) 33-39.

[E45] TD Burchell, R Bratton, W Windes, *NGNP Graphite Selection and Acquisition Strategy*, ORNL/TM-2007/153, Oak Ridge National Laboratory, 2007.

[E46] M Davies. *Graphite core components and the graphite core assembly of a High Temperature Gas-cooled Reactor (HTGR)*, presented at the Technical Meeting on High-Temperature Qualification of High Temperature Gas Cooled Reactor Materials held by the IAEA in Vienna, Austria, June 10-13, 2014, https://www.iaea.org/NuclearPower/Downloadable/Meetings/2014/2014-06-10-06-13-TM-NPTD/20_ASME_Articles_4000-6000.pdf dated May 15, 2013, accessed June 2016.

[E47] KY Wen, TJ Marrow, BJ Marsden. The microstructure of nuclear graphite binders, Carbon. 46 (2008) 62-71.

[E48] S Chi, G Kim. Comparison of 3 MeV C(+) ion-irradiation effects between the nuclear graphites made of pitch and petroleum cokes, J.Nucl.Mater. 381 (2008) 98-105.

[E49] K Wen, J Marrow, B Marsden. Microcracks in nuclear graphite and highly oriented pyrolytic graphite (HOPG), J.Nucl.Mater. 381 (2008) 199-203.

[E50] C Karthik, J Kane, DP Butt, WE Windes, R Ubic. Microstructural Characterization of Next Generation Nuclear Graphites, Microscopy and Microanalysis. 18 (2012) 272-278.

[E51] DH Hurley, JB Spicer. Line source representation for laser-generated ultrasound in an elastic transversely isotropic half-space, J.Acoust.Soc.Am. 116 (2004) 2914-2922.

[E52] JB Spicer, FW Zeng. Line source representations for shear wave birefringence measurements in transversely isotropic materials using laser ultrasonics, Wave Motion. 61 (2016) 1-10.

[E53] JR Cost, KR Janowski, RC Rossi. Elastic Properties of Isotropic Graphite, Philosophical Magazine. 17 (1968) 851-854.

[E54] JB Spicer, LR Olasov, FW Zeng, K Han, NC Gallego, CI Contescu. Laser ultrasonic assessment of the effects of porosity and microcracking on the elastic moduli of nuclear graphites, J.Nucl.Mater. 471 (2016) 80-91.

[E55] A Vreeling, J van der Laan, D D'Hulst, P ten Pierick, R den Boef, F van den Berg, *Graphite Irradiation for the European HTR-M/M1 Project*, Nuclear Research and Consultancy Group, ftp://ftp.nrg.eu/pub/www/nrg/2004composites/NRG_Vreeling.pdf accessed June 2016, N.D.

[E56] JA Vreeling, O Wouters, JG van der Laan. Graphite irradiation testing for HTR technology at the High Flux Reactor in Petten, J.Nucl.Mater. 381 (2008) 68-75.

[E57] G Vasudevamurthy, TS Byun, P Pappano, LL Snead, TD Burchell. Effect of specimen size and grain orientation on the mechanical and physical properties of NBG-18 nuclear graphite, J.Nucl.Mater. 462 (2015) 1-7.

[E58] F Entwisle. Thermal Expansion of Pyrolytic Graphite, Physics Letters. 2 (1962) 236-238.

[E59] WH Martin, F Entwisle. Thermal Expansion of Graphite Over Different Temperature Ranges, J.Nucl.Mater. 10 (1963) 1-7.

[E60] WC Morgan. Thermal Expansion Coefficients of Graphite Crystals, Technical Report BNWL-SA-3838, Battelle-Northwest Laboratory, Richland, Washington, 1971.

[E61] WC Morgan. Thermal-Expansion Coefficients of Graphite Crystals, Carbon. 10 (1972) 73-79.

[E62] AC Bailey, B Yates. Anisotropic Thermal Expansion of Pyrolytic Graphite at Low Temperatures, J.Appl.Phys. 41 (1970) 5088-5091.

[E63] DKL Tsang, BJ Marsden, SL Fok, G Hall. Graphite thermal expansion relationship for different temperature ranges, Carbon. 43 (2005) 2902-2906.

Appendix A: Additional Terms for Polycrystalline Elastic Response

These are expressions to be used in models based on those developed by Li and Thompson [E26] for the elastic moduli of polycrystalline materials composed of grains with hexagonal crystal symmetry. For the Voigt model,

$$c_{11}^{0^V} = (8c_{11} + 3c_{33} + 4c_{13} + 8c_{44})/15 \tag{E.A.1}$$

$$c_{44}^{0^V} = (7c_{11} - 5c_{12} + 2c_{33} - 4c_{13} + 12c_{44})/30 \tag{E.A.2}$$

$$c_{12}^{0^V} = (c_{11} + 5c_{12} + c_{33} + 8c_{13} - 4c_{44})/15 \tag{E.A.3}$$

$$A_1^V = (4c_{11} - 3c_{33} - c_{13} - 2c_{44}) \tag{E.A.4}$$

$$A_3^V = (-5c_{11} + 7c_{12} + 2c_{33} - 4c_{13} + 6c_{44}) \tag{E.A.5}$$

$$B^V = (c_{11} + c_{33} - 2c_{13} - 4c_{44}) \,. \tag{E.A.6}$$

For the Reuss model,

$$c_{11}^{0^R} = (s_{11}^0 + s_{12}^0)/[(s_{11}^0 - s_{12}^0)(s_{11}^0 + 2s_{12}^0)] \tag{E.A.7}$$

$$c_{12}^{0^R} = -s_{12}^0/[(s_{11}^0 - s_{12}^0)(s_{11}^0 + 2s_{12}^0)] \tag{E.A.8}$$

$$c_{44}^{0^R} = 1/s_{44}^0 \tag{E.A.9}$$

where

$$s_{11}^0 = (8s_{11} + 3s_{33} + 4s_{13} + 2s_{44})/15 \tag{E.A.10}$$

$$s_{44}^0 = 2(7s_{11} - 5s_{12} + 2s_{33} - 4s_{13} + 3s_{44})/15 \tag{E.A.11}$$

$$s_{12}^0 = (s_{11} + 5s_{12} + s_{33} + 8s_{13} - s_{44})/15 \,. \tag{E.A.12}$$

Also,

$$A_1^R = -4(c_{44}^{0^R})^2 a_1 - 14c_{12}^{0^R} c_{44}^{0^R} a_0 \tag{E.A.13}$$

$$A_3^R = -4(c_{44}^{0^R})^2 a_3 \tag{E.A.14}$$

$$B^R = -4(c_{44}^{0^R})^2 a_4 \tag{E.A.15}$$

where

$$a_0 = (s_{11} + s_{12} - s_{33} - s_{13}) \tag{E.A.16}$$

$$a_1 = (4s_{11} - 3s_{33} - s_{13} - s_{44}/2) \tag{E.A.17}$$

$$a_3 = (-5s_{11} + 7s_{12} + 2s_{33} - 4s_{13} + 3s_{44}/2) \tag{E.A.18}$$

$$a_4 = s_{11} + s_{33} - 2s_{13} - s_{44}\,. \tag{E.A.19}$$

The single crystal compliances are related to the elastic moduli as follows:

$$s_{11} = (c_{33}/c_0^2 + (c_{11} - c_{12})^{-1})/2 \tag{E.A.20}$$

$$s_{33} = (c_{11} + c_{12})/c_0^2 \tag{E.A.21}$$

$$s_{12} = (c_{33}/c_0^2 - (c_{11} - c_{12})^{-1})/2 \tag{E.A.22}$$

$$s_{13} = -c_{13}/c_0^2 \tag{E.A.23}$$

$$s_{44} = 1/c_{44} \tag{E.A.24}$$

where $c_0^2 = c_{33}(c_{11} + c_{12}) - 2c_{13}^2$.

Appendix B: Additional Terms for Polycrystalline Thermal Expansion

The expressions provided here are used with models developed from those presented by Dunn and Ledbetter [E27] for the thermal expansion of polycrystalline materials composed of grains with hexagonal crystal symmetry.

$$\gamma = (s_{11} + s_{12} - s_{13} - s_{33})/(s_{11} + s_{12} - 4s_{13} + 2s_{33}) \tag{E.B.1}$$

$$\eta = [\frac{(2/5)^{1/2}\pi^2(\alpha_3 - \alpha_1)}{21}][\frac{(S_{11}^0 + 2S_{12}^0)[2A_1(-7S_{11}^0 + S_{12}^0) + A_2(S_{11}^0 - 13S_{12}^0)]}{s_{11} + s_{12} - s_{13} - s_{33}}] \tag{E.B.2}$$

$$\kappa = [\frac{2(2/5)^{1/2}\pi^2(\alpha_3 - \alpha_1)}{21}][\frac{(S_{11}^0 + 2S_{12}^0)[2A_1(4S_{11}^0 - 7S_{12}^0) - A_2(7S_{11}^0 - S_{12}^0)]}{s_{11} + s_{12} - s_{13} - s_{33}}] \tag{E.B.3}$$

where

$$S_{11}^{0} = 12s_{44}[s_{33}(s_{11}+s_{12})-2s_{13}^{2}][s_{13}^{2}(2s_{11}-2s_{12}+s_{44})-s_{33}(s_{11}^{2}-s_{12}^{2})] \\ \times[12s_{13}(s_{11}-s_{12})-4(s_{11}^{2}-s_{12}^{2})-s_{33}(9s_{11}-5s_{12})]/D_{1} \tag{E.B.4}$$

$$S_{12}^{0} = -12s_{44}[s_{33}(s_{11}+s_{12})-2s_{13}^{2}][s_{13}^{2}(2s_{11}-2s_{12}+s_{44})-s_{33}(s_{11}^{2}-s_{12}^{2})] \\ \times[8s_{13}(s_{11}-s_{12})-(s_{11}^{2}-s_{12}^{2})-s_{33}(s_{11}-5s_{12})]/D_{1} \tag{E.B.5}$$

with

$$D_{1} = 2s_{13}(6s_{13}-s_{44})(2s_{11}-2s_{12}+s_{44})-2(s_{11}^{2}-s_{12}^{2})(6s_{33}+s_{44}) \\ +s_{44}(2s_{13}s_{44}+7s_{11}s_{33}-5s_{12}s_{33}) \tag{E.B.6}$$

and

$$A_{1} = \{2s_{12}(s_{12}s_{33}-2s_{13}^{2})-s_{11}^{2}(2s_{33}+3s_{44})+s_{44}(3s_{12}-4s_{13})(s_{12}+s_{13}) \\ +s_{11}[4s_{13}^{2}+s_{44}(s_{13}+4s_{33})]\}/D_{2} \tag{E.B.7}$$

$$A_{2} = \{4s_{12}(s_{12}s_{33}-2s_{13}^{2})+s_{11}^{2}(s_{44}-4s_{33})+s_{44}[s_{12}(7s_{33}-s_{12})+s_{13}(5s_{12}-8s_{13})] \\ +s_{11}[8s_{13}^{2}+s_{44}(s_{33}-5s_{13})]\}/D_{2} \tag{E.B.9}$$

with

$$D_{2} = s_{44}(s_{11}-s_{12})[s_{33}(s_{11}+s_{12})-2s_{13}^{2}]. \tag{E.B.10}$$

Appendix C: Equations for Orientation Distribution Coefficients

First, the quadratic equations produced for the orientation distribution coefficient, $\boldsymbol{W}_{400}$, using expressions for the material elastic moduli are developed here. Equations (E.6)-(E.8) can be expressed in the following form:

$$\overline{c}_{ii}^{I} = c_{ii}^{0^{I}} + [U_{ii}^{I}W_{200} + V_{ii}^{I}W_{400}] \tag{E.C.1}$$

where no summation is implied by the repeated subscript. According to Eq. (E.14), these expressions for the average moduli can be used to construct expressions that represent measured values for $\overline{c}_{11}$, $\overline{c}_{44}$ and $\overline{c}_{66}$. Anyone of these can be used to solve for r and the remaining two can be used to form expressions for the orientation distribution coefficient, W_{400}, in terms of W_{200}. The following equations were used to develop the results presented in this work:

$$
\begin{aligned}
0 = {} & W_{400}^2 (V_{11}^R V_{66}^V - V_{66}^R V_{11}^V) + \\
& W_{400} [(\bar{c}_{11} - c_{11}^{0^V} - U_{11}^V W_{200}) V_{66}^R - (\bar{c}_{11} - c_{11}^{0^R} - U_{11}^R W_{200}) V_{66}^V - \\
& \qquad (\bar{c}_{66} - c_{66}^{0^V} - U_{66}^V W_{200}) V_{11}^R + (\bar{c}_{66} - c_{66}^{0^R} - U_{66}^R W_{200}) V_{11}^V] + \\
& [\bar{c}_{11} (c_{66}^{0^R} - c_{66}^{0^V} + (U_{66}^R - U_{66}^V) W_{200}) - \bar{c}_{66} (c_{11}^{0^R} - c_{11}^{0^V} + (U_{11}^R - U_{11}^V) W_{200}) - \\
& \qquad (c_{11}^{0^V} + U_{11}^V W_{200})(c_{66}^{0^R} + U_{66}^R W_{200}) + (c_{66}^{0^V} + U_{66}^V W_{200})(c_{11}^{0^R} + U_{11}^R W_{200})]
\end{aligned}
\tag{E.C.2}
$$

$$
\begin{aligned}
0 = {} & W_{400}^2 (V_{44}^R V_{66}^V - V_{66}^R V_{44}^V) + \\
& W_{400} [(\bar{c}_{44} - c_{44}^{0^V} - U_{44}^V W_{200}) V_{66}^R - (\bar{c}_{44} - c_{44}^{0^R} - U_{44}^R W_{200}) V_{66}^V - \\
& \qquad (\bar{c}_{66} - c_{66}^{0^V} - U_{66}^V W_{200}) V_{44}^R + (\bar{c}_{66} - c_{66}^{0^R} - U_{66}^R W_{200}) V_{44}^V] + \\
& [\bar{c}_{44} (c_{66}^{0^R} - c_{66}^{0^V} + (U_{66}^R - U_{66}^V) W_{200}) - \bar{c}_{66} (c_{44}^{0^R} - c_{44}^{0^V} + (U_{44}^R - U_{44}^V) W_{200}) - \\
& \qquad (c_{44}^{0^V} + U_{44}^V W_{200})(c_{66}^{0^R} + U_{66}^R W_{200}) + (c_{66}^{0^V} + U_{66}^V W_{200})(c_{44}^{0^R} + U_{44}^R W_{200})]
\end{aligned}
\tag{E.C.3}
$$

Even though W_{200} could be eliminated from these equations, the solution process followed here treated it as a parameter that was fixed when a specific value for W_{200} yielded values for W_{400} from the solutions for Eqs. (E.C.2) and (E.C.3) agreed.

Next, the quadratic equation for W_{200} developed from thermal expansion results will be presented. Equations (E.10)-(E.13) can be expressed in the following form:

$$
\bar{\alpha}_i^I = \alpha^{0^I} + X_i^I W_{200} . \tag{E.C.4}
$$

According to Eq. (E.15), these expressions for the average thermal expansion coefficient can be used to construct expressions that represent measured values for $\bar{\alpha}_1$ and $\bar{\alpha}_3$. Either of these can be used to solve for r and the remaining equation can be used to form an expression for the orientation distribution coefficient W_{200}. The following result was used in this work:

$$
\begin{aligned}
0 = {} & W_{200}^2 (X_1^R X_3^V - X_3^R X_1^V) + \\
& W_{200} [(\bar{\alpha}_1 (X_3^R - X_3^V) - \bar{\alpha}_3 (X_1^R - X_1^V) - \alpha^{0^V} (X_3^R - X_1^R) + \alpha^{0^R} (X_3^V - X_1^V)] + . \\
& \quad (\alpha^{0^R} - \alpha^{0^V})(\bar{\alpha}_1 - \bar{\alpha}_3)
\end{aligned}
\tag{E.C.5}
$$

Appendix D: Relationship of Ultrasonic Measurements to Elastic Moduli

Using standard transmit-and-receive, through-thickness measurement geometries in which an ultrasonic transmitter is located directly opposite a receiver on a sample surface, the ultrasonic wavespeed for a particular wave polarization and propagation direction, v_{ij}, can be computed using measurements of the corresponding wave transit time (or time-of-flight), Δt_{ij}, and the sample thickness, T. With an

additional measurement of the sample density, ρ, the modulus of the material can be determined as follows:

$$\overline{c}_{ij} = \rho(T / \Delta t_{ij})^2 = \rho v_{ij}^2 \tag{E.D.1}$$

where $\overline{c}_{ij}$ is the modulus being measured. This expression provides the connection between the models for elastic modulus developed in previous sections to the ultrasonic measurements that were performed to assess shear wave birefringence.

3. Ultrasonic Scattering Correlation Measurements for Defect Distribution Determination

Section F: Laser Ultrasonic Correlation Measurements

F.1. Overview

Ultrasonic correlation is a powerful technique that can be used to isolate specific structural (and microstructural) defects in materials. At the beginning of this program, we envisioned making ultrasonic correlation measurements in nuclear graphites to isolate specific information about microstructural features in these materials (primarily porosity or voids). Soon after completing standard ultrasonic measurements using laser-based methods, it became clear that the waveforms recorded using these standard methods contained quite a bit of information related to the graphite microstructure and that correlation methods might not be needed. Even so, we rapidly built-up the required measurement system and proceeded to make correlation measurements in several different graphite grades that displayed a variety of ultrasonic behaviors linked to their microstructures. While correlation results seemed to provide some limited information regarding filler particle size or pore spacing in two grades, these results did not provide the type of information that can be derived from ultrasonic data. Typically, ultrasonic correlation is used to extract microstructure-related information from a noise-dominated background – the information of interest cannot be separated from the background in a single measurement and multiple measurements are needed. Correlations among the multiple measurements are used to isolate microstructure-related signals and these are interpreted using concepts from ultrasonic scattering to yield the information of interest.

However, since laser-ultrasonic data were dominated by microstructural-related signals, the usefulness of correlation was rather limited. The underlying problem was that the ultrasonic frequencies that were being used were far too low to successfully apply correlation techniques to nuclear graphites. Having completed correlation measurements at low frequencies, the decision was made to make correlation measurements in nuclear graphites at frequencies higher than 1 GHz in an attempt to isolate microscopic elements of graphite microstructure that were lost in the lower frequency measurements. We have made laser-ultrasonic measurements at these frequencies previously, but the system required to make these measurements needed to be re-built using existing equipment. By the time we were able to test various laser systems required to make the measurements, we found them to be in disrepair and we needed to have them serviced – this delayed progress on this program component. At the end of the project, we have all components in place to make the high-frequency, laser-ultrasonic correlation measurements, but have not been able to make measurements. *These types of measurements could provide fundamental information about the elastic responses of nuclear graphites and create an entirely new understanding of the elastic behaviors of these materials.*

F.2. Methods and Results

Results reported here demonstrate the use of cross-correlation based methods to develop information about nuclear graphite microstructure (*i.e.* location and regularity of pores, grain boundaries, cracks). Measurements included those made using a through transmission setup to take ultrasonic data from two separate spots on a sample to perform cross-correlation. To isolate scattering information, the autocorrelation data from a single location was subtracted from the cross-correlation and the resulting waveform was analyzed for periodicity. Even though this periodicity (assumed to relate to some average scatterer spacing) appeared to have some relation with microstructural features such as grain size and pore spacing, the results were not entirely convincing.

To better isolate the scattering information, a same-side detection setup was used. Once again, data sets were taken from two spots on the same sample, separated by a distance greater than the largest microstructural feature. However, only data between the surface wave arrival and direct longitudinal wave arrival were used for the subsequent analysis since signals in this interval were assumed to result from scattering off nearby microstructural features. The selected data from the two sample spots were cross-correlated and analyzed for periodicity (see Fig. F.1). Taking this periodicity to be related to the time between scattering events and combining it with the longitudinal sound velocity through bulk graphite, estimations for the mean scatterer spacing were determined. For graphites with large (~1.6 mm) and medium (~0.8 mm) grain sizes, these methods produced values for mean scatterer spacing that are on the order of grain size. However, for fine-grained (~15 um) graphites, this method produced a value approximates 25 times larger than the mean grain size, perhaps because the abundance of small scatterers cause destructive interference and only scatterers of a certain size were detected. Results are shown in Table F.1.

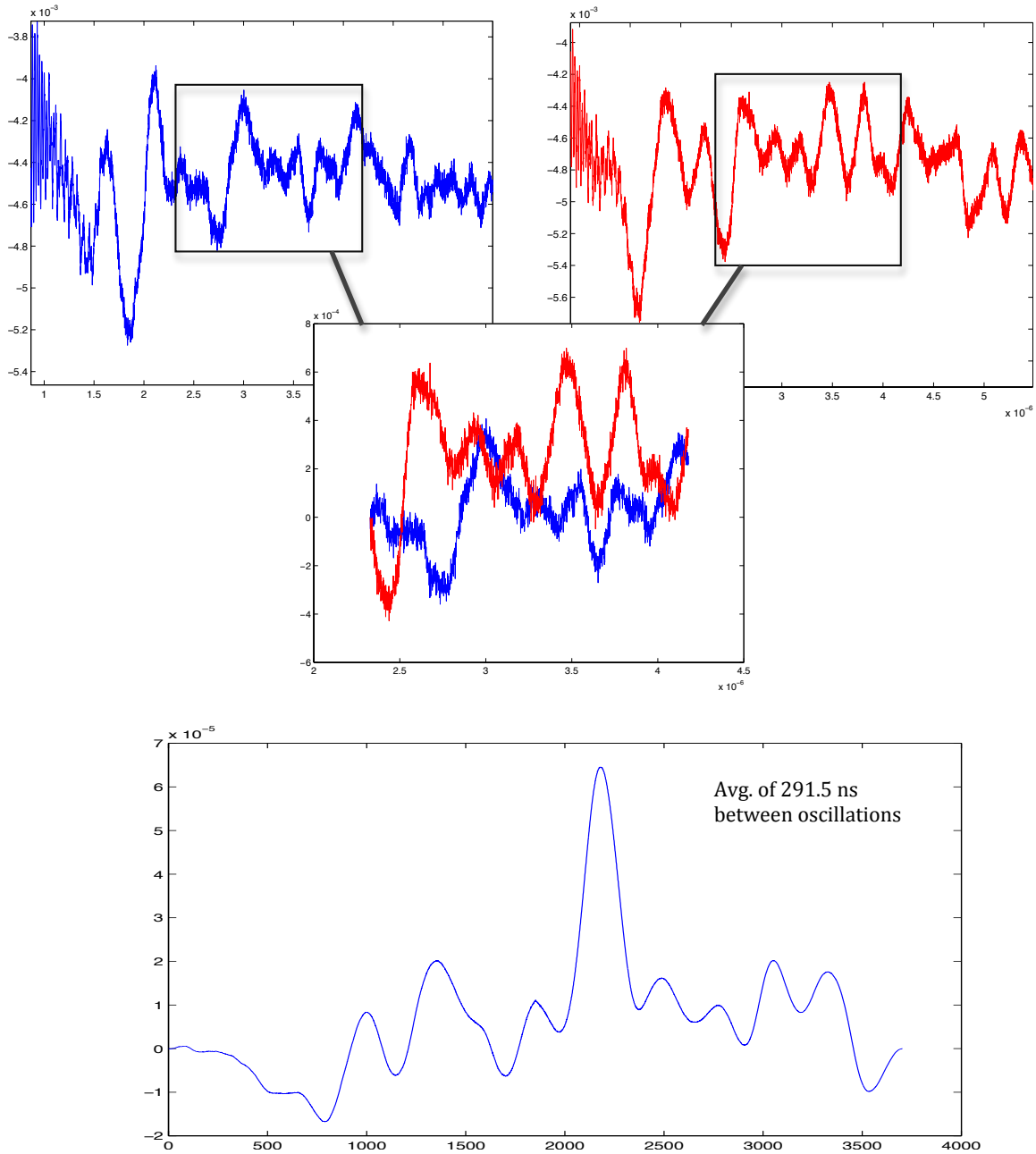

Figure F.1: NBG-10 laser ultrasonic waveforms (top) showing full waveforms along with sections used for cross-correlation and results of cross-correlation (bottom).

Table F.1: Summary of Ultrasonic Correlation Measurements in NBG-10, NBG-17 and 2020

Graphite	Fabrication Process	Longitudinal wavespeed (m/s)	Shear wavespeed (m/s)	Grain size (mm)	Periodicity of Cross Correlation (ns)	Mean scatterer spacing using v = 2495 m/s (mm)
NBG-10	Extruded	2749	1820	Max 1.6	291.5	0.728
NBG-17	Vibramolded	2917	1572	Max 0.8	260.1	0.649
2020	Isostatically pressed	2731	1710	Mean 0.015	147.9	0.369

CONCLUSIONS

Even though we do not have a quantitative understanding of the elastic responses of various microstructural components of nuclear graphite, results from this project have provided new insight into the elastic behavior of these materials especially with respect to the different values for elastic modulus that are found when different measurement methods are used. This topic was the subject of the final research presentation made on the work in this program and is critical to understanding elastic property measurements that might be made in reactor components for the purposes of structural health monitoring. It is widely known that elastic modulus measurements using compression tests differ from those made using vibrational resonance measurements and these can differ from ultrasonic results – all these methods can be used to measure Young's modulus yet all can yield different values. To understand the reasons behind these discrepancies, a detailed understanding of the elastic responses of different microstructural elements (filler particles, microcracks of different types, binder) must be known. While results from this project have shown how microstructural responses could influence bulk modulus measurements, a quantitative understanding is still at large. Instead of invoking various ansatz regarding the operational characteristics of microstructural elements, we need a detailed understanding of their behaviors when they are subjected to various stress states. Through this program, we have extended the state-of-the-art understanding of the elastic response of nuclear graphite and have identified critical needs moving forward – especially as they relate to making ultrasonic sensors that can be used to assess the structural integrity of graphite in reactor cores.

ACKNOWLEDGEMENTS

The project team gratefully acknowledges the support of the U.S. Department of Energy (DOE) through the Nuclear Energy University Program (NEUP) Contract No. 00118687. Research at ORNL was performed collaboratively with The Johns Hopkins University under the DOE Work for Others (WFO) Program.